	1.0	4.5 5.0 5.6	2.8	2.5
			3.2	2.2
			3.6	
	1.1		4.0	2.0
				1.8
	1.25	1.4		1.6

MICROCOPY RESOLUTION TEST CHART
NATIONAL BUREAU OF STANDARDS-1963-A

AFOSR-TR- 85-0854

②

AD-A160 343

RESEARCH PROPOSAL FOR THE INVESTIGATION OF

THE PROPAGATION OF INTENSE CHARGED PARTICLE BEAMS INTO VACUUM

Contract No. AFOSR-84-0091

ANNUAL
PROGRESS REPORT

For the Period April 1, 1984 through March 31, 1985

Submitted to

Air Force Office of Scientific Research

Prepared by

The Electrical Engineering Department and
The Laboratory for Plasma and Fusion Energy Studies
University of Maryland
College Park, Maryland 20742

DTIC
SELECTED
OCT 16 1985
E

DTIC FILE COPY

85 10 11 111
85 10 11 111

RESEARCH PROPOSAL FOR THE INVESTIGATION OF

THE PROPAGATION OF INTENSE CHARGED PARTICLE BEAMS INTO VACUUM

Contract No. AFOSR-84-0091

PROGRESS REPORT

For the Period April 1, 1984 through March 31, 1985

Submitted to

Air Force Office of Scientific Research

Prepared by

The Electrical Engineering Department and
The Laboratory for Plasma and Fusion Energy Studies
University of Maryland
College Park, Maryland 20742

AD-A160 343

REPORT DOCUMENTATION PAGE

1a. REPORT SECURITY CLASSIFICATION	1b. RESTRICTIVE MARKINGS
UNCLASSIFIED	

2a. SECURITY CLASSIFICATION AUTHORITY	3. DISTRIBUTION/AVAILABILITY OF REPORT
	Approved for public release;
2b. DECLASSIFICATION/DOWNGRADING SCHEDULE	Distribution unlimited

4. PERFORMING ORGANIZATION REPORT NUMBER(S)	5. MONITORING ORGANIZATION REPORT NUMBER(S)
	AFOSR·TR· 85-0854

6a. NAME OF PERFORMING ORGANIZATION	6b. OFFICE SYMBOL (If applicable)	7a. NAME OF MONITORING ORGANIZATION
University of Maryland		AFOSR/NP

6c. ADDRESS (City, State and ZIP Code)	7b. ADDRESS (City, State and ZIP Code)
Division of Mathematical & Physical Sciences and Engineering College Park, MD 20742	Building 410 Bolling AFB DC 20332-6448

8a. NAME OF FUNDING/SPONSORING ORGANIZATION	8b. OFFICE SYMBOL (If applicable)	9. PROCUREMENT INSTRUMENT IDENTIFICATION NUMBER
AFOSR	NP	AFOSR 84-0091

8c. ADDRESS (City, State and ZIP Code)	10. SOURCE OF FUNDING NOS.			
Building 410 Bolling AFB DC 20332-6448	PROGRAM ELEMENT NO.	PROJECT NO.	TASK NO.	WORK UNIT NO.
	61102F	2301	A7	

11. TITLE (Include Security Classification)
"PROPAGATION OF INTENSE CHARGED PARTICLE BEAMS INTO VACUUM"

12. PERSONAL AUTHOR(S)
Dr William Destler

13a. TYPE OF REPORT	13b. TIME COVERED	14. DATE OF REPORT (Yr., Mo., Day)	15. PAGE COUNT
ANNUAL	FROM 1 Apr 84 TO 31 Mar 85	31 Mar 85	79

16. SUPPLEMENTARY NOTATION

17.	COSATI CODES		18. SUBJECT TERMS (Continue on reverse if necessary and identify by block number)
FIELD	GROUP	SUB. GR.	

19. ABSTRACT (Continue on reverse if necessary and identify by block number) During the past year the experimental facilities have been augmented by the construction of a large diameter (60cm) vacuum chamber with an array of radial current collectors to support detailed studies of beam propagation characteristics, and a new pulsed magnetic field coil (surplus) from the Autoresonant Accelerator project. This new coil provides much more uniform fields over a longer axial length than did the previous coils. In addition, a Department of Defense University Instrumentation award is currently being used to construct a completely digital fast data acquisition system. This system, currently under installation in a special shielded room in the laboratory, will allow much greater flexibility in the manner in which we acquire and process data and hopefully will eventually reduce the yearly expenditures for Polaroid oscilloscope camera film.

20. DISTRIBUTION/AVAILABILITY OF ABSTRACT	21. ABSTRACT SECURITY CLASSIFICATION
UNCLASSIFIED/UNLIMITED ☒ SAME AS RPT. ☐ DTIC USERS ☐	Unclassified

22a. NAME OF RESPONSIBLE INDIVIDUAL	22b. TELEPHONE NUMBER (Include Area Code)	22c. OFFICE SYMBOL
Major Henry L. Pugh	202/767-4908	NP

DD FORM 1473, 83 APR   EDITION OF 1 JAN 73 IS OBSOLETE.   UNCLASSIFIED

PROGRESS REPORT

SUBMITTED TO: Air Force Office of Scientific Research

SUBMITTED BY: Electrical Engineering Department
                                   University of Maryland
                                   College Park, Maryland 20742

GRANT NUMBER: AFOSR-84-0091

AMOUNT: $131,986

PERIOD: April 1, 1984 through March 31, 1985

PRINCIPAL INVESTIGATORS: William W. Destler, Associate Professor
                                   Electrical Engineering Department

                                   Martin P. Reiser, Professor
                                   Electrical Engineering Department and
                                   Department of Physics and Astronomy

                                   Moon-Jhong Rhee, Professor
                                   Electrical Engineering Department

                                   Charles D. Striffler, Associate Professor
                                   Electrical Engineering Department

TITLE OF RESEARCH PROJECT: "Research Proposal for the Investigation
                                   of the Propagation of Intense Charged
                                   Particle Beams into Vacuum"

PROGRESS REPORT

(for the Period April 1, 1984–March 31, 1985)

A. <u>Propagation of Intense Charged Particle Beams into Vacuum</u>

1. Experimental Studies

a) <u>Improvements to the Experimental Facilities</u>. During the past
year the experimental facilities have been augmented by the construction
of a large diameter (60 cm) vacuum chamber with an array of radial
current collectors to support detailed studies of beam propagation
characteristics, and a new pulsed magnetic field coil (surplus) from the
Autoresonant Accelerator project. This new coil provides much more
uniform fields over a longer axial length than did our previous coils.

In addition, a Department of Defense University Instrumentation
award is currently being used to construct a completely digital fast
data acquisition system. This system, currently under installation in a
special shielded room in our laboratory, will allow much greater
flexibility in the manner in which we acquire and process data and
hopefully will eventually reduce our staggering yearly expenditures for
Polaroid oscilloscope camera film.

b) <u>Studies of Intense Beam Propagation in Vacuum after Passing
Through a Localized Plasma</u>. These studies, detailed in two papers
enclosed in the Appendix ("Electron Beam Propagation Through a Localized

Plasma into Vacuum," published in Physical Review Letters, and "Experimental Study of Electron Beam Propagation Through a Localized Plasma into Vacuum," published in Physics of Fluids), represent the first detailed look at an experiment in which co-moving electrons and ions are joined in a manner that results in effective propagation of beam energy. In the experiments, an electron beam current in excess of 20 kA was observed to propagate to a current collector 55 cm downstream of the injection point after passing through a localized plasma. Beam damage patterns at the collection site indicated that the majority of the propagated beam current was confined to a radius of less than 2 cm even though no confining magnetic field was applied.

Additional results obtained since these results were published included studies of the propagated beam energy vs. net beam current shown in Figs. 1 and 2. To understand the significance of these results, it is helpful to review the proposed mechanism by which beam propagation occurs. It is thought that beam propagation results from a moving "virtual cathode" (formed by the injected electron beam) that draws ions downstream, thereby forming a moving channel of ionization through which the electron beam can propagate. As the formation of this ionization channel to a given axial position can take a substantial fraction of the duration of the injected electron beam pulse, one would expect that if the propagated beam energy were primarily electron beam energy, the observed beam energy in joules for a given net current would decline as the collector is moved farther downstream. The fact that the data for all axial positions falls roughly on the same line is an
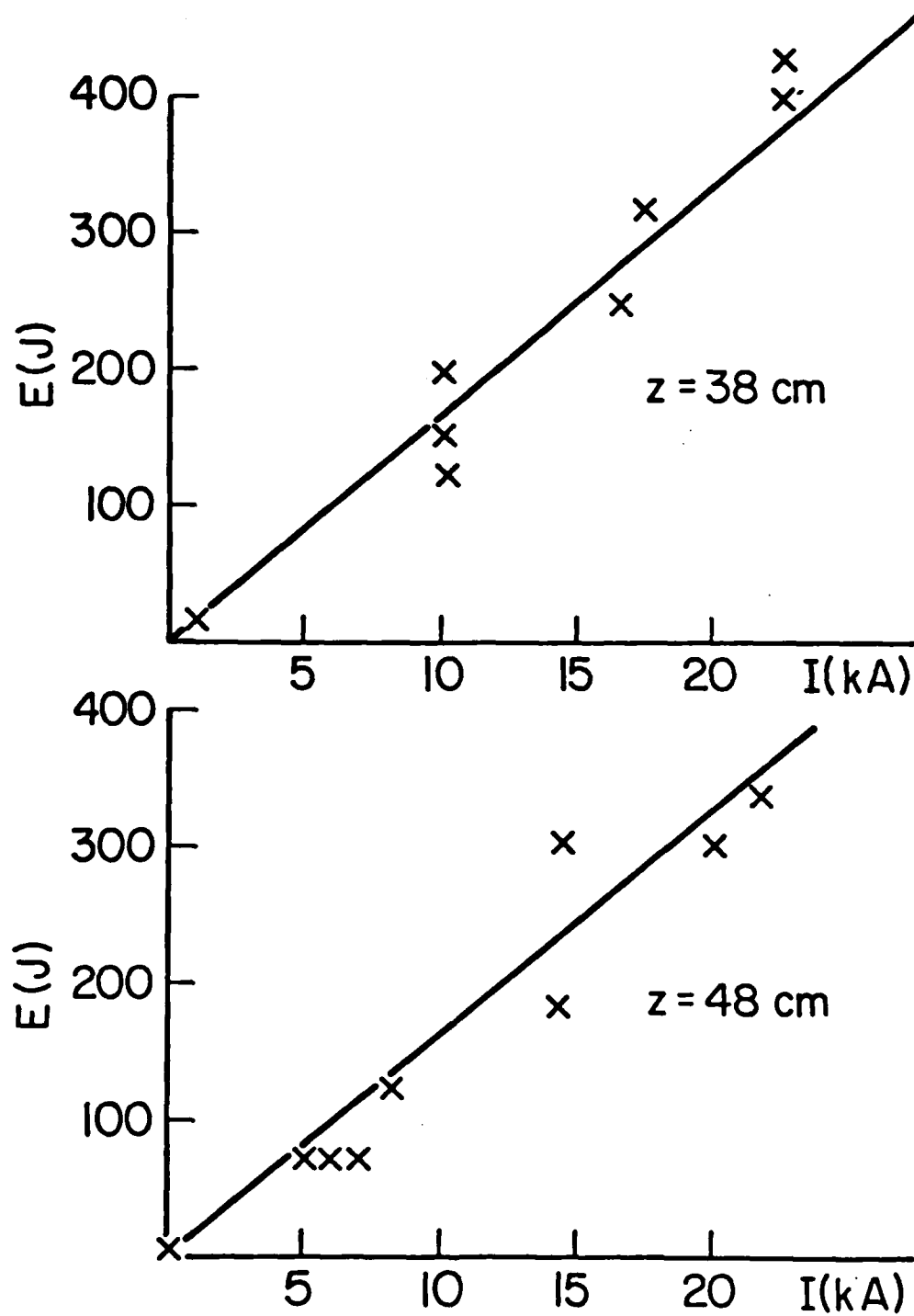
3

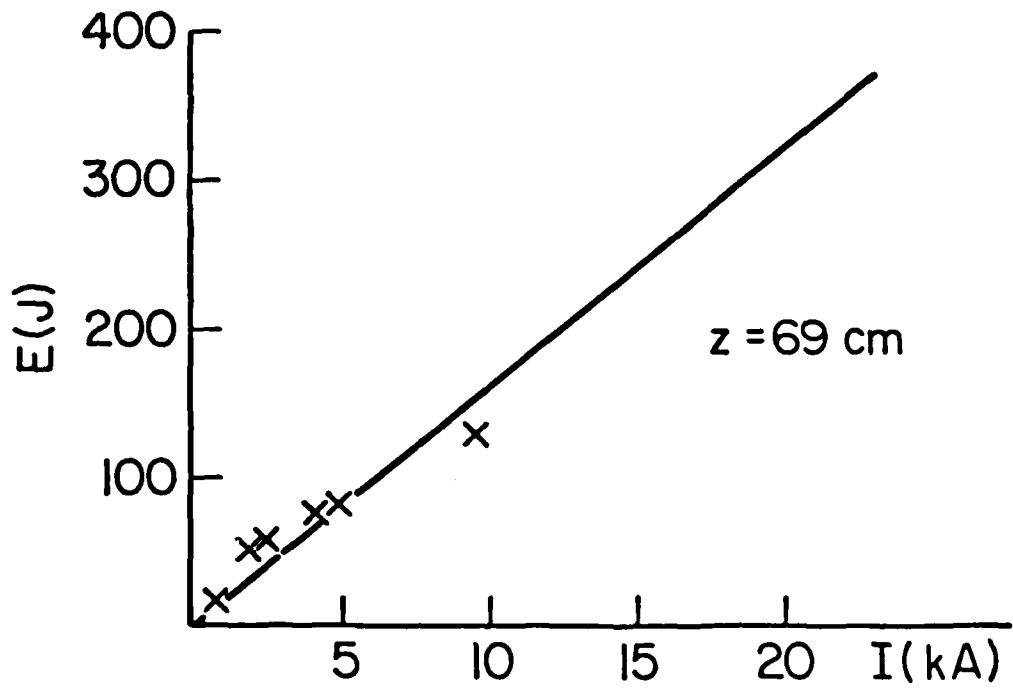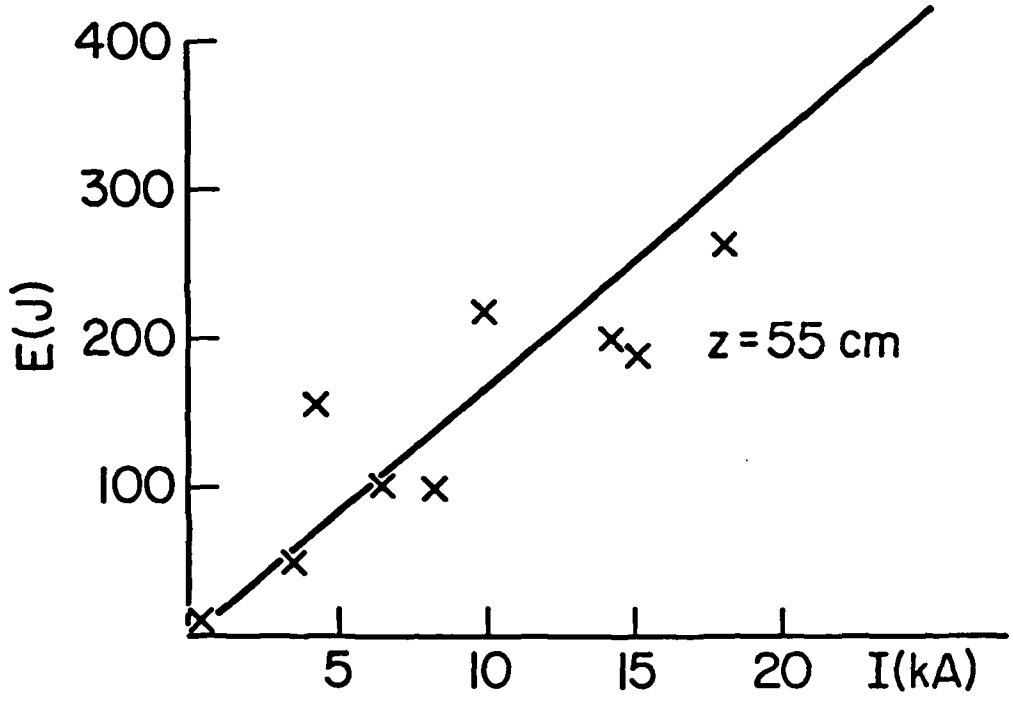FIG. 1. Propagated beam energy vs. net measured current at two different axial positions.

FIG. 2. Propagated beam energy vs. net measured current at two different axial positions.

indication that the energy lost in the time taken to establish the ionization channel is at least partically converted to ion energy.

Preliminary results from the large diameter (60 cm) vacuum chamber studies are shown in Fig. 3. Once again, an intense relativistic electron beam (1 MeV, 22 kA, 30 ns) was injected through a localized gas cloud confined to within 3 cm of the anode plane at the time of electron beam injection. A 6.5 cm diameter Faraday cup/calorimeter was located 40 cm downstream of the injection point. As can be seen, if the peak pressure of the gas cloud is adjusted to an optimum value, almost the entire injected beam current can be propagated to this position in the absence of any confining magnetic field. The large vacuum vessel ensures that wall currents play no significant role in the radial focusing of the beam, and witness plate measurements show that the radial extent of the majority of the beam electrons is no more than 1 cm. More than any other results to date, these studies show dramatically the quality of the radial force balance that can be achieved under the right experimental conditions.

c) Intense Beam Propagation with Applied Magnetic Field. These studies, detailed in a paper enclosed in the Appendix ("Intense Relativistic Electron Beam Propagation in Evacuated Drift Tubes," published in the Journal of Applied Physics) represent the first detailed experimental study of the maximum beam currents that can be propagated in vacuum in the presence of an applied magnetic field. Good overall agreement with theoretical expectations was achieved in these
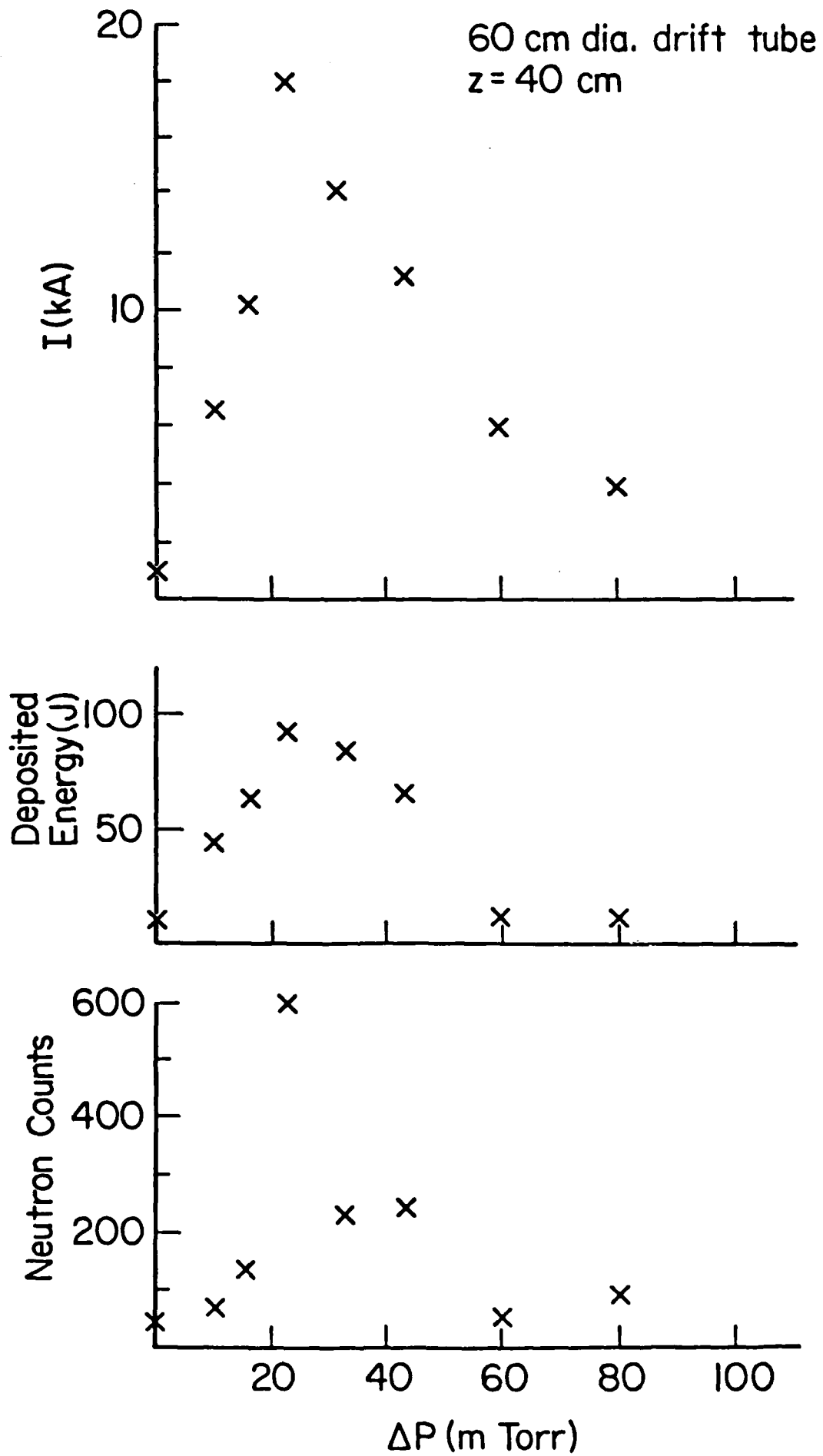
FIG. 3. Results of large diameter drift tube experiment.

studies, and the results should prove valuable to both beam propagation
studies and to high power rf source design studies as well.

2.   Theoretical Research

During the past year, we pursued theoretical studies in three
areas: [a] steady-state equilibria and limiting currents of a
magnetically focused electron beam in a vacuum drift tube, [b] numerical
simulation of a magnetically focused electron beam propagating through a
localized gas cloud in a vacuum drift tube, and [c] analytical model of
electron-ion beam propagation through plasma into vacuum.   Each of these
projects is summarized below.

a) Steady-State Analysis of a Magnetically Confined Electron
Beam. The results of this study are published in J. Appl. Phys. 55,
3934 (1984) [enclosed in the Appendix] and are presented in detail in
the M.S. Thesis of Daniel Welsh, May 1984. The purpose of the
theoretical study is to examine the solutions of an analytical steady-
state model of a solid laminar electron beam propagating inside an
evacuated drift tube which is immersed in an axially applied magnetic
field. A schematic of the model is shown in Fig. 4. The self-fields
generated by the electron beam as well as the diode properties of the
beam are included in the model. These properties of the electron beam
are related via conservation of particle energy and canonical angular
momentum, radial force balance of the beam, and continuity of current.
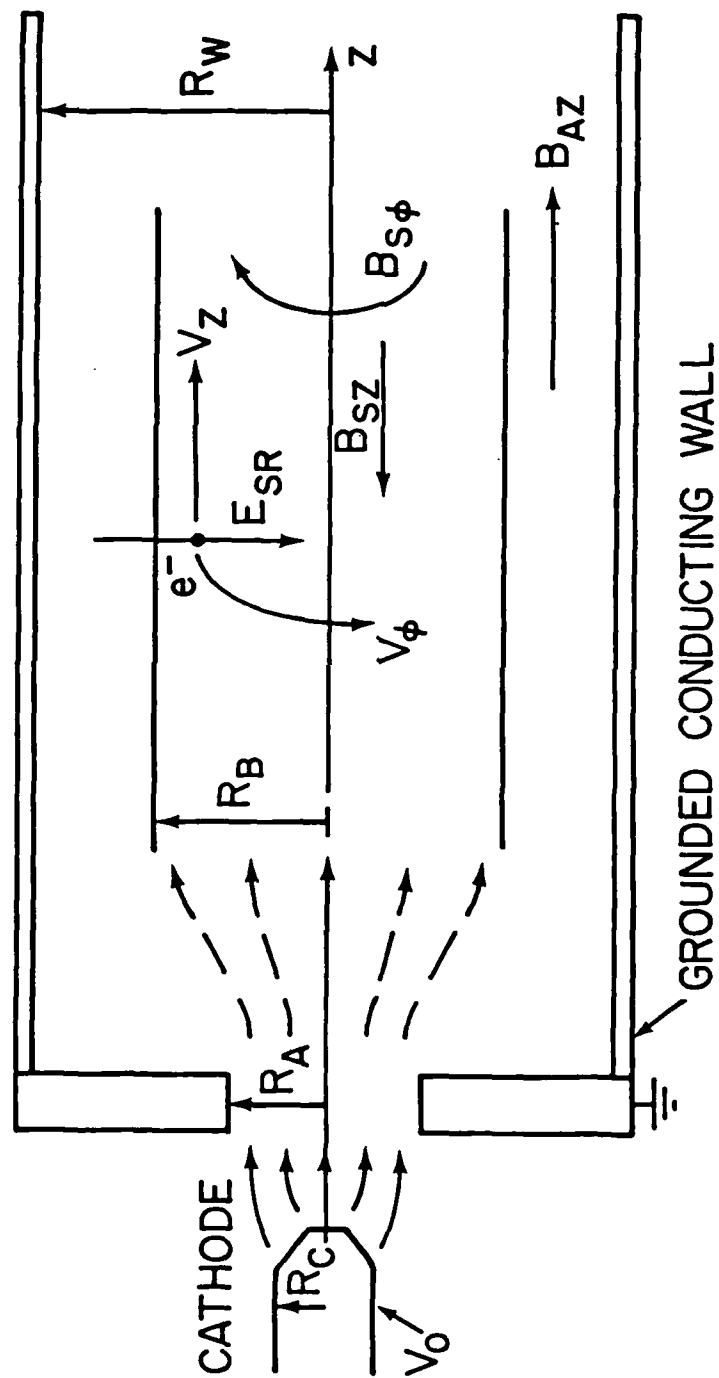A typical set of results obtained from such a model is displayed in

FIG. 4. Schematic of beam model.

Fig. 5. We have plotted the peak beam current that can propagate versus the applied magnetic field for two different anode hole radii. The other parameters of the beam system are given in the figure caption and are those of the experimental system. These analytic results agree with the experimental results as to: I_{peak} versus B_{AZ} profile, quantitative values of the maximum I_{peak}, the value of I_{peak} in the large B_{AZ} regime, and the variation of these results with wall radii R_w and anode hole radii R_a. They do not agree with the value of B_{AZ} where the maximum I_{peak} occurs; the theoretical value being a factor of two less. The analytical model does agree with large numerical simulation results and other analytic theories. Such effects as nonlaminar flow, virtual cathode formation, etc. are not included in the model, but the overall agreement of the results with our experimental results leads us to believe that the basic phenomena responsible for limiting currents is included in the model.

b) Numerical Simulation of Intense Electron Beams. The particle simulations performed in our theoretical group have modelled two systems, (i) The "Experimental" Cylindrical System, and (ii) The "Free-Space" Planar System.

(i) The Experimental Cylindrical System. The cylindrical system is shown in Fig. 6, where a magnetically confined solid electron beam is injected into an evacuated drift tube. Without the presence of a source of ions near the entrance end of the electron beam, a deep potential well of depth about equal to the
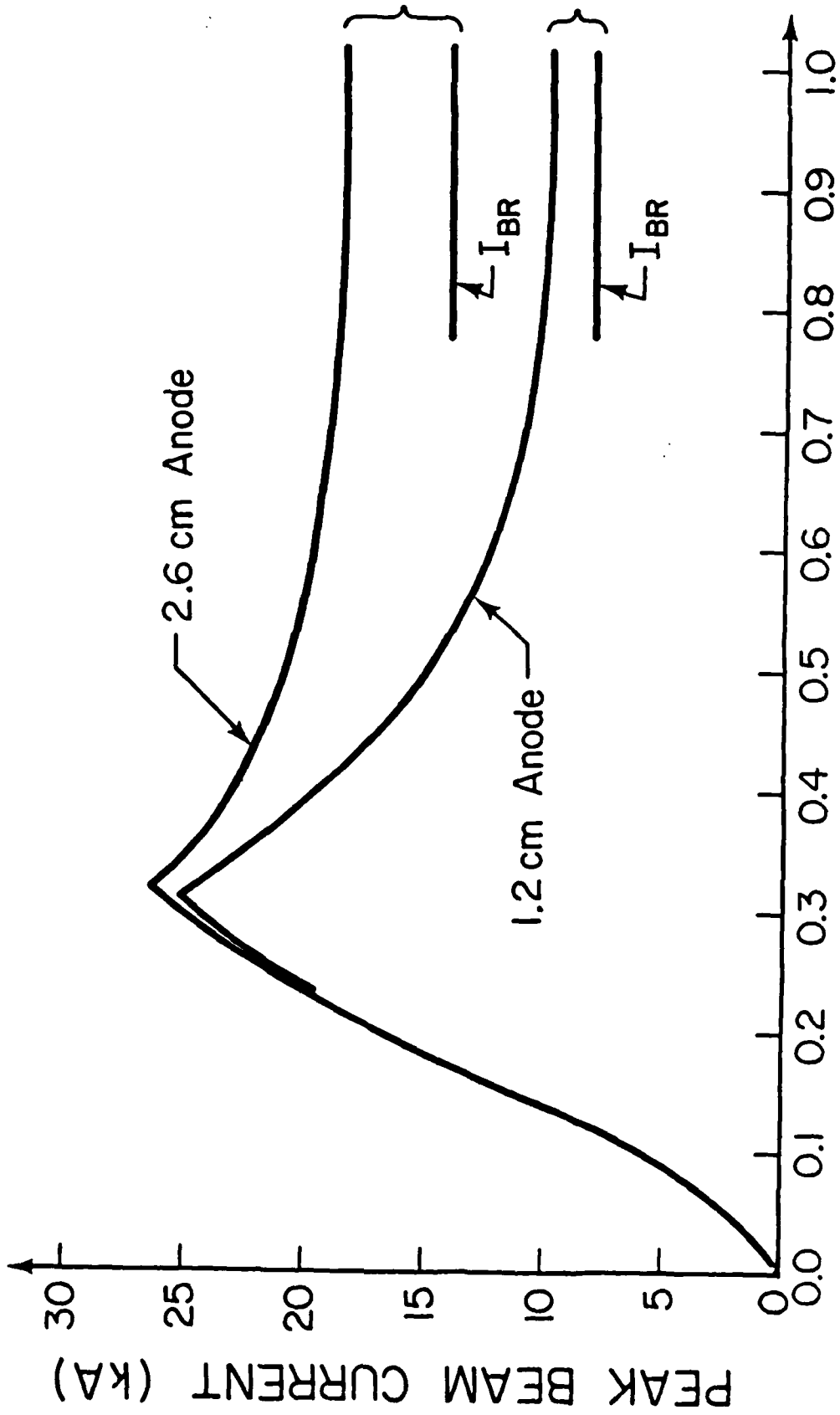
FIG. 5. Maximum propagated beam current versus applied magnetic field for $R_w = 1.9$ cm and $\gamma_0 = 3.5$. Two different anode sizes are shown, $R_a = 0.6$ sm and 1.3 cm.
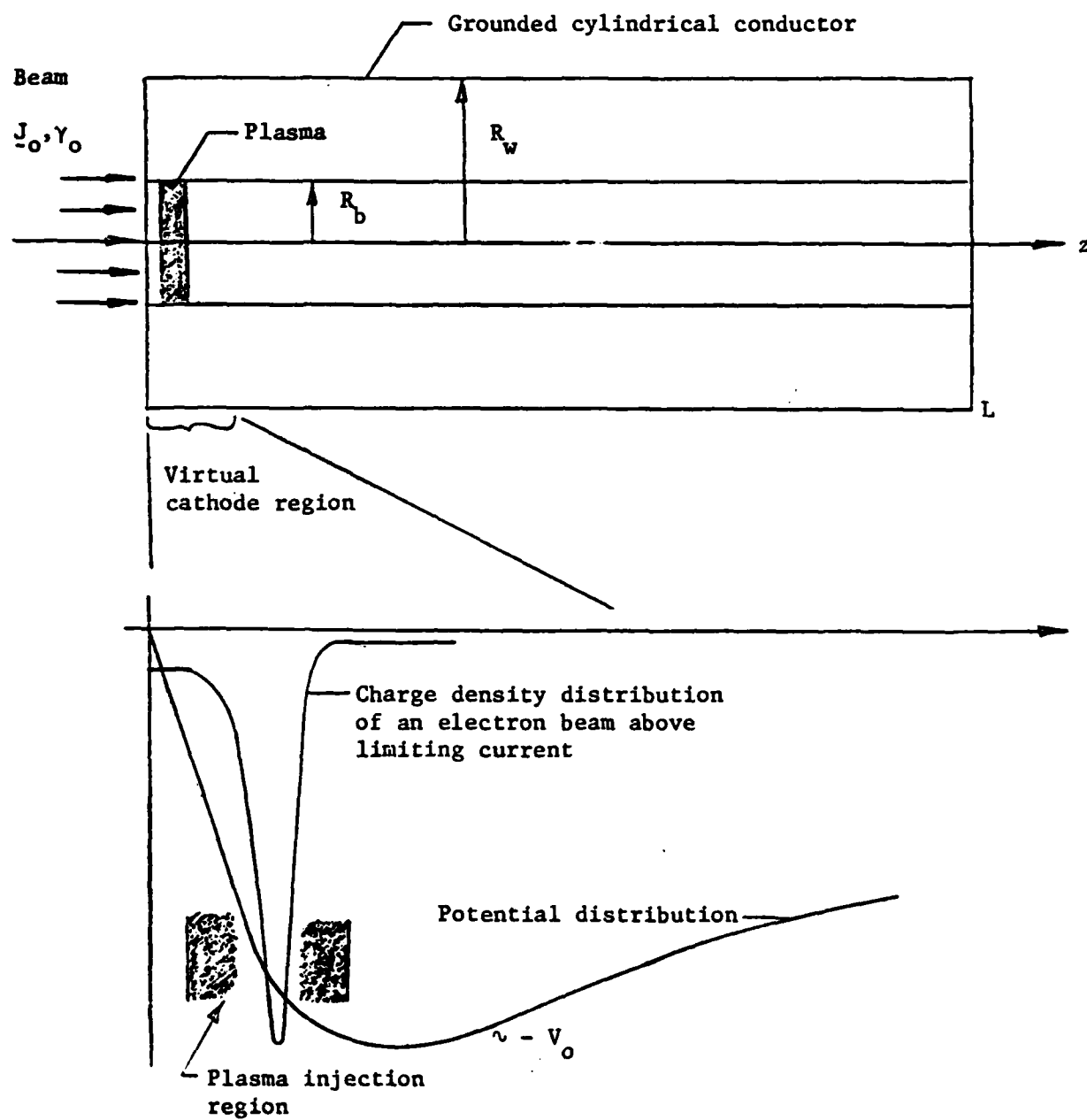
Grounded cylindrical conductor

Beam

J_o, γ_o

Plasma

R_w

R_b

z

L

Virtual
cathode region

Charge density distribution
of an electron beam above
limiting current

Potential distribution

$\sim - V_o$

Plasma injection
region

FIG. 6. Geometry and schematic of numerical simulations.

accelerating voltage V_o forms about 1-3 mm downstream of the entrance end (z = 0, anode). The transmitted current past this deep potential region (virtual cathode) is equal to the limiting current discussed in Section (a). This numerical model is the result of John Grossmann's Ph.D. Thesis, 1982. Since that time, we have modelled the ionization process of a localized gas cloud in the region near the anode. This cloud serves as the source of ions that should enable more electron current to propagate downstream as the ions provide neutralization. The system parameters examined this past year are very close to those of the experimental configuration. The results of this simulation in terms of ion phase-space are shown in Fig. 7. The ion phase-space is shown at 1.05 and 1.95 ns after beam injection. As seen in the plots, a charge neutral plasma (only ions are shown) is injected, to simulate ionization, at a constant rate in the region of maximum electron beam density. Two results are immediately observed from these results: (1) The virtual cathode moves downstream as charge neutralization occurs and (2) peak ion energies have a velocity about twice as fast as the virtual cathode motion. These results are in good qualitative agreement with the experimental observations and have led us to quantify the ionization process more accurately (see Proposed Research).

(ii) The Free-Space Planar System. This past year we have studied via numerical particle simulation the behavior of the motion of an electron beam between two grounded planar surfaces.
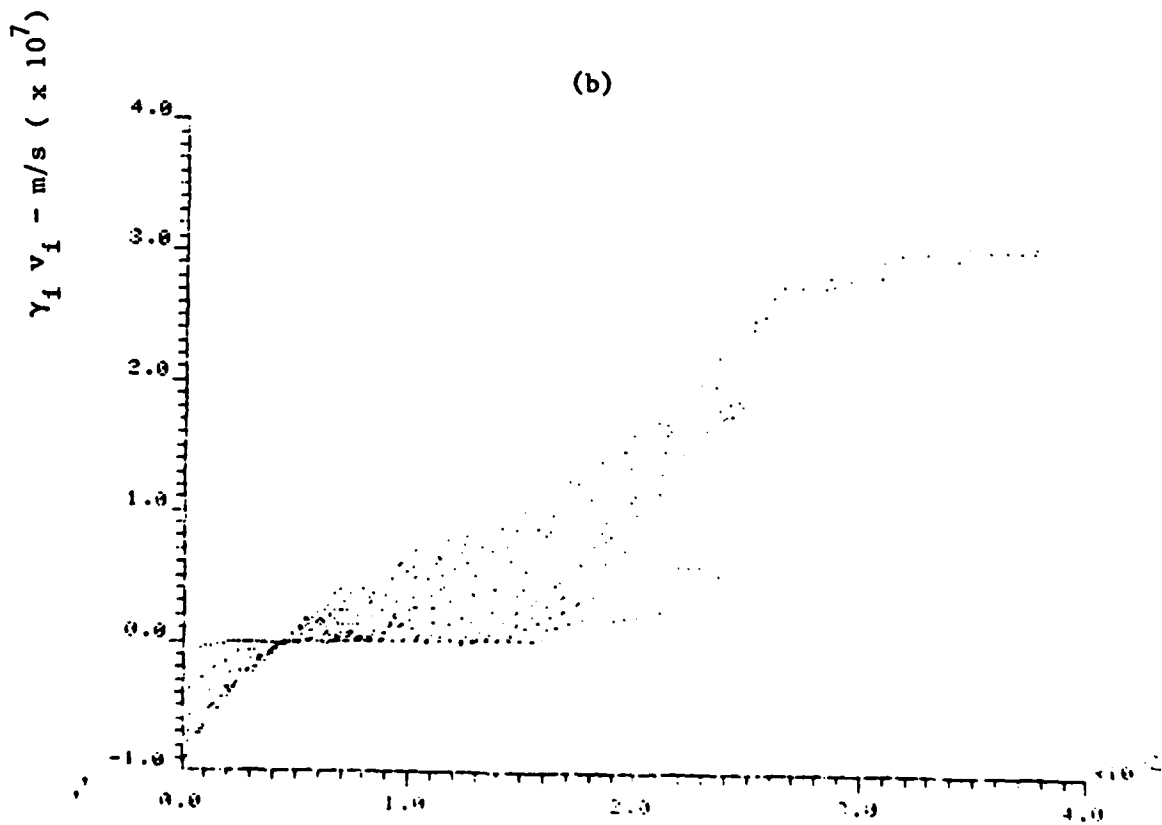
(a)

(b)

$\gamma_i v_i - m/s \ (\times 10^7)$
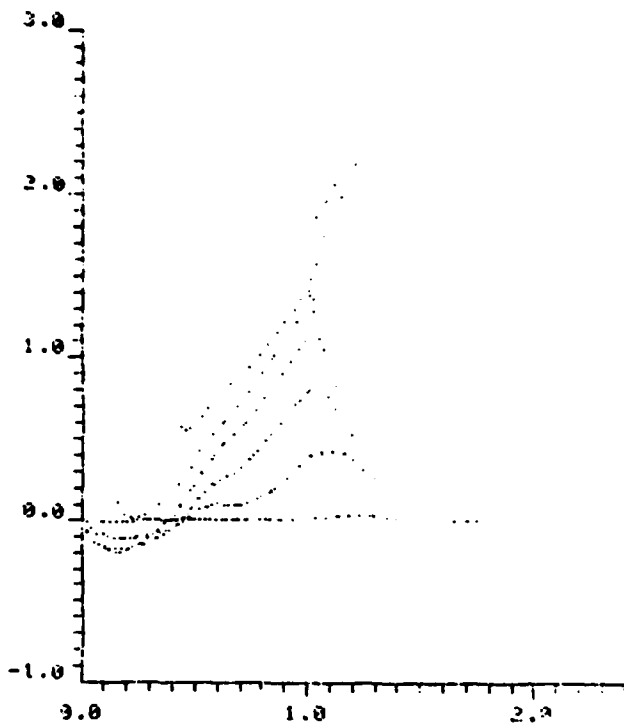
FIG. 7. Ion phase-space plots at (a) t = 1.05 ns and (b) t = 1.95 ns. The system parameters (see Fig.   ) are: γ_o = 3.5 (1.3 MeV), I_o = 35 KA, R_b = 1 cm, R_w = 15 cm, and L = 30 cm.

The results of this work are in the M.A. Thesis of Helen Dantsker, May 1984. As in the cylindrical system, virtual cathodes form when the injected current is above the one-dimensional space charge limiting current. The purpose of this model is to study electron beam injection into free space, i.e. no conducting walls beyond the diode region. This will be discussed further in the Proposed Research Section.
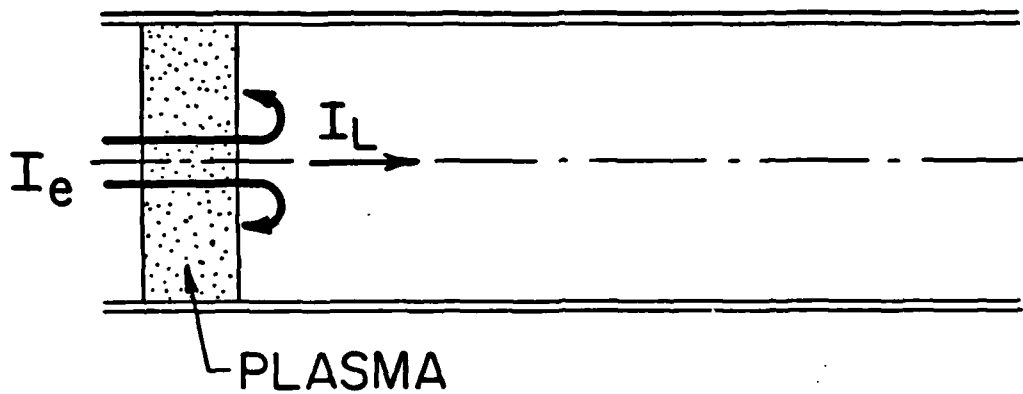
c) Momentum-Balance ("Piston-Plasmoid") Model of Electron Beam Propagation through Plasma into Vacuum. Our recent experiments of electron beam propagation through plasma into vacuum triggered new interest in the development of a theoretical model to explain the observed phenomena. During the summer of 1984, efforts in this direction were successful, and we were able to develop a relatively simple momentum-balance model that links electron beam propagation with collective ion acceleration from the plasma. The new theory represents a major modification of the socalled "piston" model that we published several years ago [J. Appl. Phys. 50, 3015 (1979)]. This earlier model predicted that a small group of ions could be accelerated to the same velocity as the electrons. However, we have since recognized that this is only possible if electron propagation is controlled and facilitated by external means, as in the beam front accelerator. Without such external guidance, electron beam propagation above the space-charge limit in a vacuum drift tube, or in free space, is possible only if partial, or full, charge and current neutralization is provided by co-moving positive ions. In free space, without conducting boundaries

surrounding the beam, full charge and current neutraliztion is required, i.e. the beam propagates only if a "plasmoid" is formed. Our new theory incorporates this feature, hence the name "piston-plasmoid" model. The key feature of this model is based on momentum-balance considerations. As the electron beam is injected into vacuum, a virtual cathode forms and the beam momentarily stops propagating. Electron reflection from this virtual cathode at the beam front transfers momentum to the positive ions from the plasma. The ions are accelerated and a moving ion channel is formed allowing the electron beam to propagate further. This process continues as long as the additional number of ions required to form the channel can be extracted from the plasma at the plane of injection.

In free space, all electrons are reflected back towards the plasma surface, and the average ion density n_i in the channel required for propagation is $n_i = 2n_e/Z$, where n_e is the density of the injected electron beam and Z the charge of the ions. In a drift tube, a fraction of the electron beam corresponding to the limiting current and with density n_L can propagate; the remainder of the beam is deflected sideways to the wall (see Fig. 8). The ion density required for partial neutraliztion such that all injected electrons are able to propagate is $n_i = n_e/Z$. Suppose that the ion channel has a length $L(t)$ and an average velocity $v_i = dL/dt$ at some given time. From momentum balance considerations and using the above neutralization conditions, one can derive the following differential equation

$$L \frac{dv_i}{dt} + v_i^2 = \xi(v_e - v_i)^2 , \tag{1}$$

ELECTRON/ION BEAM PROPAGATION FROM PLASMA INTO VACUUM

a) ELECTRON BEAM INJECTION THROUGH PLASMA INTO DRIFT TUBE (t=0)
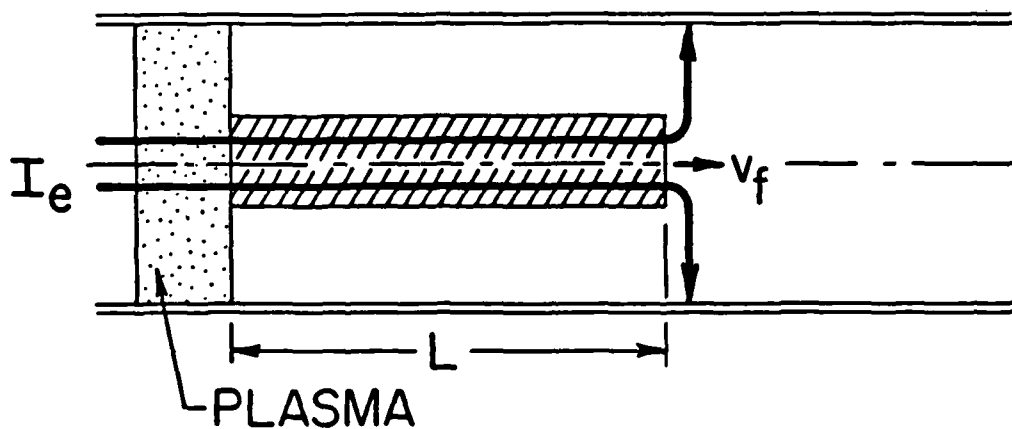
b) ELECTRON BEAM PROPAGATION THROUGH ION CHANNEL AT LATER TIME

FIG. 8. Electron/ion beam propagation from plasma into vacuum.

where $\xi = \gamma_e mZ/M$; m, v_e and M, v_i are the rest mass and velocity of electrons and ions, respectively, and $\gamma_e = (1 - v_e^2/c^2)^{-1/2}$.

From the above equation of motion one finds that the ions are accelerated to an average velocity which reaches a constant upper limit ($dv_i/dt = 0$) given by

$$v_{i,max} = \frac{\sqrt{\xi} - \xi}{1 - \xi} v_e \; . \qquad (2)$$

Numerical integration of Eq. (1) yields v_i as a function of time for several values of γ_e as shown in Fig. 9. A good approximation for $v_i(t)$ is given by the formula

$$v_i = v_{i,max}(1 - e^{-B\sqrt{\xi}t}) \; , \qquad (3)$$

with $B = 2 \times 10^{-10}s^{-1}$ and time t in seconds. From Eq. (3) one can define the characteristic time constant for the initial acceleration

$$\tau = \frac{1}{B\sqrt{\xi}} \; . \qquad (4)$$

Integration of Eq. (3) with $L = L_o$ at $t = 0$ yields

$$L - L_o = v_{i,max}[t - \tau(1 - e^{-t/\tau})] \qquad (5)$$

for the increase of the ion channel length $L - L_o$ versus time. As an example, one gets for electrons with kinetic energy of 1.5
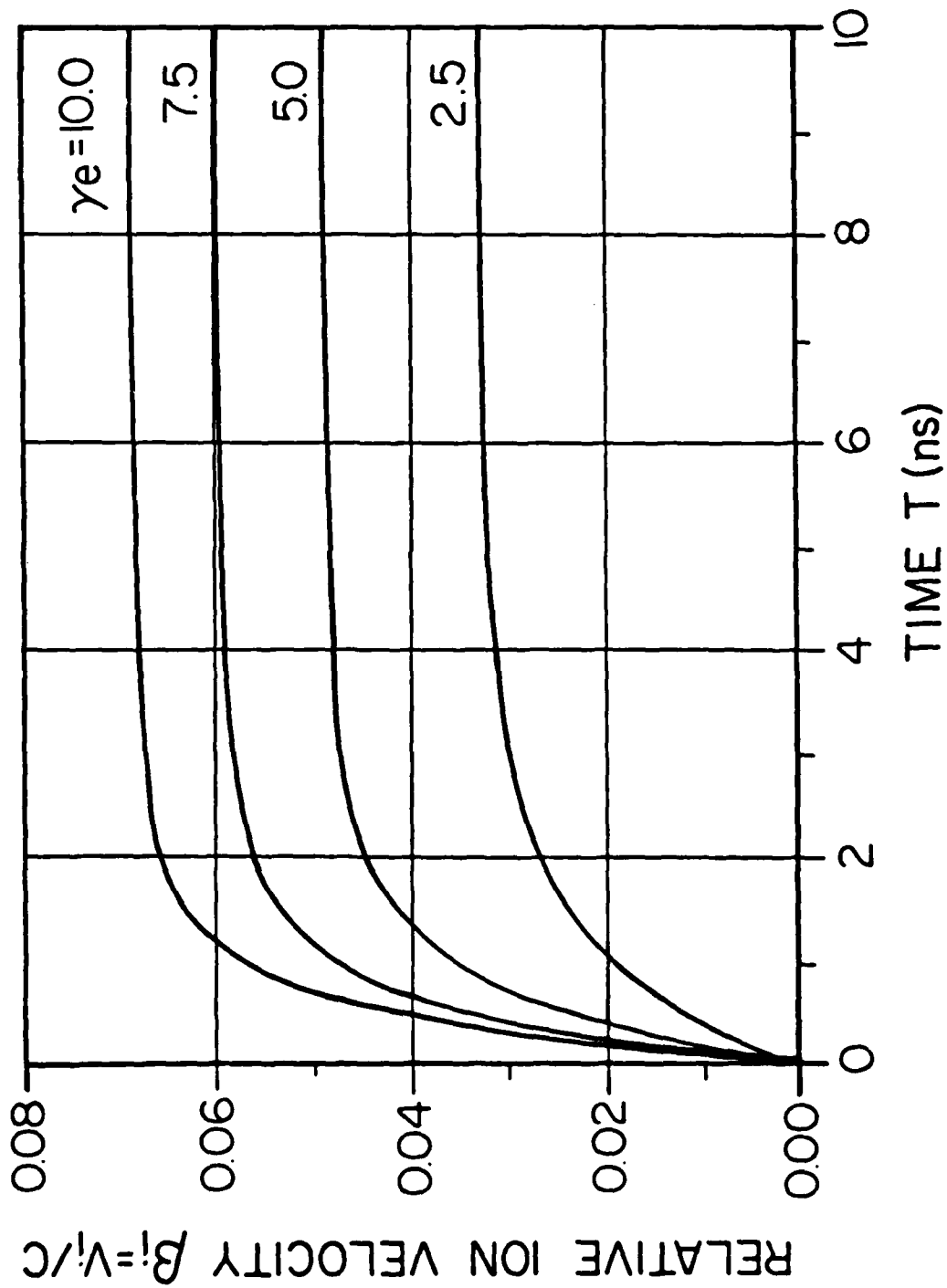
ION VELOCITY VS TIME FOR DIFFERENT VALUES OF γ_e

FIG. 9. Ion velocity vs. time for different electron beam energies.

MeV (i.e. γ_e = 4) and protons with charge Z = 1 and mass M = 1836 m, the following results: ξ = 4/1836, $\beta_{i,max}$ = $v_{i,max}/c$ = 0.043, and τ = 1.07 × 10^{-9}s. The corresponding average kinetic energy of the ions in the channel after the initial acceleration is $K_{i,max}$ = 0.874 MeV.

One should point out that this model describes the average behavior of the particles. Therefore, it does not account for dynamical processes that lead to an ion distribution with a small high energy tail where the ion energy can be several times larger than the electron energy, as observed in experiemnts. However, the predicted average ion energy appears to be reasonable when compared with experimental results. Also in good agreement with experiments is the scaling with Z/M, i.e. the average ion energy depends only on the ratio of charge to mass of the ions.

B. Compact Pulsed Accelerator Research

The major efforts related to the compact pulsed accelerator are described in three categories. These are the development of diagnostics, ion beam studies, and electron beam studies.

1. Development of Diagnostics

a) Thomson Spectrometer. We have been extensively using Thomson spectrometers for ion beam measurements. Thus, it was of interest to make a systematic study of the spectometer system. In this study, we concluded that our unique pinhole arrangement and micro-sized parabola

spectrogram has significant advantages for most applications. This study was published in a paper entitled, "Compact Thomson Spectrometer," [Rev. Sci. Instrum. 55, 1229 (1984)], enclosed in the Appendix. A careful resolution analysis of the Thomson spectrometer was also conducted. Charge, mass, energy, and momentum resolution have been found as functions of collimation parameters and field strengths. The results are generally applicable to all Thomson spectrometer systems. The resulting simple analytical formulas are not only important in analyzing experimental data, but also in designing spectrometers of desired resolution for any particular experiment. This study is detailed in a paper, "Resolution Analysis of the Thomson Spectrometer," [to appear in J. Appl. Phys. 56, (Dec. 1984)] enclosed in the Appendix.

b) Compact Magnetic Electron Analyzer. This simple magnetic spectrometer utilizes a permanent magnet and is capable of measuring electrons of energies 10 keV to 1.5 MeV. The collimated electrons are deflected 180^0 by the uniform magnetic field and strike a phosphor detector. The light emitted by the phosphor is recorded by an open shutter camera placed outside of the vacuum system. This feature allows us to take many spectra without disturbing the experimental condition. A paper detailing this work is currently under preparation.

2. Ion and Neutral Beam Studies

a) Constant Peak Energy per Charge of Ions. Ions produced in plasma focus and collective ion acceleration experiments have been

analyzed using Thomson spectrometers and have been characteristically found to be the same energy as those produced in an ion diode. This feature is clearly displayed by the constant electric deflection of peak energy ions of various charge to mass ratio parabolas. This experimental fact strongly suggests a stationary electric field model or equivalent for the ion acceleration mechanism in both experiments. This is in contrast to other collective ion acceleration models in which a moving field is incorporated.

b) <u>Observation of Energetic Neutrals.</u> Thomson spectrograms almost always display a spot at the origin which corresponds to neutral particles. We have also observed copious neutrals streaming with the electron beam in the opposite direction as the ion beam. A magnetic deflection experiment using a CR-39 detector has revealed that the particles are charge neutral Argon atoms (the fill gas). The total flux of particles has been measured to be 10^7-10^8 particles per shot.

3. Electron Beam Studies

We have invented a new electrode geometry, "Inverted Mather Type Plasma Gun." This electrode system has been used to produce an electron beam which can be easily extracted. The resulting electron beam has attractive characteristics. The energy spectra have been obtained by using the electron spectrometer described earlier. The typical spectrum shows that peak energy exceeds 300 keV and intensity peaks at 100 KeV. The current measured by either a Rogowski coil or a Faraday cup is as

high as 10 kA. The major results of this study are detailed in a paper

entitled, "Operation of a Plasma Focus device as a Compact Electron

Accelerator," (to be submitted to Phys. Fluids for publication) enclosed

in the Appendix.

APPENDIX

Copies of Papers Published during the Period

April 1, 1984 to March 31, 1985

Propagation in Vacuum of an Intense Electron Beam Injected Through a Localized Plasma

W. W. Destler, P. G. O'Shea, and M. Reiser

Laboratory for Plasma and Fusion Energy Studies, University of Maryland, College Park, Maryland 20742

(Received 12 October 1983)

Propagation of an intense relativistic electron beam (1 MeV, 27 kA, 30 ns) in vacuum after passage through a localized hydrogen plasma of ~ 2-cm width has been observed. A large fraction of the injected current was found to propagate in a vacuum drift tube to a distance in excess of 50 cm downstream of the plasma. A description of the process is proposed which links the electron beam propagation with collective ion acceleration and which relates to cosmic-ray acceleration and laser experiments.

The generation and propagation of intense relativistic electron beams (IREB) have been the subject of many theoretical and experimental studies, and the work prior to 1982 is reviewed in the book by Miller.[1] With respect to beam propagation, one distinguishes between propagation in (a) vacuum, (b) plasma, and (c) neutral gas, and the beam current I is generally related to the space-charge–limiting current I_L in (a), and the Alfvén-Lawson current[2,3] I_A in (b) and (c). Thus, in a vacuum drift tube and in the absence of charge-neutralizing ions, IREB propagation is possible only if $I < I_L$ and if a focusing magnetic field B is present. The space-charge–limiting current then depends on whether both the cathode and the drift tube or only the drift tube are immersed in the magnetic field.[4] In the first case, the assumption that $B \rightarrow \infty$ yields the formula for I_L by Bogdankevich and Rukhadze.[5]

For a beam in vacuum with accelerated ions, as in our experiments, neither I_L nor I_A can be applied. In this general case, the propagation is limited by the amount of the fractional charge and current neutralization, f_e and f_m, respectively, and by power-balance considerations, i.e., by the fact that kinetic energy is spent to build up electromagnetic field energy along the path of propagation.[6] The beam particle current can substantially exceed both I_A and I_L as $f_e \rightarrow 1$ and $f_m \rightarrow 1$, and propagation into free-space vacuum is possible if comoving particles of opposite charge are present to assure both charge and current neutralization ($f_e = 1$, $f_m = 1$).

In our present paper, we describe experiments in which IREB propagation in a vacuum drift tube is achieved with currents $I \gg I_L$ when a source of positive ions is provided at the drift tube entrance. These studies were motivated by observations in collective ion acceleration experiments at our laboratory.[7,8] The emphasis in our previous studies

with vacuum drift tubes, as well as in related work by other groups,[9-11] was on detection and measurement of the collective acceleration of ions to high energies. Gilad and Zinamon,[10] for example, accelerated ions from an anode foil with an IREB and observed beam propagation with a B loop. A new feature in our experiments is that the source of ions is a well-localized gas cloud at the anode and that the pressure in the cloud can be controlled externally. The observations that the electron beam propagation distance depends critically on the gas density and that the pulse width (rather than peak electron current) decreases with distance are new results of our recent studies which are reported below.

The experimental configuration used for the studies is shown in Fig. 1. An IREB [1 MeV, 27 kA, 30 ns full width at half maximum (FWHM)] from a 3-mm-diam tungsten cathode was injected through a 26-mm hole in the stainless-steel anode plate (located 6.3 mm from the cathode) into the drift tube region. The drift tube diameter was 15 cm, and the vacuum pressure was in the range 10^{-5}–10^{-4} Torr. No focusing magnetic field was used. A well-localized hydrogen gas cloud was pro-
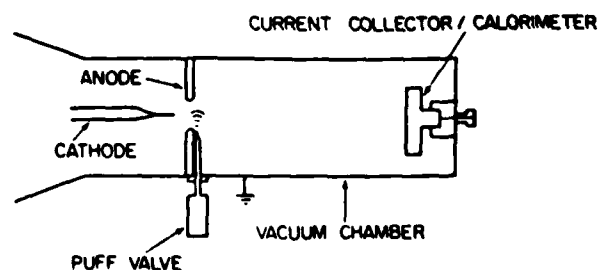

FIG. 1. Experimental configuration for the beam propagation studies with the puff-valve ion source at the anode.
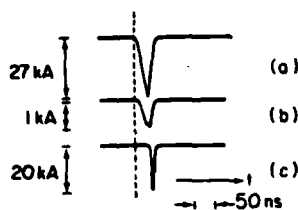
FIG. 2. Current-collector wave forms for (a) injected current, (b) current at $z=38$ cm with no gas injected, and (c) current at $z=38$ cm with optimized gas-cloud pressure at injection.

duced on the downstream side of the anode by firing a fast gas puff valve 540 μs before electron beam injection. Measurements using a fast ionization gauge showed that the effective axial extent of the cloud is less than 2 cm (FWHM) at the time of beam injection, independent of the peak pressure of the gas cloud. By varying the charging voltage of the capacitor bank that powers the puff valve, the effective pressure in the cloud seen by the electron

beam could be varied up to a peak pressure of about 100 mTorr. Ionization of the gas results from electron-impact and ion-avalanche processes.

The current reaching a given position in the drift tube was measured with a low-impedance (14 mΩ) current collector with a carbon beam stop 7.4 cm in diameter. Figure 2 shows typical wave forms from the current collector for (a) the injected current at the anode, (b) the current at $z=38$ cm from the anode with no gas cloud present, and (c) at $z=38$ cm with a gas cloud at optimum pressure present at the anode.

A thermistor embedded in the carbon beam stop was used to measure the temperature rise of the beam stop which yields an estimate of the total beam energy (electrons and ions) propagated to a given axial position in the drift tube. The injected electron beam energy was approximately 1 kJ.

As an additional diagnostic, a silver-activation neutron detector was placed exterior to the drift tube and used to detect neutrons produced by accelerated protons striking the stainless-steel drift tube wall. Proton energies in excess of 5 MeV were routinely observed using foil activation diagnostics.[7]

Figure 3 shows the results obtained from all three diagnostics for beams injected through the localized gas cloud into evacuated drift tubes of axial lengths 38 and 55 cm.

Figure 4 is a photograph of a 20-mil-thick copper witness plate placed 70 cm downstream of the anode and exposed to the beam under conditions where effective beam propagation is observed. The damage pattern results from thermal effects associated with beam energy deposition. The small size (comparable to that of the anode aperture) and circular symmetry of the witness-plate damage pattern
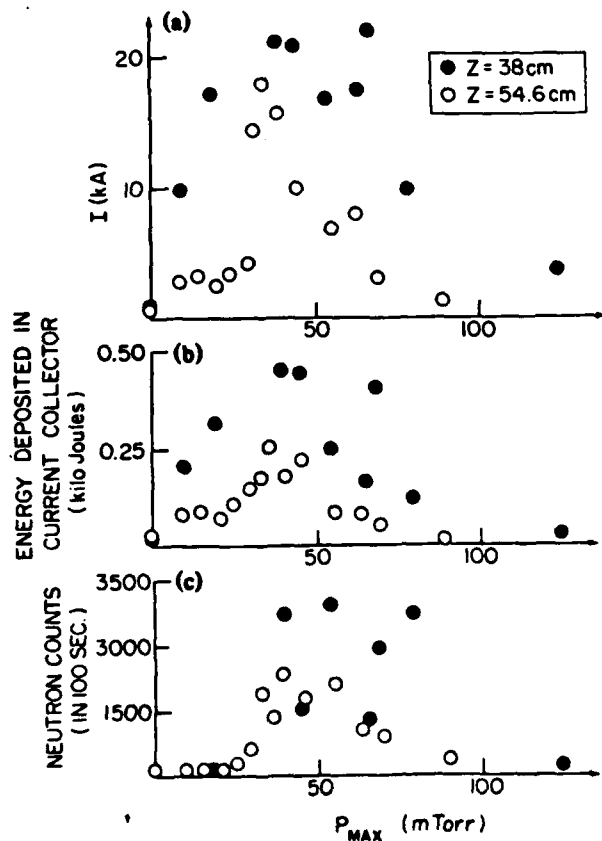
FIG. 3. Results of (a) current collector, (b) calorimeter, and (c) neutron detector measurements at $z=38$ cm and $z=54.6$ cm as a function of gas-cloud peak pressure (p_{max}) at time of beam injection.
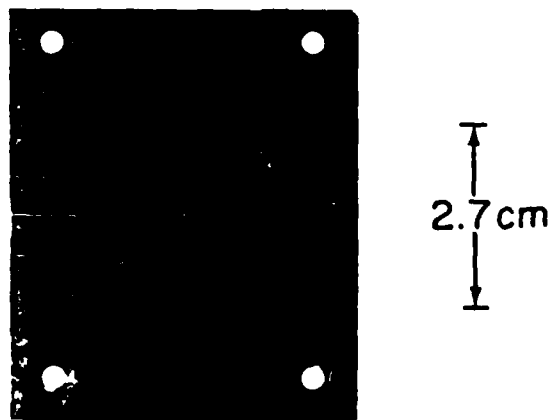
FIG. 4. Photograph of copper witness plate at $z=70$ cm with optimized gas-cloud pressure at injection.

are a clear confirmation of the effective beam propagation due to the gas cloud at the anode.

The results of our experiments may be summarized as follows:

(1) Electron beam current in excess of the space-charge–limiting value I_L (here about 8 kA) can propagate into a vacuum drift tube if a localized source of ions is provided at the injection point.

(2) The propagation of electron beam current to a given axial position is critically dependent upon the peak pressure of the gas cloud; this implies that the propagation results from charge neutralization provided by the localized source, rather than from ions drawn off the drift tube walls or from the background vacuum.

(3) The time delay between the arrival of the electron pulse at the collector and the injected current pulse increases with distance while the width of the collector pulse decreases, indicating that the electrons arriving at the collector come from the late part of the injected beam pulse.

(4) The total energy deposited in the downstream collector at 38 cm is about 50% of the injected beam energy and decreases as the axial position of the collector is increased, even when the peak electron current collected remains about the same.

(5) Neutron production by accelerated protons seems to correlate reasonably well with effective propagation of the beam current. The propagation velocity of the front of the beam is comparable to that of the fast protons observed ($v \lesssim 0.1c$).

These conclusions support a description of the propagation process which we present here as a plausible explanation of the observed phenomena. In this concept, the electron beam enters the drift tube at a current $I > I_L$. Collisional ionization of the gas provides positive ions for charge neutralization and permits the beam to propagate to the edge of the cloud. As the beam enters the vacuum region downstream from the cloud, the space charge forms a "virtual cathode" from which the electrons are reflected back.[6,8] The high electric fields of the virtual cathode draw ions from the cloud until the electron beam can propagate further into the vacuum drift region. This process may repeat itself until a channel of ionization has been produced stretching from the anode to the collector, at which time the remaining beam electron current at the back end of the pulse may flow through the channel at nearly the speed of light and be collected. Thus, the fraction of the injected current pulse arriving at the collector depends upon the time necessary to establish the channel of ionization. As the axial position of the collector is moved further down-

stream, this time increases until it becomes equal to the injected current pulse duration. At this point, the current observed at the collector falls to zero.

The dependence of the propagation on the gas pressure can be explained as follows. At low pressures, ions are not available in sufficient number to achieve the partial neutralization required for efficient propagation. Thus, the beam spreads radially as it propagates, resulting in more current collected at $z = 38$ cm than at 55 cm, etc. As the injected gas pressure is increased, an optimum value is reached at which just the right amount of ions is available for adequate partial neutralization and effective propagation of the electron beam. Beyond this optimum value, a larger number of ions is available and may be accelerated at the expense of a lower peak and/or average ion velocity. Thus, given the finite pulse length of the beam (~ 30 ns), effective propagation cannot be achieved as far down the drift tube as under optimum conditions. This conclusion is supported by the drop in neutron production at high gas-puff pressures.

This process is somewhat similar to that discussed by Ryutov and Stupakov[11] in reports of experiments in which an intense electron beam is injected through an anode foil into vacuum in the presence of a strong axial magnetic field. In our experiments, however, the absence of the confining magnetic field render Ryutov's one-dimensional model (with reflecting electrons) inapplicable. Because of the difficulty in treating analytically the three-dimensional (3D) beam front and transverse electron-ion dynamics, the propagation process may be best studied by use of 2D or 3D particle-in-cell simulation codes.

The propagation of charged particles in vacuum is of fundamental interest in many areas such as astrophysics, laser fusion, ion propulsion, etc. In the absence of a charge-neutralizing plasma, it is clear from our results and the preceding discussion that free-space propagation requires comoving positive ions to assure charge and current neutrality. Thus, if an intense flux of relativistic electrons is ejected from an object (e.g., star, laser pellet) into free-space vacuum, the negative space charge forms a "mirror" reflecting the electrons back towards the surface. If a plasma is present, collective acceleration of positive ions facilitates propagation away from the surface. This process is different from ambipolar diffusion in that the relativistic electrons provide the energy source for propagation into vacuum. A large number of reflecting electrons accelerates a smaller number of ions until the electron pulse terminates (as in our experiments), the sup-

ply of ions is cut off, or the comoving ions at the front of the stream have reached the same velocity as the injected electrons[6] (in which case no further electron reflections occur at the front and a charge- and current-neutralized "plasmoid" is formed). Thus, collective ion acceleration associated with the propagation of intense electron streams into free-space vacuum could play a role in the generation of high-energy cosmic rays whose origin is still an open question.[12]

This mechanism could also explain the energetic positive ions observed in laser-target–interaction experiments[13] when the fast electrons produced in the target try to escape from the target-plasma surface. We hope that future results of our investigations will provide further understanding of the correlation between collective ion acceleration and beam propagation in vacuum.[14]

[1]R. B. Miller, *An Introduction to the Physics of Intense Charged Particle Beams* (Plenum, New York, 1982).

[2]H. Alfvén, Phys. Rev. 55, 425 (1939).

[3]J. D. Lawson, J. Electron Control 3, 587 (1957), and 5, 146 (1958).

[4]M. Reiser, Phys. Fluids 20, 477 (1977).

[5]L. S. Bogdankevich and A. A. Rukhadze, Usp. Fiz. Nauk. 103, 609 (1971) [Sov. Phys. Usp. 14, 163 (1971)].

[6]M. Reiser, in *The Challenge of Ultra-High Energies*, Proceedings of the ECFA-RAL Meeting, Oxford 1982 (Rutherford-Appleton Laboratory, Chilton, Didcot, United Kingdom), p. 131.

[7]W. W. Destler, L. E. Floyd, and M. Reiser, IEEE Trans. Nucl. Sci. 26, 4177 (1979), and Phys. Rev. Lett. 44, 70 (1980); J. T. Cremer and W. W. Destler, IEEE Trans. Nucl. Sci. 30, 3186 (1983).

[8]W. W. Destler, H. S. Uhm, H. Kim, and M. Reiser, J. Appl. Phys. 50, 3015 (1979).

[9]R. Adler, J. A. Nation, and V. Serlin, Phys. Fluids 24, 347 (1981); F. Mako, A. Fisher, N. Rostoker, D. Tzach, IEEE Trans. Nucl. Sci. 26, 4199 (1979); D. W. Swain, G. W. Kuswa, J. W. Poukey, and C. L. Olson, in *Proceedings of the Ninth International Conference on High Energy Acclerators, Stanford, California, 1974*, CONF-740 522 (National Technical Information Service, Springfield, Va., 1974), p. 268.

[10]P. Gilad and Z. Zinamon, Phys. Rev. Lett. 37, 697 (1976).

[11]D. D. Ryutov and G. V. Stupakov, Sov. J. Plasma Phys. 2, 427 (1976); D. D. Ryutov, in *Proceedings of the Fourth International Conference on High Power Electron and Ion Beam Research and Technology, Palaiseau, France, 1981*, edited by H. J. Doucet and J. M. Buzzi (Laboratoire Physique des Milieux Ionises, Palaiseau, France, 1981), p. 77.

[12]A recent review on the topic of acceleration of galactic cosmic rays was given by W. I. Axford, in *Origin of Cosmic Rays*, edited by G. Setti, G. Spada, and A. W. Wolfendale (Reidel, Higham, Mass., 1981), pp. 339–358.

[13]J. S. Pearlman and G. H. Dahlbacka, Appl. Phys. Lett. 31, 414 (1977); Y. Gazit, J. Delettrez, T. C. Bristow, A. Entenberg, and J. Soures, Phys. Rev. Lett. 43, 1943 (1979); G. D. Tsakiris, K. Eidmann, R. Petsch, and R. Sigel, Phys. Rev. Lett. 46, 1202 (1981); H. Hora, in *Laser Interaction and Related Plasma Phenomena*, edited by H. Hora and G. H. Miley (Plenum, New York, 1983), Vol. 6.

[14]A more comprehensive description of our work, including experiments with laser-produced plasmas, will be published in a separate paper.

Propagation of an intense relativistic electron beam through a plasma region into vacuum

W. W. Destler, P. G. O'Shea, and M. Reiser

Laboratory for Plasma and Fusion Energy Studies, University of Maryland, College Park, Maryland 20742

An intense relativistic electron beam (IREB) is injected through a narrow plasma region into a vacuum drift tube at current levels far above the space-charge limit of the drift tube. Experiments show that accelerated co-moving positive ions from the plasma enable the beam to propagate to a collector at the end of the 15 cm diameter drift tube. In one set of experiments, the IREB (1 MeV, 27 kA, 30 nsec) passes through a hydrogen gas cloud with an effective width of approximately 2 cm. The net current measured by a 7 cm diameter collector at the end of a 55 cm long drift tube is 70% of the peak injected electron current. In another configuration, the IREB is injected through a laser-produced carbon plasma. A model is proposed linking electron beam propagation with collective ion acceleration which results in the generation of charge- and current-neutral plasmoids capable of free space propagation. Possible implications of this work to astrophysical processes (cosmic ray acceleration) and laser fusion (observation of high-energy positive ions escaping from target plasma) are discussed.

I. INTRODUCTION AND THEORETICAL CONSIDERATIONS

In recent years, many theoretical and experimental studies concerning the generation and propagation of intense relativistic electron beams (IREB) have been published. A review of the field and a summary of the work prior to 1982 is presented in the book by Miller.[1]

Beam propagation experiments usually involve electron beam injection from a diode (with or without a foil at the anode) into a drift tube. Depending on whether the drift tube is evacuated or filled with a charge-neutralizing medium, one distinguishes between (a) propagation in vacuum, (b) propagation in a plasma, and (c) propagation in a neutral gas. Since in (c) the beam forms a plasma channel by collisional ionization effects, there is no fundamental difference between (b) and (c). In all three cases, the propagation depends on the injected beam current and propagation is usually described in terms of the space-charge limiting current I_L in (a), the Alfvén–Lawson current in (b) and (c), or other limiting effects like instabilities (e.g., hose, sausage, and two-stream instability) in (b) and (c). Thus in a vacuum drift tube and in the absence of charge-neutralizing positive ions, an IREB can propagate only if the beam current I is less than I_L and if a focusing magnetic field is present. Usually a uniform solenoidal magnetic field is employed to confine the flow. The space-charge limiting current then depends on whether both the beam-generating diode and the vacuum drift tube, or only the drift tube, are immersed in the magnetic field.[2] In the first case, the assumption that a very high magnetic field ($B \to \infty$) forces the electrons to move along field lines on straight paths yields the well-known formula for I_L by Bogdankevich and Rukhadze.[3] This formula is also widely used when no external B field is present and the focusing is accomplished by charge-neutralizing positive ions within the electron beam. If f_e denotes the fractional charge neutralization, then one writes the space-charge current limit in the form

$$I_L = I_0 \frac{(\gamma^{2/3} - 1)^{3/2}}{[1 + 2\ln(b/a)](1 - f_e)}, \tag{1}$$

where $I_0 = 4\pi\epsilon_0 m_0 c^3 / e \approx 1.7 \times 10^4$ A for electrons, a = beam radius, b = radius of the drift tube (cylindrical conducting wall surrounding the beam), $(\gamma - 1)m_0 c^2 = eV$ = kinetic energy of the electrons at the plane of injection into the drift tube. Another useful relation, which is given here for reference in subsequent discussions, is the force on an electron at radius r in the beam because of the electric and magnetic self fields[4]:

$$F_r = (qIr/2\pi\epsilon_0 a^2 \beta c)(1 - f_e - \beta^2), \tag{2}$$

with βc = mean axial velocity. From Eq. (2) it follows that the beam is self-focused when partial charge neutralization is present, such that $f_e > 1 - \beta^2$.

From Eq. (1), one would conclude that $I_L \to \infty$ (i.e., no upper limit for the beam current exists) when $f_e \to 1$. However, in this formula the self-field energy has been neglected, and as the beam becomes fully charge neutralized, the energy stored in the magnetic field of the beam must be taken into account. One can derive a more general upper limit for the beam current from consideration of energy conservation or power balance.[5] In the propagation down a drift tube, kinetic energy of the beam is spent to build up field energy. The energy stored in the electric and magnetic self fields of an electron beam of length L is given by

$$W = \frac{I^2 L}{4\pi\epsilon_0 c^2}\left(\frac{1}{4} + \ln\frac{b}{a}\right)\left(\frac{(1 - f_e)^2}{\beta_f^2} + (1 - f_m)^2\right), \tag{3}$$

where both charge and current neutralization are included and represented by the factors f_e and f_m. This field energy results in a difference between the kinetic energy $(\gamma_f - 1)(m_0 c^2/e)$ at the beam front and that at injection, $(\gamma_i - 1)(m_0 c^2/e)$. One can present this energy conservation law in the form of a power balance equation:

$$I(\gamma_f - 1)(m_0 c^2/e) = I(\gamma_i - 1)(m_0 c^2/e) - (W/L)\beta_f c,$$

$$(4)$$

where $\beta_f c$ is the beam front velocity and loss or reflection of electrons at the beam front has been neglected. By substituting (3) into (4), one obtains the following relation for the beam current:

$$I = I_0 \frac{(\gamma_i \gamma_f - \gamma_f^2)(\gamma_f^2 - 1)^{1/2}}{[0.25 + \ln(b/a)][(1 - f_e)^2 \gamma_f^2 + (1 - f_m)^2(\gamma_f^2 - 1)]}.$$

$$(5)$$

The limiting current caused by power balance, $I = I_P$, can be found from the maximum of the curve I vs γ_f, i.e., from the condition $\partial I/\partial\gamma_f = 0$. We note that by setting $f_e = 0, f_m = 0$, one obtains a space-charge current limit that is greater than I_L in (1). Likewise, for the case $f_e = 1, f_m = 0$, one obtains a magnetic limit that is greater than the Alfvén–Lawson current[4,6] $I_A = I_0\beta_i\gamma_i$. This is because of the fact that particle dynamics effects may inhibit the current flow before the fundamental power balance limit is reached. We should point out that the above theoretical picture does not describe how charge- and current-neutralizing ions are supplied to the beam. Such ions could be injected from an external source or, as in our experiment discussed below, they could be drawn from a localized plasma at the injection point by the electric space-charge field associated with the electron beam (via virtual cathode formation).

From the above review of current-limiting phenomena, it is clear that propagation in a vacuum drift tube is not possible for beam currents exceeding the space-charge limit I_L. In fact, in the absence of a confining magnetic field or fractional neutralization, even this current cannot propagate since radial force balance cannot be achieved. To obtain effective propagation at any meaningful current level, charge neutralization by positive ions must be provided to satisfy the force-balance condition $f_e > 1 - \beta^2$; at the same time, the current cannot exceed the power-balance limit, i.e., $I < I_P$. Both current limits, I_L and I_P, depend on the ratio of drift tube radius to beam radius b/a and decrease as b/a increases. Specifically, when no conducting wall is present ($b \rightarrow \infty$), they go to zero ($I_L \rightarrow 0, I_P \rightarrow 0$). This implies that charged particle beams cannot propagate into free space vacuum unless co-moving particles of opposite charge are present in sufficient numbers to assure both charge and current neutralization ($f_e = f_m = 1$). In ion propulsion, for instance, this condition is met by simultaneous ejection of electrons with the ions. On the other hand, in laboratory propagation studies with conducting drift tubes, a plasma or neutral gas background is usually provided to achieve charge neutralization when the beam current exceeds the space-charge limit.[7]

In our present paper we describe experiments in which IREB propagation in a vacuum drift tube is achieved with currents far above the space-charge limit when a source of positive ions (gas cloud or plasma) is provided at the drift tube entrance. These studies were motivated by observations in connection with collective ion acceleration experiments at our laboratory where an IREB pulse (typically 1 MeV, 27 kA, 30 nsec) is injected through a localized gas cloud (from a puff valve) or a laser-produced plasma into a vacuum drift
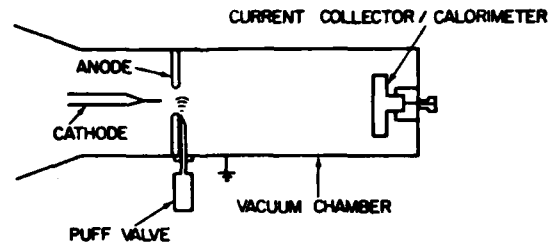

FIG. 1. Experimental configuration used for the puff valve ion source propagation studies.

tube.[8,9] We found that the presence of such an "ion source" at the drift tube entrance not only produced high-energy positive ions by collective acceleration effects, but also facilitated the propagation of a large fraction of the electron beam current down the drift tube.[10] Similar effects were also observed in collective acceleration experiments at other laboratories.[11] In order to obtain a better understanding of the conditions that lead to beam propagation and of the correlation between propagation and collective ion acceleration, we initiated a systematic experimental investigation, the first results of which are reported in the following section.

II. EXPERIMENTS

The configurations used for the studies of electron beam propagation in vacuum are shown schematically in Fig. 1. An intense relativistic electron beam (1 MeV, 27 kA, 30 nsec FWHM) is produced by field emission from a 3 mm diameter tungsten cathode located 6.3 mm upstream of a stainless steel anode plate. A 26 mm hole in the anode plate on axis allowed almost all of the electron beam to pass through the anode plane into the downstream drift region.
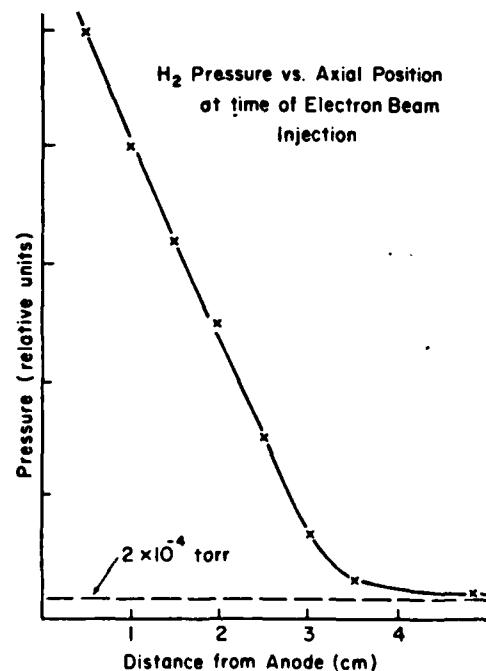

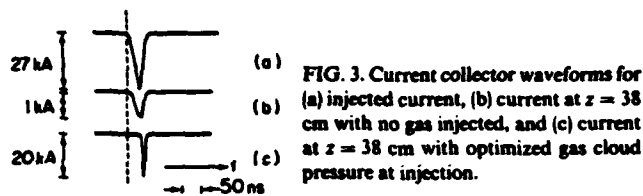FIG. 2. Injected gas presure profile at time of electron beam injection.

FIG. 3. Current collector waveforms for (a) injected current, (b) current at $z = 38$ cm with no gas injected, and (c) current at $z = 38$ cm with optimized gas cloud pressure at injection.

Drift tubes of different length were used, with a diameter of 15 cm in all cases. The vacuum maintained both upstream and downstream of the anode plane was in the range 10^{-5}–10^{-4} Torr, and no applied magnetic field was used in these experiments.

A. Puff valve ion source studies

In these studies, a well localized hydrogen gas cloud was produced on the downstream side of the anode by firing a fast gas puff valve a short time before electron beam injection. Fast ionization gauge measurements of the pressure profile downstream of the anode at the time of electron beam injection are shown in Fig. 2 and indicate that the gas was confined to a region within 3 cm of the anode. The peak pressure in the cloud at the time of electron beam injection can be varied over the range 0–100 mTorr. Under no circumstances was any significant gas pressure measured more than 4 cm from the anode plane. Typically, the delay between the discharging of the capacitor bank that fired the puff valve and the electron beam injection was 540 μsec. Ionization of
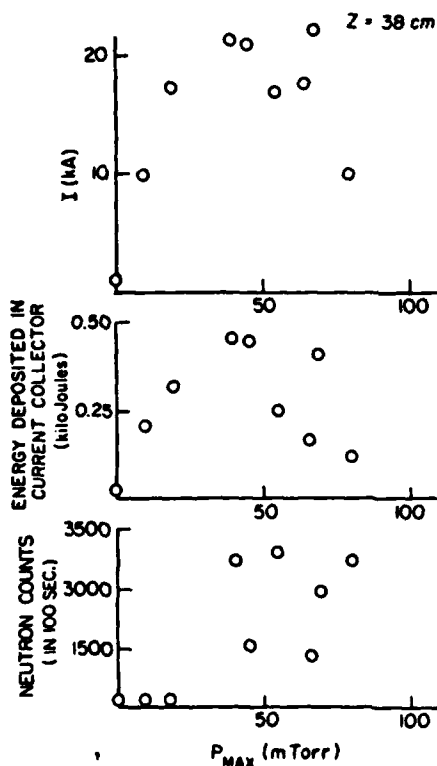

FIG. 5. As in Fig. 4, but $z = 48.3$ cm.

FIG. 4. Results of (a) current collector, (b) calorimeter, and (c) neutron detector measurements at $z = 38$ cm as a function of injected gas cloud peak pressure.
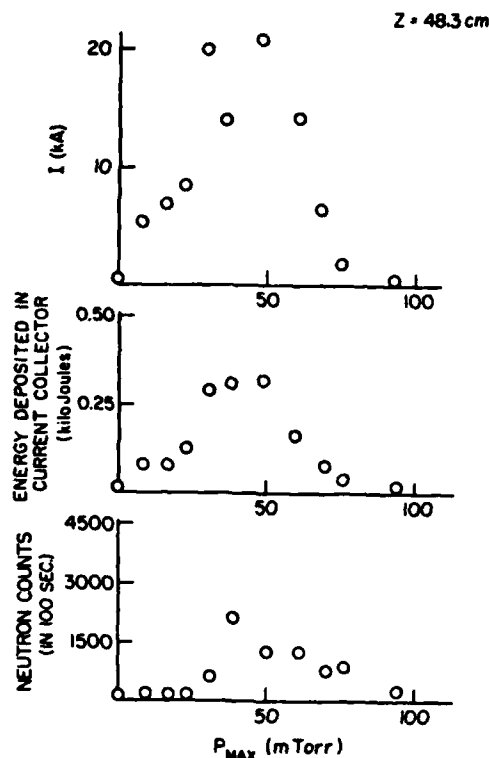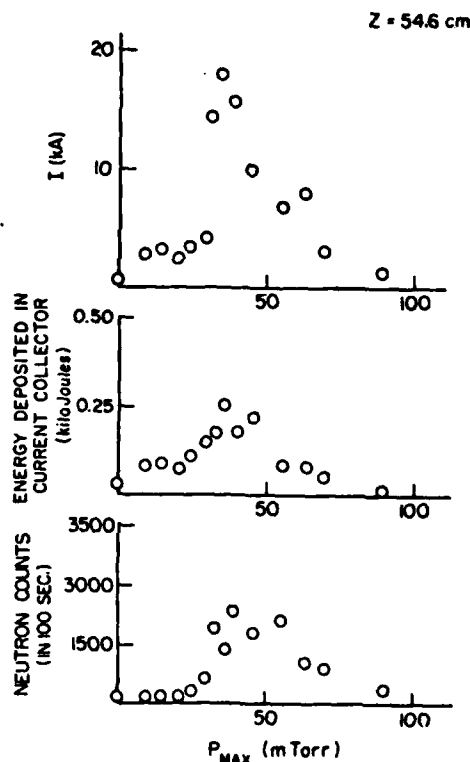

FIG. 6. As in Fig. 4, but $z = 54.6$ cm.

the gas results from electron impact ionization and, subsequently, from ion–ion avalanche ionization processes.

The current reaching a given position in the downstream drift tube was measured using a specially designed low-impedance current collector with a carbon beam stop 7.4 cm in diameter. The effective impedance of the current collector (14 mohms) is that of a thin stainless steel foil shunt through which the collected beam current passes to ground. Figure 3 shows typical current waveforms from the current collector for (a) the case where the collector was placed immediately downstream of the anode and, therefore, measures the injected current, (b) the case where the collector was placed at $z = 38$ cm downstream of the anode with no localized gas cloud present, and (c) the same conditions but a localized gas cloud with peak pressure of about 50 mTorr was present on the downstream side of the anode. These results will be discussed in detail in Sec. III.

A thermistor embedded in the carbon beam stop was used to measure the temperature rise of the beam stop and, therefore, obtain an estimate of the total beam energy (electrons and ions) propagating to a given axial position in the drift tube. This calorimeter was calibrated by moving the current collector/calorimeter to a position immediately downstream of the anode hole and measuring simultaneously the injected beam current and voltage waveforms and the temperature rise of the carbon beam stop. With a total deposited beam energy of approximately 1 kJ, the carbon beam stop temperature was increased by 12 °C, implying an effective beam stop mass of 117 g, compared with its actual mass of 191 g. Thus, each degree of temperature rise recorded may be assumed to result from about 80 J of beam energy deposition.
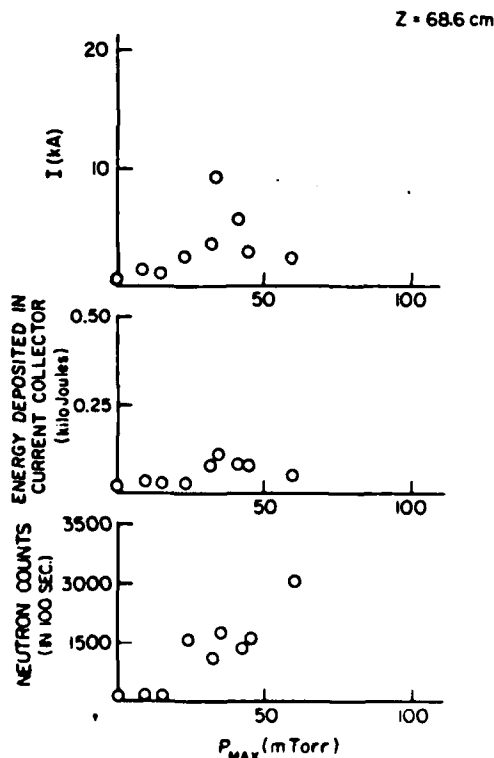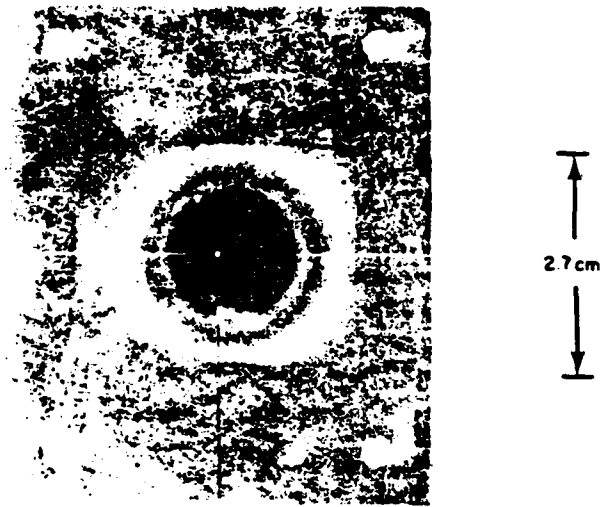

FIG. 8. Photograph of copper witness plate at $z = 70$ cm with optimized gas cloud pressure at injection.

As an additional diagnostic, a silver activation neutron detector was placed exterior to the drift tube. This detector was used to detect neutrons produced by accelerated protons striking the stainless steel drift tube wall. Since the many possible neutron producing reactions from the various constituents of stainless steel typically have threshold energies of several MeV, the production of significant neutron fluxes can be used as an indication that protons have been accelerated to energies in this range.

Figures 4–7 show the results obtained from all three diagnostics for beams injected through the localized gas cloud into evacuated drift tubes of axial lengths 38, 48, 55, and 67 cm, respectively. Several important features are readily apparent from these measurements:

(1) Without the localized gas cloud only about 1 kA or less of peak beam current is observed to propagate downstream.

(2) As the amount of gas injected to form the localized gas cloud is increased, the propagated beam current and total beam energy both rise to a maximum, then fall off as the pressure is further increased.

(3) The range of pressures at which the beam current can effectively propagate to a given axial position becomes more narrow as the axial position is increased.

(4) The net peak current (electrons + ions) measured by the collector at a distance of 55 cm downstream of the anode represents approximately 70% of the value of injected peak electron current; at 69 cm, the net current drops to about 30% of injected current.

(5) The arrival time of the peak electron current at the current collector at axial positions of 38 cm and greater is delayed, and the pulse width is narrowed with respect to the injected current waveform; this delay and the observed "beam front erosion" indicates, we believe, that electrons arriving at the collector originate from the rear part of the injected current pulse.

(6) Neutron production seems to correlate reasonably well with effective propagation of the electron beam.

FIG. 7. As in Fig. 4, but $z = 68.6$ cm.

1900   Phys. Fluids, Vol. 27, No. 7, July 1984

Destler, O'Shea, and Reiser   1900

Figure 8 is a photograph of a 20 mil thick copper witness plate placed 70 cm downstream of the anode and exposed to the beam under conditions where effective beam propagation is observed. The damage pattern results from thermal effects associated with beam energy deposition. The small size and circular symmetry of the witness plate damage pattern are a clear confirmation of the effective beam propagation that results from the localized gas cloud at the anode plane.

B. Laser plasma ion source

Some additional information on the propagation of beam energy under conditions where the beam is injected through a very dense ion source (to be compared with that obtained when the gas puff pressure was very high and little net current was measured at the collector) has been obtained using the configuration shown in Fig. 9. A Q-switched ruby laser (0.1 − 15 J, 15 nsec) is fired at a target immediately downstream of the anode about 1 μsec before the electron beam is injected. In this manner, a very dense plasma is produced and confined within 2 cm of the anode plane at the time of electron injection. At high laser energy (5 J) the particle densities available for ionization can be as high as 10^{16}–10^{18} cm^{-3} from such a source, much higher than the 10^{14}–10^{16} cm^{-3} densities available from the puff valve ion source.

Since high densities are produced over the entire operating range of the laser, the net collector currents measured at a given distance are very low when the 1 MeV, 27 kA, 30 nsec electron beam pulse is fired through the localized plasma created by the laser. This is consistent with the results obtained with the puff valve at high pressures. The acceleration of ions from the plasma by the injected electron beam has been checked independently by measuring the ion time of flight between two charge collection probes located 40 cm and 70 cm downstream of the anode plane, as shown in Fig. 9. A 1.5 kG deflecting magnet is used to sweep away accompanying electrons. Typical time of flight current waveforms are displayed in Fig. 10 for discharges in which the electron beam was fired through a localized plasma produced by firing the laser at a carbon target immediately prior to electron beam injection. The two cases displayed are for two laser
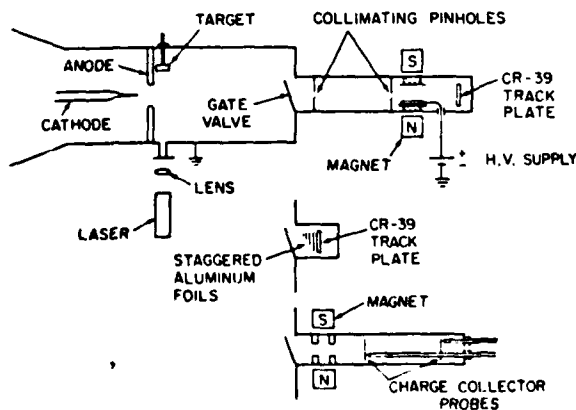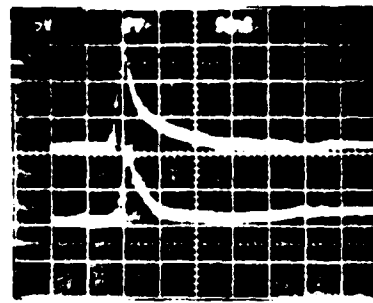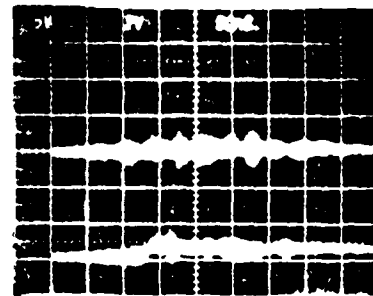
ION TIME OF FLIGHT SIGNALS

LASER ENERGY 0.3 Joules

front probe - 30 A/div

back probe - 4 A/div

LASER ENERGY 5 Joules

front probe - 30 A/div

back probe - 4 A/div

FIG. 10. Typical time of flight waveforms for laser energies of 0.3 J and 5 J, respectively (carbon target).

energies: 0.3 J and 5 J, respectively. The 0.3 J data show ion current signals which are much greater than any observed when the laser energy was 5 J, and which have a time of flight corresponding to peak ion energies of at least 10 MeV/amu. Previous results[9] reported by our group have indicated maximum ion energies in the range 2–5 MeV/amu. The higher

FIG. 9. Experimental configuration used for the laser ion source propagation studies.

FIG. 11. Typical Thomson parabolas for C^{+1}, C^{+2}, C^{+3}, and C^{+4} when laser is fired at a carbon target. Laser energy was 5 J (see Ref. 9).

ion energies observed in these experiments are attributed tentatively to the lower laser energy used in these experiments (0.3 J compared to 4–10 J for the previous studies) and a somewhat different target geometry that allows for a smaller effective ion source size at the time of electron beam injection. The data at 5 J laser energy are typical, exhibiting almost no net ion current at either probe.

Information from two other ion diagnostics, also shown in Fig. 9, contradict the obvious conclusion that few, if any, ions are accelerated in the case where the laser energy is 5 J. In fact, interestingly, Thomson Spectrometer data and range energy measurements both indicate that the peak ion current is substantially higher when the laser energy is 5 J than when it is 0.3 J. (A typical Thomson parabola obtained for the 5 J case is shown in Fig. 11.) A possible explanation of this phenomenon is that when the laser energy is high, the electron beam transfers energy to the laser plasma in a manner that results in a dense, charge-neutral, current-neutral flowing plasma (a "plasmoid") with sufficient density that the sweeping magnet can no longer separate the electrons from the ions. This possibility will be discussed in more detail in the next section.

III. SUMMARY OF RESULTS

The results of the experiments described in the previous section may be summarized as follows:

(1) Electron beam current in excess of the space-charge limiting value I_L (here $I_L < 8$ kA assuming that the radius of the beam is less than, or at best equal to, the current collector radius) may be propagated down an evacuated drift tube by providing a localized source of ions at the injection point.

(2) The propagation of electron beam current to a given axial position is critically dependent upon the peak pressure (and, therefore, the density of ions potentially available for neutralization) of the localized gas cloud used as the ion source. Thus it is clear that the propagation results from neutralization provided by the localized source, rather than from ions drawn off the walls of the drift tube or from the background vacuum.

(3) The observed propagated electron current waveforms arrive at the collector at a time late in the injected current pulse.

(4) The total energy deposited in the downstream collector is never more than 50% of the injected beam energy (at 38 cm) and decreases as the axial position of the collector is increased, even when the peak electron current collected remains about the same.

(5) Although effective electron beam propagation is not observed without ion acceleration, effective ion acceleration does not imply effective beam propagation in every case.

IV. DISCUSSION

The conclusions above support a description of the propagation process which we present here not as fact but rather as a plausible explanation of the observed phenomena. In this concept, the electron beam enters the drift tube at a current level several times the space-charge limiting value. Unable to propagate, the beam forms a virtual cathode immediately downstream of the anode plane, which remains

there until ionization processes produce the approximately 50% neutralization necessary for propagation. When this is achieved, the electron beam propagates to the edge of the ion cloud, forming the virtual cathode there. The electric fields associated with the virtual cathode draw ions downstream until the electron beam can propagate further into the vacuum drift region. This process may repeat itself until a channel of ions has been produced stretching from the anode to the downstream collector, at which time the remaining beam electron current at the back end of the pulse may flow through the channel at nearly the speed of light and be collected. Thus, the fraction of the injected current pulse that can propagate to the collector depends upon the time necessary to establish the ion channel. As the axial position of the collector is moved further downstream, the time needed to establish the ion channel increases until it becomes equal to the injected current pulse duration. At this point, the current observed at the collector falls to zero.

The dependence of the propagation on the injected gas pressure can be explained in a straightforward manner assuming that the above description of the propagation process is correct. At injected pressures too low for the most effective propagation, ions are not available in sufficient number to achieve radial force balance. Thus the beam spreads radially as it propagates, resulting in more current collected at $z = 38$ cm than at 58 cm, etc. As the injected gas pressure is increased, an optimum value is reached. Beyond this value, more ions than are required to produce the necessary partial charge neutralization are available, and the inertia of the excess ions slows the propagation velocity of the ionization channel. As a result, at higher pressures effective electron beam propagation cannot be achieved as far down the drift tube as is observed under optimum conditions.

This model of the propagation process can be checked in a straightforward manner by repeating the experiments using an electron beam generator with a longer pulse duration. Such experiments are planned for the near future.

The laser ion experiments are of interest because they represent the very high-pressure (or ion density) regime. In this case, it would be expected that a higher fraction of the electron beam energy would be converted to ion energy, that the electron beam would not propagate very far down the drift tube, and that a very dense moving plasma channel would result. In the experiments reported, there is indirect evidence of such a dense, charge-neutral, current-neutral plasmoid. When high laser energy is used, and, therefore, a very high number of ions are available for neutralization, we measure very little ion current on our time of flight current collectors even though two independent ion detection systems indicate that ions are present in quantity. To explain this phenomenon, we must examine under what conditions our deflecting magnet can sweep away the electrons in a flowing plasma, such that ion current could be measured with our time of flight current collectors.

Obviously, the Lorentz force $F_L = evB$ on an electron because of the external magnetic field must be greater than the focusing force F, because of the self fields. We can obtain a rough estimate by using Eq. (2) for F, setting $r = a$. The ratio of the two forces is then given by

$$\frac{F_s}{F_L} = \frac{I(1 - f_e - \beta^2)}{2\pi\epsilon_0 a\beta^2 c^2 B} = \frac{\mu_0}{2\pi} \frac{I(1 - f_e - \beta^2)}{a\beta^2 B}. \quad (6)$$

As an example, for a fully charge-neutralized beam ($f_e = 1$) with $I = 2.5 \times 10^4$ A, $a = 1 \times 10^{-2}$ m, $\beta^2 = 0.89$, and $B = 0.15$ T: $|F_s/F_L| \approx 3$, i.e., the self force at the edge of the beam exceeds the force caused by the sweeping magnet by a factor of three. Only for partial neutralization factors $f_e < 0.5$ does the external force exceed the force that keeps the beam together.

Thus, at high ion density, when $f_e > 0.5$, the deflecting magnet can no longer effectively sweep away the electrons, and little net current would be observed on our collectors. The fraction of injected beam energy that can be converted to a flowing plasma in this manner is not clear at this time, although calorimetry measurements indicate that it is less than 10% in these experiments. Experiments with larger diameter drift tubes, where the required fractional neutralization would be higher, may result in higher conversion efficiencies. Such experiments are also in the planning stages.

It is interesting to note that the results reported here are in apparent conflict with a number of numerical simulations of such systems.[12] In these numerical studies, an electron beam injected through a localized plasma does form a virtual cathode immediately downstream of the plasma, and ions are accelerated by the electric fields associated with the virtual cathode. But in all of these studies to date, the neutralization provided by the accelerated ions is small, and the virtual cathode does not move downstream at all. As a result, only an electron current comparable to the space-charge limiting current can propagate downstream, with the accelerated ions providing some radial force balance. In the experiments reported here, propagated current is at least three to four times the space-charge limiting value.

The propagation of charged particles in vacuum is of fundamental interest in many areas such as astrophysics, ion propulsion, laser fusion, etc. Alfvén,[6] in one of the first papers on this topic, studied the propagation of relativistic electrons through an interstellar plasma and concluded that the pinch force caused by the magnetic self-field of the electron stream results in the upper limit of $I_A = 17\,000\,\beta\gamma$ A for the current, as discussed in Sec. I. In the absence of a charge-neutralizing plasma or background gas, it is clear from our experimental results and the preceding discussion that effective propagation requires co-moving particles of opposite charge polarity to assure both full charge and current neutrality. Thus if an intense flux of relativistic electrons is ejected through the hot plasma on the surface of a star into free-space vacuum, the negative space charge forms a "virtual cathode" which acts like a mirror reflecting all electrons back towards the surface.[5,10] At the same time, the electric field associated with the virtual cathode extracts and accelerates positive ions from the plasma, and the reflecting space-charge mirror moves farther away from the surface. This collective acceleration process, which forces positive ions to follow the electrons is, in a sense, self-synchronizing and should continue, in principle, until the electron pulse terminates, or the supply of ions is cut off, or the co-moving ions at the front of the stream have reached the same velocity as the injected electrons. In the last case, no further electron

reflections occur at the front of the stream, and electrons and co-moving ions form a charge- and current-neutralized plasmoid. Thus, collective ion acceleration associated with the propagation of intense electron streams into free-space vacuum could play a role in the generation of high-energy cosmic rays, whose origin is still an open question,[13] and in other astrophysical processes.

The energetic positive ions observed in laser-produced plasmas and laser-target interaction experiments[14-17] are probably also produced by this mechanism. It is known that in laser-target interactions, a significant fraction of the absorbed laser energy is coupled into fast electrons with energies considerably higher than the mean energy of the thermal distribution. As these fast electrons escape from the surface, they charge up the target (if it is electrically insulated) or leave behind a positive image charge. In either case, after a sufficient number of fast electrons have escaped, a space-charge mirror forms, reflecting the electrons arriving later. The electric field associated with the mirror then extracts and accelerates positive ions from the surface plasma as described above. We hope that future results of our investigations will provide further understanding of the correlation between collective ion acceleration and beam propagation in vacuum.

ACKNOWLEDGMENTS

[1] R. B. Miller, *An Introduction to the Physics of Intense Charged Particle Beams* (Plenum, New York, 1982).
[2] M. Reiser, Phys. Fluids 20, 477 (1977).
[3] L. S. Bogdankevich and A. A. Rukhadze, Usp. Fiz. Nauk 103, 609 (1971) [Sov. Phys. Usp. 14, 163 (1971)].
[4] J. D. Lawson, J. Electron. and Control 3, 587 (1957); 5, 146 (1958).
[5] M. Reiser, in *Proceedings of the ECFA-RAL Meeting on The Challenge of Ultra-High Energies*, Oxford, 1982 (Rutherford-Appleton Laboratory, Chilton, Didcot, U.K., 1982), p. 131.
[6] H. Alfvén, Phys. Rev. 55, 425 (1939).
[7] To our knowledge, the first paper reporting experiments on electron beam propagation in a gas-filled drift tube is that by S. E. Graybill and S. V. Nablo, Appl. Phys. Lett. 8, 18 (1966).
[8] W. W. Destler, L. E. Floyd, and M. Reiser, IEEE Trans. Nucl. Sci. 26, 4177 (1979); Phys. Rev. Lett. 44, 70 (1980).
[9] J. T. Cremer and W. W. Destler, IEEE Trans. Nucl. Sci. 30, 3186 (1983).
[10] W. W. Destler, H. S. Uhm, H. Kim, and M. Reiser, J. Appl. Phys. 50, 3015 (1979).
[11] R. Adler, J. A. Nation, and V. Serlin, Phys. Fluids 24, 347 (1981); F. Mako, A. Fisher, N. Rostoker, and D. Tzach, IEEE Trans. Nucl. Sci. 26, 4199 (1979).
[12] See, for example, D. W. Swain, G. W. Kuswa, J. W. Poukey, and C. C. Olson, in Proceedings of the IXth International Conference on High Energy Accelerators, SLAC, Stanford, CA, May 2-7, 1974; or R. J. Faehl (private communication).
[13] A recent review on the topic of acceleration of galactic cosmic rays was given by W. I. Axford, in *Origin of Cosmic Rays*, edited by G. Setti, G. Spada, and A. W. Wolfendale (Reidel, Dordrecht, Holland, 1981), p. 339.
[14] J. S. Pearlman and G. H. Dahlbacka, Appl. Phys. lett. 31, 414 (1977).
[15] Y. Gazit, J. Delettrez, T. C. Bristow, A. Entenberg, and J. Soures, Phys. Rev. Lett. 43, 1943 (1979).
[16] G. D. Tsakiris, K. Eidmann, R. Petsch, and R. Sigel, Phys. Rev. Lett. 46, 1202 (1981).
[17] H. Hora, in *Laser Interaction and Related Plasma Phenomena*, edited by H. Hora and G. H. Miley (Plenum, New York, 1983), Vol. 6.

Intense relativistic electron beam propagation in evacuated drift tubes

P. G. O'Shea, D. Welsh, W. W. Destler, and C. D. Striffler

Laboratory for Plasma and Fusion Energy Studies and the Electrical Engineering Department, University of Maryland, College Park, Maryland 20742

The propagation of a magnetically confined intense relativistic electron beam (IREB) (1 MeV, 27 kA, 20 ns FWHM) in vacuum drift tubes has been studied experimentally and theoretically. Experimental results for current propagation as a function of uniform applied magnetic field (0–1.2 T) are presented for various drift tube diameters, cathode geometries, and anode aperture sizes. An analytic model of laminar beam flow is presented which predicts the space-charge-limited current of a solid IREB propagating in a grounded drift tube. A steady-state equilibrium is examined and is compared with the experimental results.

PACS numbers: 41.80.Dd, 52.40.Mj, 52.60. + h, 41.70. + t

I. INTRODUCTION

In recent years, the generation and propagation of intense relativistic electron beams (IREB) have been the subjects of many theoretical and experimental studies, in part due to the various applications of such beams in such diverse fields as high power coherent radiation source development,[1-3] collective ion acceleration,[4-7] and plasma heating and confinement.[8,9] A summary of the field prior to 1982 is presented in the book by R. B. Miller.[10]

With respect to beam propagation, one distinguishes between (a) propagation in vacuum, (b) propagation in a plasma, and (c) propagation in a neutral gas. Each of these areas can be divided into operating regimes which depend on the focusing field in (a), on plasma density and temperature in (b), and on the gas pressure in (c). Furthermore, beam propagation can be described in terms of fundamental limits such as the space-charge-limiting current I_L in (a), the Alfvén–Lawson current I_A in (b) and (c), or other limiting effects such as instabilities. Thus, in a vacuum drift tube and in the absence of charge neutralizing positive ions, an IREB with a current $I < I_L$ can propagate and then over significant distances only if a focusing magnetic field is present. A distinction is made between systems in which the cathode is either immersed or not immersed in the confining magnetic field.[11] In the former case, one finds that in the regime of high magnetic field $(B \to \infty)$ the electrons are forced to move along field lines. The space-charge-limiting current in this extreme is the well-known formula for I_L by Bogdankevich and Rukhadze,

$$I_L = I_0 \frac{(\gamma_0^{2/3} - 1)^{3/2}}{1 + 2 \ln \dfrac{R_w}{R_b}}, \tag{1}$$

where $I_0 = 4\pi\epsilon_0 mc^3/q = 1.7 \times 10^4$ A for electrons, R_b = beam radius, R_w = radius of the drift tube, and $(\gamma_0 - 1)mc^2 = eV_0$ = kinetic energy of the electron at the plane of injection into the drift tube. In actual laboratory experiments where the magnetic field is typically constrained to values in the range 0–2 T, this result must be modified to include internal electron beam dynamics in such systems.

Both analytical theories and numerical simulations of such systems have been reported,[12-17] but to date a systematic experimental study of these phenomena has not been available for comparison with theory and simulation. In this paper, we describe the results of an experimental study of intense electron beam propagation in evacuated drift tubes of various diameters in the presence of a nearly uniform applied magnetic field. These results, presented in Sec. II, are then compared to results expected from an analytical model presented in Sec. III. Conclusions are drawn in Sec. IV.

II. EXPERIMENTS

The general experimental configuration is shown in Fig. 1. An intense relativistic electron beam (1 MeV, 27 kA, 30 ns FWHM) was field emitted from a 1-cm-diam stainless steel cathode situated 1.2 cm upstream of a stainless steel anode plate. Two different cathode geometries were used as shown in Fig. 2, and will be referred to as "solid" and "hollow" cathodes, respectively. Anode apertures of 1.2 and 2.6 cm were used in combination with stainless steel drift tubes
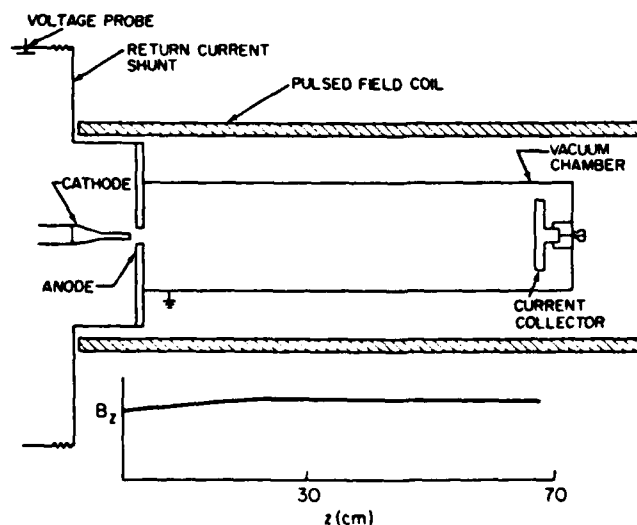

FIG. 1. Experimental configuration and applied axial magnetic field profile.
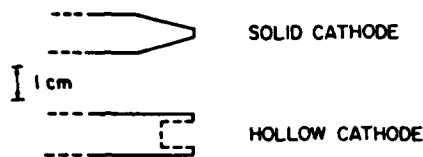
FIG. 2. "Solid" and "hollow" cathode geometries.

of 3.8, 9.8, and 14.8 cm i.d. An axial magnetic guide field in the range 0–1.2 T constrained the radial motion of the beam electrons over the entire experimental length from cathode to current collector. The beam current propagating to the end of the drift tube was measured using a low impedance current collector. In the collector, electron current was absorbed in a graphite beamstop and flowed to ground through a 14-mΩ stainless steel foil shunt. The injected beam current was measured by placing the collector 2 cm downstream of the anode plane and was found to be consistently 27 ± 1 kA with no appreciable variation with applied magnetic field. The vacuum maintained both upstream and downstream of the anode was in the range 10^{-5}–10^{-4} Torr.

The peak electron beam current I measured at the downstream end of the 70-cm-long drift tube as a function of applied magnetic field B is shown in Figs. 3 and 4 for the various geometries considered. Characteristic oscilloscope traces, giving beam current as a function of time, are shown in Fig. 5.

The following important features are apparent from our measurements.
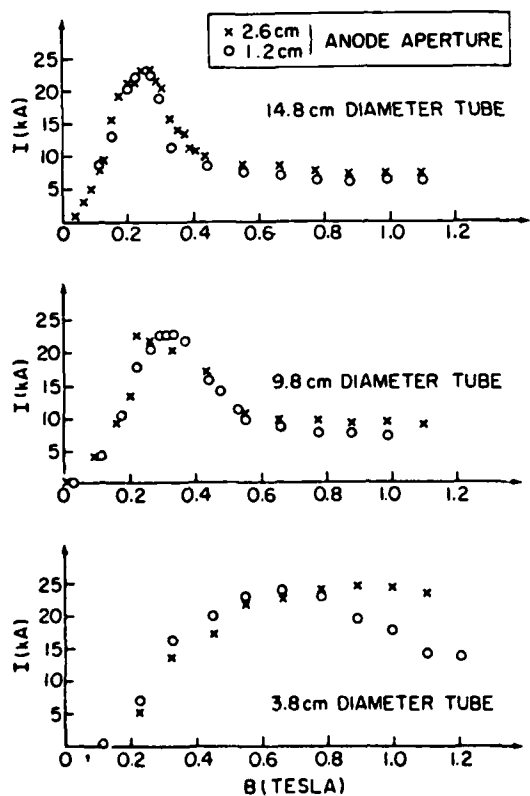

FIG. 3. Peak propagating current measured at current collector for 14.8-, 9.8-, 3.8-cm-diam drift tubes, and 2.6- and 1.2-cm-diam anode apertures using *solid cathode*.
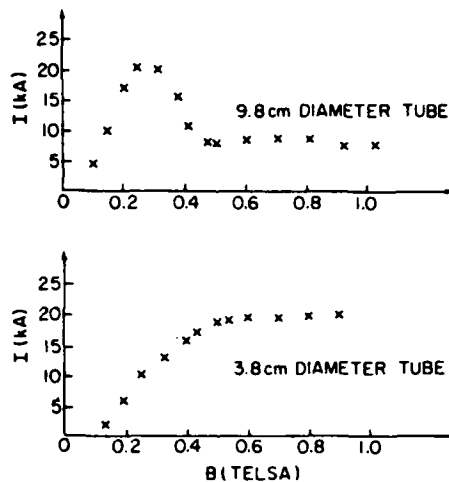

FIG. 4. Peak propagating current measured at current collector for 9.8- and 3.8-cm-diam drift tubes with 2.6-cm-diam anode aperture and *hollow cathode*.

(1) Without applied magnetic field, less than 0.5 kA of beam current was observed to propagate to the end of any of the drift tubes.

(2) In all tubes there appear to be three distinct regimes of beam propagation. However, these distinctions are more obvious in the 14.8- and 9.8-cm-diam tube results.

(a) *Low magnetic field.* Propagating current initially rises as B is increased from zero. Here we have a poorly confined beam, a significant fraction of which may hit the tube wall and be lost. As B increases, the beam confinement improves and more current propagates.

(b) *Intermediate magnetic field.* Beam current decreases rapidly with increasing B, and space-charge effects due to the relationship between beam and tube radius are playing an increasingly significant role in this region.

(c) *High magnetic field.* A plateau region where the change in propagating current is small as B increases.

(3) As tube diameter decreases, the region of maximum current propagation shifts to higher magnetic fields and also the propagating current in the high field plateau region increases.

(4) For the 14.8- and 9.8-cm-diam tubes, changing the anode aperture size from 1.2 to 2.6 cm diam did not greatly
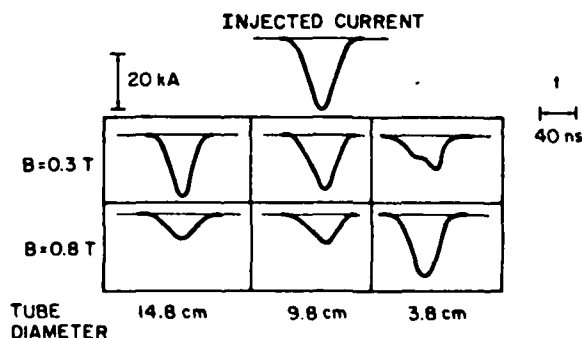

FIG. 5. Oscilloscope tracings of typical current collector pulse shapes, indicating injected current waveform and downstream current waveform, for applied magnetic fields of 0.3 and 0.8 T in 14.8-, 9.8- and 3.8-cm-diam drift tubes using 2.6-cm-diam aperture and solid cathode.
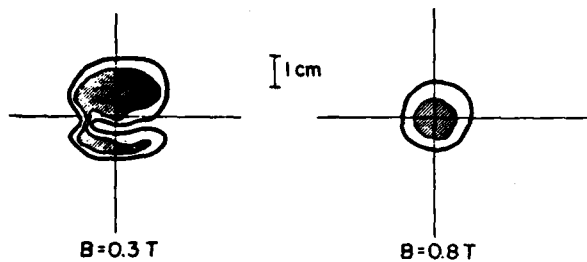
FIG. 6. Tracings of witness plate damage patterns for applied magnetic fields of 0.3 and 0.8 T in 3.8-cm-diam tube using 2.6-cm-diam anode aperture and solid cathode. Shaded areas indicate region of most intense damage. Outer boundary indicates extent of observable damage.

alter the propagating current except in the high field plateau region. However, we note significant difference in the current characteristics for the high field region between the 1.2- and 2.6-cm anode hole cases for the 3.8-cm tube. This is due to the fact that the anode diameter is a significant fraction of the tube diameter. The smaller anode hole case appears to exhibit similar features in the region $0.8 \lesssim B \lesssim 1.1$ T as the large tubes do in the range $0.3 \lesssim B \lesssim 0.5$ T. We have evidence that the current propagating in this tube for the 2.6 anode begins to decrease at $B = 1.2$ T and above, but limitations on our pulsed magnetic field coils prevent us from operating reproducibly in this region.

(5) The hollow cathode data differs from the solid cathode data primarily by a small difference in the magnitude of the propagated currents as a given magnetic field.

The fact that the smallest tube can propagate as much current at high B as the large ones can at considerably lower B removes from consideration the possibility that some form of magnetic mirroring, resulting from nonuniformity of the applied field causes the observed reduction of current in the large tubes at high magnetic field.

A further series of experiments was carried out using the solid cathode and 9.8-cm drift tube in which the 2.6-cm anode hole was covered at the cathode side by a 25-μ-thick titanium foil. In these tests, no significant deviations from the current propagation characteristic of the foilless diode case were observed.

Experiments were also performed to measure the beam cross section at the downstream end of the 9.8-cm drift tube using Mylar witness plates. Two characteristic witness plate patterns are exhibited in Fig. 6. For $B \gtrsim 0.4$ T, the pattern is circular and well defined, the diameter being approximately constant 2.3 cm. However, for $0.2 < B < 0.4$ T, the pattern indicated a filamentary beam such as the bifurcated pattern shown for 0.3 T. Tests with axially stacked plates indicate that this filamentary pattern was rotating about the axis of propagation. Such patterns appear to be characteristic of an $m = 2$ or higher-order type instability of the beam in the high current propagation region.

III. MODEL OF SOLID BEAM EQUILIBRIUM

A steady-state model of an intense relativistic electron beam in an axis-symmetric system can be constructed by conserving single particle energy, conserving canonical angular momentum, applying continuity of current, and main-

taining force balance on each element of the beam. The parameters we consider are shown in Fig. 7, and they represent the experimental system discussed in Sec. II. Specifically, we assume that a solid, uniform density electron beam of radius R_a is injected into a long grounded cylindrical drift tube of radius R_w. The injected beam is irrotational and monoenergetic with energy $mc^2(\gamma_0 - 1) = eV_0$. After the beam passes through the anode end of the drift tube, we assume it expands adiabatically to a radius R_b where a laminar flow equilibrium is set up far from the end walls. The entire system is immersed in a uniform axial magnetic field B_{AZ}. The downstream beam properties are the charge density $\rho(r)$, and the azimuthal and axial velocities, $V_\phi(r)$ and $V_z(r)$. We assume the fields generated by the beam are confined inside the drift tube. These self-fields, which are shown in Fig. 7, include the radial electric field $E_{sr}(r)$ as well as the azimuthal and axial magnetic fields, $B_{s\phi}$ and B_{sz}.

To further simplify the analysis, we assume the equilibrium beam density is constant across the beam cross section, $\rho(r) = \rho_b$. Because of this assumption, the electric potential $\phi(r)$ and the electric field $E_{sr}(r) = -\partial\phi(r)/\partial r$ are easily calculated. Now by conserving single particle energy, we can write the kinetic energy of the beam, KE $= mc^2[\gamma(r) - 1]$ in terms of the electric potential,

$$\gamma(r) = \gamma_0 + \frac{e}{mc^2}\phi(r) = \frac{1}{\sqrt{1 - \beta_\phi^2(r) - \beta_z^2(r)}}, \qquad (2)$$

where

$$\phi(r) = \frac{\rho_b R_b^2}{4\epsilon_0}\left(1 - \frac{r^2}{R_b^2} + 2\ln\frac{R_w}{R_b}\right), \qquad (3)$$

$\beta_\phi(r) = V_\phi(r)/c$ and $\beta_z(r) = V_z(r)/c$.

In a laminar flow beam of uniform density, the relative radial position of an electron in the beam is constant regardless of beam radius, i.e., $r_a/R_a = r/R_b$ where r_a is the radial position of the particle as it passes through the anode plane and r is the radial position of the particle downstream. For this case, canonical angular momentum is conserved totally in terms of the downstream beam radius. We obtain

$$-\frac{eB_{AZ}r_a^2}{2} = -\frac{eB_{AZ}r^2}{2}\left(\frac{R_a}{R_b}\right)^2 = r[m\gamma(r)V_\phi(r) - eA_\phi(r)], \qquad (4)$$

where $A_\phi(r)$ is the downstream total azimuthal component of the magnetic vector potential. Solving Eq. (4) for $V_\phi(r)$ and substituting it into $J_\phi(r) = \rho_b V_\phi(r)$, noting that $A_\phi(r)$
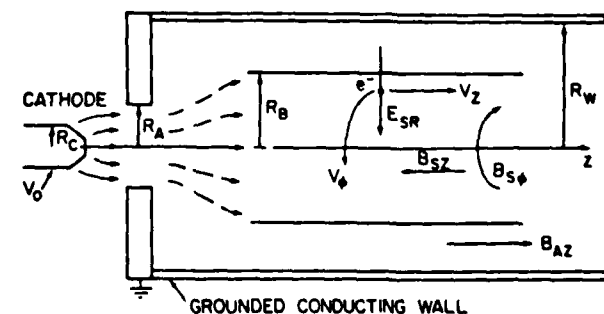

FIG. 7. Schematic of beam model.

$= rB_{AZ}/2 + A_{s\phi}(r)$, we obtain from Maxwell's Equations, $\nabla \times \mathbf{B}_s = -\nabla^2 \mathbf{A}_s = \mu_0 \mathbf{J}_s$,

$$\frac{\partial}{\partial r} \frac{1}{r} \frac{\partial}{\partial r} rA_{s\phi}(r) + \frac{e}{m} \frac{\mu_0 \rho_b}{\gamma(r)} A_{s\phi}(r)$$

$$= -\frac{1}{2} \frac{e}{m} \frac{\mu_0 \rho_b}{\gamma(r)} B_{AZ}\left(1 - \frac{R_a^2}{R_b^2}\right) r, \quad 0 < r < R_b , \quad (5a)$$

$$\frac{\partial}{\partial r} \frac{1}{r} \frac{\partial}{\partial r} rA_{s\phi}(r) = 0, \quad R_b < r < R_w . \quad (5b)$$

After expanding $\gamma(r)$ in terms of ρ_b from Eq. (2), Eq. (5) can be solved by Frobenius' Method. The boundary conditions are: $A_{s\phi}(r = 0) = 0$, $A_{s\phi}$ and B_{sz} are continuous across the beam edge $r = R_b$, and $A_{s\phi}(r = R_w) = 0$. The general solution inside the beam is

$$A_{s\phi}(r) = \frac{B_{AZ}\left(1 - \frac{R_a^2}{R_b^2}\right)r}{2(1 + \xi)}$$

$$\times \left[-\xi + \sum_{n=1}^{\infty} \prod_{i=1}^{n} \frac{i(i-1) - 1}{i(i+1)} K^n \left(\frac{r}{R_b}\right)^{2n} \right], \quad (6)$$

where

$$K = \frac{\frac{1}{4}\frac{e}{m}\mu_0 \rho_b R_b^2}{\gamma_0 + \frac{1}{4}\frac{e}{m}\mu_0 \rho_b R_b^2 \left(1 + 2\ln\frac{R_w}{R_b}\right)}$$

and

$$\xi = \sum_{n=1}^{\infty} \prod_{i=1}^{n} \frac{i(i-1) - 1}{i(i+1)} K^n \left[n\left(1 - \frac{R_b^2}{R_w^2}\right) + 1 \right].$$

Now $B_{sz}(r)$ is computed from $\mathbf{B}_s = \nabla \times \mathbf{A}_s$, and $V_\phi(r)$ is calculated from Eq. (4). Then, $V_\phi(r)$ and Eq. (2) are used to find $V_z(r)$. Finally, the azimuthal self-magnetic field $B_{s\phi}(r)$ can be calculated from $V_z(r)$ and Ampere's Law.

At this point, the functional forms of all the equilibrium beam properties have been found in terms of R_a, R_b, R_w, γ_0, B_{AZ}, and the beam density ρ_b. These quantities can be determined by requiring each volume element of the beam to be in radial force balance. Radial force balance can be written

$$\frac{m\gamma(r)V_\phi^2(r)}{r} = e\left\{E_{sr}(r) + V_\phi(r)[B_{AZ} + B_{sz}(r)]\right.$$

$$\left. - V_z(r)B_{s\phi}(r)\right\} \quad (7)$$

for our model. To solve this equation, R_a, R_b, R_w, γ_0, and B_{AZ} are held fixed while ρ_b is varied until the "best possible equilibrium" is found. Because of our uniform density assumption, there is no total radial force balance, but Fig. 8 shows a typical "best possible equilibrium" and the net force balance is good. All of our "equilibria" had three features in common with Fig. 8: (a) there is exact force balance between $r/R_b = 0.5$ and $r/R_b = 0.6$, (b) the net radial force is smaller than any of the individual forces, and (c) the force imbalance shows a stable configuration with outward forces in the beam's core and inward forces on the beam's edge. The velocity profiles for this beam are included for completeness. After calculating the beam density for an equilibrium, the axial beam current is calculated from

(a)

$\frac{r}{R_b}$: RADIAL POSITION WITHIN BEAM

(b)
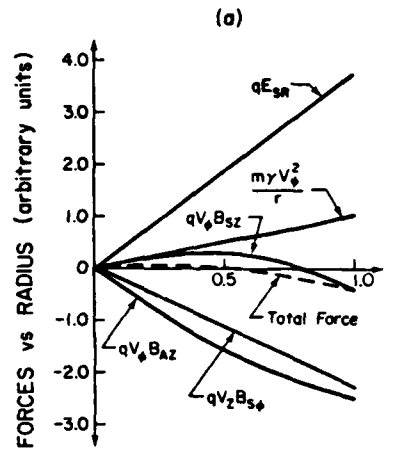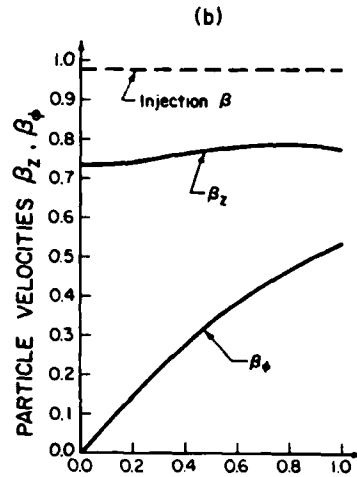
$\frac{r}{R_b}$: RADIAL POSITION WITHIN BEAM

FIG. 8. Equilibrium force and velocity profiles for typical downstream beam. The parameters are : $R_a = 1.3$ cm, $R_w = 4.8$ cm, $\gamma_0 = 3.5$, $B_{AZ} = 0.16$ T, $R_b = 4.0$ cm, and $I = 19.4$ kA. Point D of Figs. 9 and 10.

$$I = 2\pi\rho_b \int_0^{R_b} V_z(r) \, r dr , \quad (8)$$

where we have assumed this current equals the injected current.

A set of results displaying the interdependencies of all the variables is shown in Fig. 9. The fixed parameters are $R_a = 1.3$ cm, $R_w = 4.8$ cm, and $\gamma_0 = 3.5$ (a 1.28-MeV beam). We have plotted normalized electrostatic potential on the beam axis, $\phi(r = 0)/eV_0$, versus beam current I in kA. The solid lines represent constant beam radii R_b and the dashed lines represent constant applied magnetic field B_{AZ}. One can read this graph as follows; choose an applied magnetic field B_{AZ} and an injected current, then follow the magnetic field line until the current is reached. If this is not possible, the maximum current propagated is less than the injected current for this B_{AZ}. Otherwise, the beam has expanded to a radius R_b and has attained radial force balance.
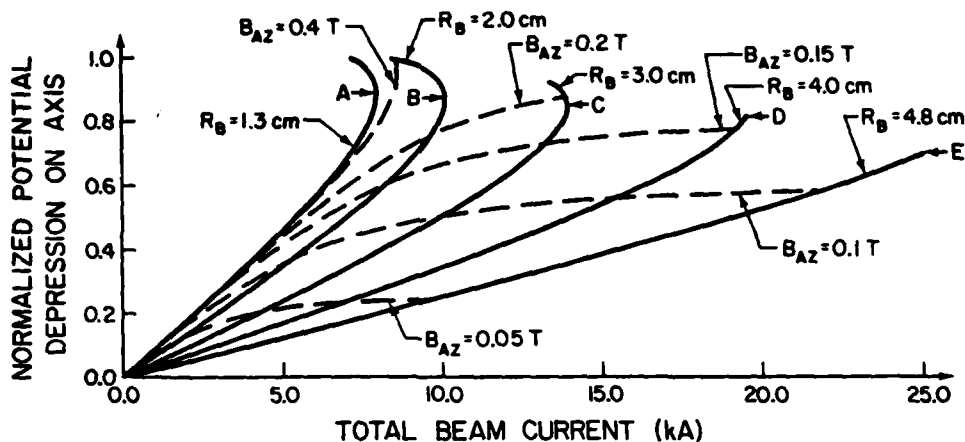
FIG. 9. Downstream beam properties for $R_a = 1.3$ cm, $R_w = 4.8$ cm, and $\gamma_0 = 3.5$. Normalized potential depression on axis vs axial current with beam radius R_b and applied magnetic field B_{AZ} as parameters.

As an example, if $B_{AZ} = 1.0$ kG and 10 kA is injected, the beam expands to $R_b = 3.0$ cm and the potential depression on the beam axis is 0.5 of the diode potential. Notice that no more than 22 kA will propagate at 1.0 kG.

To compare the theoretical predictions to the experimental results, we generated Fig. 10 from the data in Fig. 9. This is done by starting at the infinite magnetic field limit where $R_b = R_a$. The maximum current propagated for this situation is about 8 kA and is indicated by Point A in Fig. 9. Point A and the Bogdankevich–Rukhadze limiting current of Eq. (1) are both displayed in Fig. 10 ($I_{BR} = I_L$). Now, as the magnetic field is lowered, the beam will expand to some new $R_b > R_a$. When $R_b = 2.0$ cm, the necessary applied field for maximum current propagation is approximately 2.5 kG, and $I_{max} = 10$ kA (Point B). Following this argument generates the I_{max} vs B_{AZ} curve from Point A through Point B to Point C. In this region, the beam current is space charge limited. This means the electrostatic potential energy of the beam near the axis is large enough to regulate the current flow. For example, if the beam density were increased at Point B, less current would flow because the center of the beam has so little kinetic energy.

As the magnetic field is decreased from its value at Point C, the beam continues to expand, and the limiting current moves from Point C through Point D to Point E in Fig. 9. For magnetic field strengths in this regime, the lines of constant beam radius end prematurely at Points D and E

because the current is limited by the total field energy of the beam. If the current density increases for the beam at Point D or E, the field energy generated by the beam becomes larger than the kinetic energy of the beam and steady state cannot be achieved.

Finally, for magnetic fields lower than at Point E, the beam fills the drift tube $R_b = R_w$ and current is limited by the size of the tube. In Fig. 11, we have generated the I_{max} vs B_{AZ} curve for a wall radius $R_w = 1.905$ cm, $\gamma_0 = 3.5$, and two different anode radii, $R_a = 1.27$ and 0.635 cm. For these cases, I_{BR} is shown for reference.

In comparing Figs. 3, 10, and 11, it is clear that the theory predicts all the trends discussed in Sec. II. The only disagreement is the magnitude of the applied magnetic field. Here, the theory is off by approximately a factor of 2. It is expected that cyclotron motions, other nonlaminar effects, and nonadiabatic expansions will account for some of this discrepancy.

IV. SUMMARY AND DISCUSSION

We have performed experiments to determine the maximum current that can propagate down a cylindrical drift tube. The current source is nominally a 1-MV, 30-kA, 30-ns electron beam which enters one end (that serves as the anode) of a long cylindrical tube ($L > R$). The maximum propagated
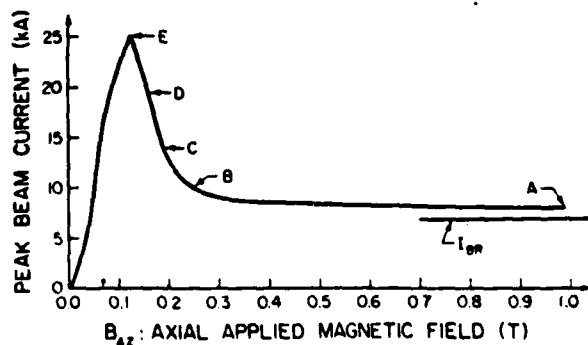

FIG. 10. Maximum beam current vs applied magnetic field for $R_a = 1.3$ cm, $R_w = 4.8$ cm, and $\gamma_0 = 3.5$. The same case as Fig. 9.
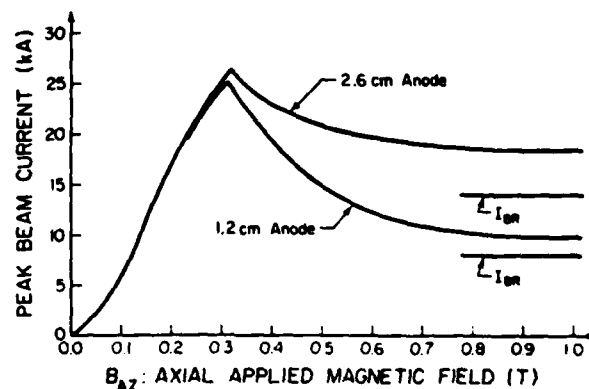

FIG. 11. Maximum beam current vs applied magnetic field for $R_w = 1.9$ cm and $\gamma_0 = 3.5$. Two different anode sizes are shown: $R_a = 0.6$ cm and $R_a = 1.3$ cm.

current is examined as a function of tube radius, anode hole size, and applied magnetic field. For solid cathodes these results are displayed in Fig. 3 and for a hollow cathode in Fig. 4.

In an attempt to understand these results, a steady-state, azimuthally symmetric beam model is presented and self-consistently solved to determine the downstream beam properties for an injected solid, monoenergetic, uniform current density electron beam. Further restrictions of the model are laminar flow and uniform charge density after it has reached an axial position. These results, in the same form as the experimental results, are shown in Figs. 10 and 11. Detailed comparisons should only be made between the solid cathode data of Fig. 3 and the analytical results of Figs. 10 and 11.

The model and experiments agree with respect to general shape of the maximum current as a function of applied magnetic field. This is true for all variations in the ratio of tube radius to anode hole size. The three regimes of magnetic field operation are: low field regime, where the beam is poorly confined and a significant fraction is lost to the tube walls; intermediate field regime, where the beam current is confined within the tube walls but space-charge potential depression causes a decrease in net current propagated; and high field regime, where the net current propagated remains relatively constant with further increase in the field. The model and experiment agree with the uncertainty of the diode voltage as to the quantitative peak value of the current as well as the propagated current in the high magnetic field regime. The main disagreement between the model and experiments is the value of the magnetic field at which the peak current propagates. This value is a factor of 2 larger in the experiments than in the model.

We would like to comment on a few effects which we believe could be important and would help to explain some of our differences. The full injected current of 30 kA is never seen to propagate the length of the system. Thus, in almost all experiments a virtual cathode is formed near the entrance end of the drift tube. Clearly the analytic model does not include this condition or the effects resulting from it. The actual radial extent of the virtual cahtode is probably a strong function of magnetic field and a more appropriate model should think of the virtual cathode as the entering surface versus the anode plane. A related issue is the laminar flow assumption in our model. Initial analytic studies involving cyclotron orbit effects indicate a shift of the I_{max} vs B_{AZ} curve to higher values of B_{AZ}.

In summary, the comparisons between an experiment and a fairly simple model that concentrates on determining the maximum current that can propagate in an evacuated drift tube as a function of applied magnetic has produced fairly good agreement and understanding of this system.

ACKNOWLEDGMENTS

[1] J. L. Herschfield and V. L. Granatstein, IEEE Trans. Microwave Theory Tech. MTT-25, 522 (1977).

[2] E. Ott and R. V. Lovelace, Appl. Phys. Lett. 27, 378 (1975).

[3] G. Bekefi and T. J. Orzechowski, Phys. Rev. Lett. 37, 379 (1976).

[4] C. L. Olson and U. Schumacker, in Springer Tracts in Modern Pysics: Collective Ion Acceleration, edited by G. Hobler (Springer, New York, 1979).

[5] S. Graybill and J. Uglum, J. Appl. Phys. 41, 236 (1970).

[6] W. W. Destler, L. E. Floyd, and M. Reiser, Phys. Rev. Lett. 44, 70 (1980).

[7] R. Adler, J. A. Nation, and V. Serlin, Phys. Fluids 24, 347 (1981).

[8] C. A. Kapetanakos and W. M. Black, Bull. Am. Phys. Soc. 18, 1264 (1973).

[9] M. Friedman, Phys. Rev. Lett. 24, 1098 (1970).

[10] R. B. Miller, An Introduction to the Physics of Intense Charged Particle Beams (Plenum, New York, 1982).

[11] M. Reiser, Phys. Fluids 20, 477 (1977).

[12] L. S. Bogdankevich and A. A. Rukhadze, Usp. Fiz. Nauk. 103, 609 (1971) [Sov. Phys. Usp. 14, 163 (1971)].

[13] J. R. Thompson and M. L. Sloan, Phys. Fluids 21, 2032 (1978).

[14] L. E. Thode, B. B. Godfrey, and W. R. Shanahan, Phys. Fluids 22, 747 (1979).

[15] P. G. O'Shea, W. W. Destler, C. D. Striffler, and D. Welsh, Bull. Am. Phys. Soc. 27, 983 (1983).

[16] W. W. Destler, P. G. O'Shea, M. Reiser, C. D. Striffler, D. Welsh, and H. H. Fleishmann, IEEE Trans. Nucl. Sci. NS-30, 3183 (1983).

[17] D. Welsh, C. D. Striffler, P. G. O'Shea, and W. W. Destler, Bull. Am. Phys. Soc. 28, 1039 (1983).

OPERATION OF A PLASMA FOCUS DEVICE AS A
COMPACT ELECTRON ACCELERATOR

John R. Smith
Naval Surface Weapons Center
White Oak, Silver Spring, Maryland 20910

C. M. Luo[a], M. J. Rhee, and R. F. Schneider
Laboratory for Plasma and Fusion Energy Studies
University of Maryland
College Park, Maryland 20742

ABSTRACT

The electron beam produced by a compact plasma focus device has been investigated. The Mather geometry plasma focus electrodes were modified to permit extraction of accelerated electrons. Performance of the plasma focus as an electron accelerator using different gas species and pressures is investigated. Also, results on measurements of the beam parameters are given.

[a]On leave from Tsinghua University, Peking, China.

Many laboratories have observed energetic ions[1-10] and electrons[9-13] in plasma focus experiments. Both ions and electrons with energies of several hundred keV and above have been reported. These energies compare with a typical device charging voltage of 20 to 50 kV. The plasma focus device at the University of Maryland is one of the smallest such experiments with approximate dimensions of 0.5 x 0.5 x 1.5 m. This device has previously achieved ion energies as high as 1 MeV.[1] The advantage of compactness and possibility of high electron energy was the motivation to study the operation of a plasma focus device as a compact electron accelerator.

The typical plasma focus consists of a capacitor bank, spark gap switch, transmission line, and coaxial plasma gun. The spark gap is triggered and raises the anode of the plasma gun to high voltage. Gas breakdown occurs initially across the surface of the insulator separating the plasma gun's anode and cathode. The resulting plasma sheath is accelerated axially down the plasma gun by the $j_r B_\theta$ force. Upon reaching the open end of the plasma focus gun the sheath pinches radially due to the $j_z B_\theta$ force. Subsequently the $m = 0$ sausage instability causes a current interruption associated with the acceleration of ions and electrons from the plasma.

Most plasma focus experiments use either cables or parallel plate transmission lines to connect the capacitors to the plasma gun. Our system is unique in that it uses a dielectric filled coaxial transmission line. Analysis of the system by treatment of the coaxial line as a current charged transmission line and the unstable plasma as an opening switch is given in Ref. 14. Fast, high-voltage pulses may be created which are capable of

2

accelerating particles out of the dense plasma. The pulse height and width in theory may be changed by choice of the dielectric material used to fill the transmission line.

The five major components of the plasma focus device used in this work are shown in Fig. 1. They are: (1) 15 μF, 3 kJ capacitor, (2) triggered spark gap, (3) coaxial transmission line, (4) inverted Mather type plasma gun, and (5) drift chamber. Typically the energy storage capacitor is charged to 18 kV and is discharged into the coaxial transmission line with a single pressurized spark gap switch. The transmission line is filled with water for this work and has a characteristic impedance of 7Ω with the following dimensions: outer conductor diameter - 14.5 cm, inner conductor diameter - 5.1 cm, length - 30 cm.

In the ion acceleration work described in Ref. 1 we used a standard Mather geometry plasma gun which was attached to the end of the transmission line. Ions are accelerated out of the focussed plasma and away from the plasma gun, while electrons derived from the plasma are accelerated into the center of the anode. Since the location of the transmission line prohibits extraction of electrons a modified plasma gun was designed. In essence the Mather gun used in the ion acceleration work was inverted as shown in Fig. 2. The center conductor of the transmission line (charged negatively) is attached to the outer conductor (cathode) of the plasma gun. The transmission line's outer conductor is folded inward to become the center conductor (anode) of the plasma gun. Electrons are extracted from the hollow anode

3

(1 cm i.d.) and enter a 10 cm diameter drift region which is filled with the same gas as the plasma gun. In Fig. 2 are typical traces of the machine voltage and current and the net current at the drift tube entrance.

Filling gases of hydrogen, helium, nitrogen or argon were used. Gas pressure was varied in the range from 0 to 2 Torr while measuring the net current with a Rogowski coil. Results in terms of peak net current vs gas pressure for He, N_2, and Ar are shown in Fig. 3. Peak currents were generally several kiloamperes and in some shots currents as high as 10 kiloamperes were measured. The most reproducible results were obtained with argon. Using the lighter gases sometimes there were multiple pulses. Current traces from the Rogowski coil may not be a true representation of beam current since the beam may ionize filling gas and create plasma return currents which may reduce the height and increase the width of the pulse. However, these measurements do represent a qualitative comparison of operation with different gases and different pressures. The measurements described in the remainder of this report were all taken using argon gas with a pressure of 1 Torr.

A more accurate measurement of the beam current was achieved with the Faraday cup diagnostic shown in Fig. 4. The region downstream of the thin foil is evacuated so that only beam electrons with range greater than the foil thickness are collected by the carbon disk. The disk is connected to ground through a 50 mΩ current viewing resistor whose risetime is 0.2 ns. Measured current waveforms for beam electrons whose energy is greater than 20 keV (6 μm mylar foil), and greater than 50 keV (13 μm titanium foil), are given in Fig. 4.

Electron beam energy was measured with the magnetic spectrometer[15] shown in Fig. 5. The spectrometer case is made of soft ion with one side open for photographic measurements of electron deflections. The field strength is 0.53 Wb/m^2 and type P-31 phosphor was used as the detector. The plunger is opened only at the time of firing so that the spectrometer is operated in a vacuum environment. After measurement of electron deflection, electron energy, T in eV, is calculated according to

$$T = [E_0^2 + (\frac{c}{2} Bd)^2]^{1/2} - E_0 \quad (eV),$$

where $E_0 = m_0 c^2/e = 0.511 \times 10^6$ eV, B is the magnetic field strength in Wb/m^2, and d is the measured electron deflection in m. The spectrometer is capable of measurement in the range from 0.2 to 1.5 MeV. Open shutter photography with black and white 35 mm film was used to record deflections. The film was scanned with a microdensitometer to produce results such as shown in Fig. 5. The peak at the origin is due to plasma light showing through the collimating slit and the interruption at T = 120 keV is caused by a scratch in the phosphor used as a fiducial mark. While the spectrum peaks at 100 keV, electrons in the high energy tail are observed at energies near 300 keV.

An open shutter photograph of the beam propagating in a gas-filled drift tube is shown in Fig. 6. An acrylic tube with a copper screen lining was utilized for this photograph. The beam does not stably propagate, therefore it was necessary to position diagnostics near the location of beam injection for accurate measurements.

The beam parameters measured here (10-20 ns, 1-10 kA, 100-300 keV) are similar to results in other experiments using much larger devices.[10,11,13] Our results, while interesting for such a small device, will be more promising if the energy can be scaled upward to the MeV region in future work.

REFERENCES

1. M. J. Rhee, C. M. Luo, R. F. Schneider, and J. R. Smith, in Proceedings of the 3rd International Workshop on Plasma Focus Research, edited by H. Herold and H. J. Kaeppeler (University of Stuttgart, Stuttgart, F. R. Germany, 1983) pp. 47-50.

2. S. Denus, Ref. 1, pp. 11-16.

3. K. Hirano, K. Shimoda, T. Yamamota, M. Sato, K. Kobayashi, and H. Misaizu, Ref. 1, pp. 35-38.

4. M. Sadowski, S. Chyrczakowski, W. Komar, E. Rydygier, and J. Zebrowski, Ref. 1, pp. 39-42.

5. A. Mozer, M. Sadowski, H. Herold, and H. Schmidt, J. Appl. Phys. $\underline{53}$, 2959 (1982).

6. H. Krompholz, E. Grimm, F. Rühl, K. Schönbach, and G. Herziger, Phys. Lett. $\underline{76A}$, 255 (1980).

7. M. Yokoyama, Y. Kitagawa, Y. Yamada, M. Okada, Y. Yamamoto, T. Hori, and C. Yamanaka, in Conference Record - Abstracts 1982 IEEE International Conference on Plasma Science, IEEE Catalog No.: 82CH1770-7, 116 (1982).

8. R. L. Gullickson and H. L. Sahlin, J. Appl. Phys. $\underline{49}$, 1099 (1978).

9. V. Nardi, W. H. Bostick, J. Feugeas, W. Prior, and C. Cortese, Plasma Physics and Controlled Nuclear Fusion - Research 1978, (Proceedings of the 7th International Conference on Plasma Physics and Controlled Nuclear Fusion Research, Innsbruck, Austria, 1979), Vol. 2, pp. 143-157.

10. W. Stygar, G. Gerdin, F. Venneri, and J. Mandrekas, Nucl. Fusion $\underline{22}$, 1161 (1982).

11. W. L. Harries, J. H. Lee, and D. R. McFarland, Plasma Phys. $\underline{20}$, 95 (1978).

12. K. Schmitt, H. Krompholz, F. Rühl, and G. Herziger, Phys. Lett. $\underline{95A}$, 239 (1983).

13. R. L. Gullickson and R. H. Barlett, Adv. X-Ray Anal. $\underline{18}$, 184 (1975).

14. M. J. Rhee and R. F. Schneider, IEEE Trans. Nucl. Sci. $\underline{30}$, 3192 (1983).

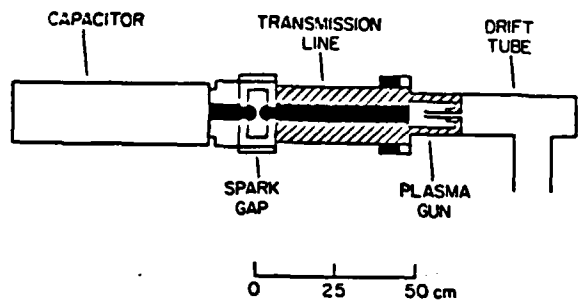15. R. F. Schneider, C. M. Luo, M. J. Rhee, and J. R. Smith, to be published.
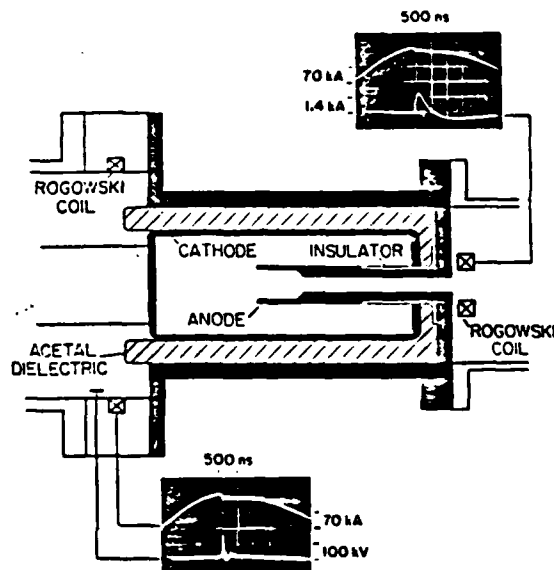
Fig. 1
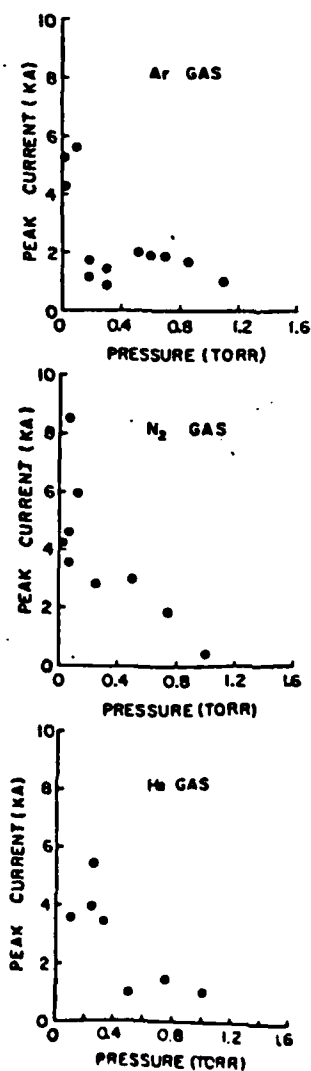The compact plasma focus.

Fig. 2   Modified plasma gun.

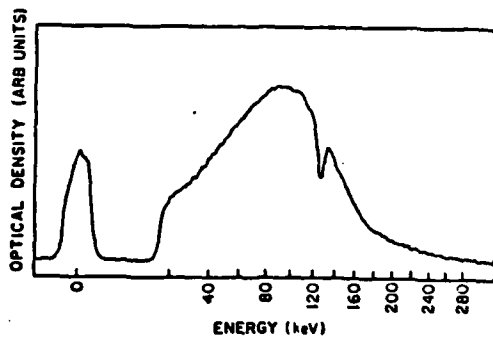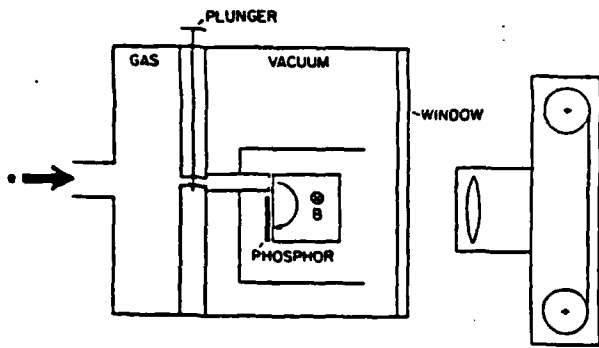Fig. 3   Peak Rogowski current vs.
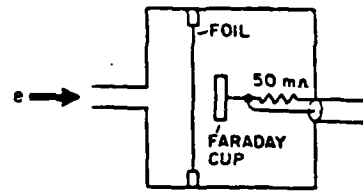gas pressure for He, N_2, and Ar.
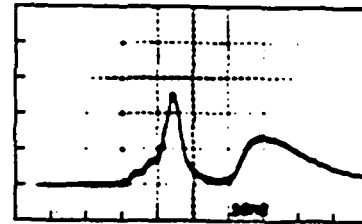
Fig. 4   Electron Faraday cup diagnostic
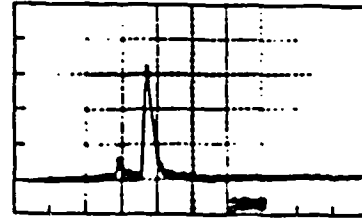
Fig. 5

Magnetic spectrometer
diagnostic and electron
spectrum.

Fig. 6

Open shutter photograph of the beam propagating
in the drift tube with 1 Torr of argon.

Compact Thomson spectrometer

M. J. Rhee

Electrical Engineering Department and Laboratory for Plasma and Fusion Energy Studies, University of Maryland, College Park, Maryland 20742

Particle dynamics and collimation in the Thomson spectrometer system are discussed. A compact spectrometer which consists of a unique pinhole arrangment, a pair of permanent magnets, and CR-39 detector is described with a few practical calibration techniques. Applications including analysis of charge-to-mass ratio and construction of charge state resolved energy spectra are discussed with experimental examples.

INTRODUCTION

In the past several years, there has been an increasing interest in the Thomson spectrometer as an ion diagnostic. Since the Thomson spectrometer provides information of energy, momentum, charge-to-mass ratio, etc., simultaneously, it has been used for study of ion sources such as collective ion accelerators,[1-5] laser produced plasmas,[6-11] ion diodes,[12,13] and plasma foci.[14-18] The Thomson spectrometer requires a high-sensitivity detector to record the very-low-intensity beams resulting from the high degree of beam collimation required to provide adequate resolution.

The high gain (10^3) chaneltron electron multiplier array (CEMA) has been used successfully by Kuswa *et al.*[1] and others[6,8,9,13] as a low-intensity particle detector in the Thomson spectrometer. Recently, solid nuclear track detectors have been widely used for ion detection.[19] In particular, CR-39 plastic appears to be the most sensitive material for track detection[20] and is well suited to the Thomson spectrometer. Numerous applications of CR-39 in this type of spectrometer have been reported.[4,5,12,14,16,18]

It is the purpose of this paper to describe a compact spectrometer system which has been found to be both very practical and optimized with regard to the resolution of the system. In the following sections, the general principles are reviewed and the required collimation, relating to the spectrometer resolution, is discussed. Subsequently, the design of the actual device is described with a few calibration techniques. In the final section, the analysis of the charge-to-mass ratio of ions and also the construction of energy spectra from the Thomson spectrogram are described.

I. PARTICLE DYNAMICS AND PARABOLA ANALYSIS

The analysis of ion trajectories in the Thomson spectrometer is well described in the literature.[21] In this section, we summarize and discuss the general features of the results. The deflection sector of the Thomson spectrometer consists of parallel electric and magnetic fields. For simple analysis, we begin with an assumption that both fields are uniform over length L and zero outside. It is elementary to show that the trajectory of nonrelativistic ions moving perpendicular to the electric field is parabolic and the resulting total deflection angle gained in the entire field region is found to be approximately

$$\theta_e = \frac{ZeEL}{Am}\frac{1}{v^2} = \frac{ZeEL}{2T},\tag{1}$$

where θ_e is the electric deflection angle in radians (which is $\tan\theta_e$ for a large angle), Z is the charge state of the ion, e is the electronic charge, EL is the product of electric field and the length of the field, A is the ion mass number, m is the unit nucleon mass based on C^{12}, v is the velocity, and T is the kinetic energy of the ion. The mks units are used throughout. Similarly, the trajectory of ions moving perpendicular to the magnetic field is circular; thus the magnetic deflection angle is approximately given by

$$\theta_b = \frac{ZeBL}{Amv} = \frac{ZeBL}{\sqrt{2AmT}},\tag{2}$$

where the term BL is the product of the magnetic field and its length. If one replaces L with the arc length of the trajectory, then Eq. (2) would be exact. One can show that the intersection of extensions of incident and deflected trajectories occurs exactly at the center of the electric field. This is also true for a magnetic field of circular cross section but, in general, does not hold true for other shapes (see Fig. 1).

Since the electric and magnetic fields are parallel, the corresponding deflections given by Eqs. (1) and (2) are orthogonal to each other. The information one can obtain from the two-dimensional deflection may be expressed in the functional form

$$\alpha_i = f_i(\theta_e,\theta_b),\tag{3}$$

where α_i is a physical quantity associated with the ions and f_i is a function of coordinates θ_e and θ_b only. Many functions f_i, that describe lines in the $\theta_e - \theta_b$ plane, may be possible for corresponding quantities α_i. A few directly meaningful quantities associated with the ions are immediately derived from Eqs. (1) and (2). The momentum per charge can be found from Eq. (2) as
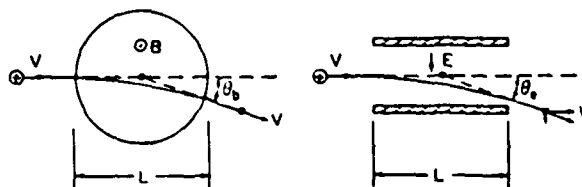

FIG. 1. Particle deflections in an idealized field system for the Thomson spectrometer.

$$Amv/Ze = BL/\theta_b , \qquad (4)$$

which is inversely proportional to the magnetic deflection and independent of the electric deflection. Any horizontal line $\theta_b =$ const corresponds to a constant momentum per charge. Similarly, the kinetic energy per charge is found from Eq. (1) as

$$\frac{1}{2}\frac{Amv^2}{Ze} = \frac{1}{2}\frac{EL}{\theta_e} , \qquad (5)$$

which depends only on the electric deflection. Any ions on a vertical line $\theta_e =$ const have a constant energy per charge.

The velocity of ions is found by taking the ratio of Eqs. (1) and (2) as

$$v = \frac{EL}{BL}\frac{\theta_b}{\theta_e} , \qquad (6)$$

which is independent of charge or mass. Any straight line crossing the origin of the deflection coordinates is a constant velocity line. Finally, the charge-to-mass ratio of ions is found by eliminating v in Eqs. (1) and (2) as

$$\frac{Ze}{Am} = \frac{EL}{(BL)^2}\frac{\theta_b^2}{\theta_e} . \qquad (7)$$

Thus, ions of various energies with the same charge-to-mass ratio form a well-known parabola shaped deflection pattern. Note that the quantities α_i of Eqs. (4)–(7) are of different moment of velocity. It is possible that one can construct additional functions for the quantities with higher moment of velocity such as $\frac{1}{2}(Z/A)mv^3$ and so on.

It is also interesting to find the points where the family of lines given by Eqs. (4)–(6) intersect each other. In Fig. 2, the intersections with a set of parabolas of C^{12} ions and three straight lines: (a) a constant momentum per charge, (b) a constant energy per charge, and (c) a constant velocity, are illustrated with the proton parabola as a reference. As can be seen in Eq. (7) with $\theta_e =$ const for constant energy per charge, or $\theta_b/\theta_e =$ const for constant velocity, the charge-to-mass ratios of intersections are proportional to θ_b^2 or θ_b, respectively. Thus, if there is a reference parabola of known charge-to-mass ratio, the charge-to-mass ratio of unknown parabolas can be found by either $(Z/A)/(Z/A)_{ref} = (\theta_b/\theta_{b\,ref})^2$ where θ_b and $\theta_{b\,ref}$ are of intersections with a line of constant θ_e or $(Z/A)/(Z/A)_{ref} = \theta_b/\theta_{b\,ref} = \theta_e/\theta_{e\,ref}$, where the deflections are of intersections with a line of constant θ_b/θ_e.

The Thomson spectrometer provides the charge-to-mass ratio Z/A of a given parabola, but does not indicate the charge Z or mass A of the parabola separately. If one can assume that parabolas of an ion species of every charge state below that of the unknown exist and extend to a constant velocity line, one can find the charge state of the unknown parabola by simply counting the number of intersections along the constant velocity line from the origin to the parabola. The ion species (mass) can also be identified with known charge and charge-to-mass ratio. The assumption made here appears to be true for many actual cases in which the ion deflection patterns of distinct shape are lined up with equal distance along a constant velocity line. The analysis of the intersections with a constant velocity line is more useful than that with constant energy per charge line, particularly
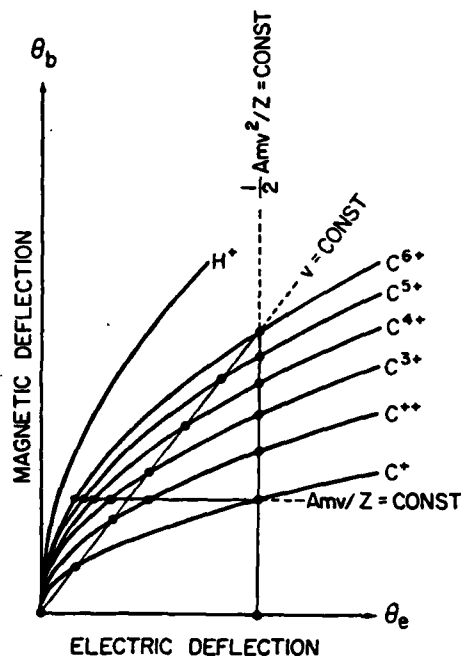

FIG. 2. Thomson parabolas of C^{12} ions and their intersections with a constant velocity line, a constant energy per charge line, and a constant momentum per charge line. The H^+ parabola is shown as reference.

when more than one ion species is present in a spectrogram. The intersections along the line of constant θ_e are unfolded into many different constant velocity lines with constant spacings between intersections.

A spectrogram, shown in Fig. 3(a), obtained in an earlier experiment[16] shows the distinct feature that all of the parabolas begin with a line of constant θ_e, i.e., the peak energy per charge of each parabola is constant. Another interesting pattern of parabolas observed frequently is that particles (tracks) of different parabolas are lined up on a constant velocity line as described in Eq. (6). The spectrogram, shown in Fig. 3(b) as a typical example, shows a constant peak velocity of different ions of different parabolas. Measurement of slope of the line and ratio of calibrated EL to BL are needed for actual velocity calculation.

II. COLLIMATION

CR-39, a commercially available clear plastic, is known as a nuclear track detector of very high sensitivity. It can
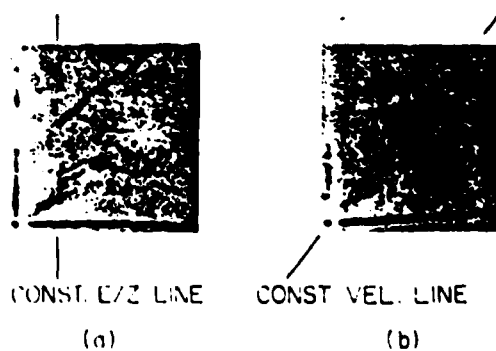

FIG. 3. (a) Parabolas of constant peak energy per charge. (b) Parabolas of constant peak velocity.

detect protons with energies up to 1 MeV and a wide range of other heavier ions.[20] Its uniformity of response and good optical quality make it ideal for use as a Thomson spectrometer detector. The ultimate spatial resolution of the detector may be limited by the diameter of an etched track pit, a quantity that can be varied by the amount of etching, ion species, and its energy. The typical track size, about 1 μm, is convenient for optical microscope observation and is far below the practical size of the collimated beam (pinhole size). Therefore, the spatial resolution of the system depends mainly on the collimation of the beam. There is, however, a lower limit of collimation beyond which the beam intensity (track density on the detector) is reduced to levels too low to be analyzed.

Assuming a simple type of beam source, a quantitative analysis of size and intensity of the beam can be given as below. In general, two pinholes are required to collimate the beam as shown in Fig. 4. We assume that the beam distribution at the first pinhole is as if particles are emitted from isotropic point sources which are evenly distributed on the entire pinhole area. To a good approximation, the above assumption may be practical if the pinhole is placed downstream of a relatively large source which emits particles isotropically within a small solid angle.

From the geometry (see Fig. 4), the size of the beam at the detector plane is found as

$$D_3 = D_2\left(1 + \frac{L_2}{L_1}\right) + D_1\frac{L_2}{L_1},\tag{8}$$

$$D_3' = D_2\left(1 + \frac{L_2}{L_1}\right) - D_1\frac{L_2}{L_1},\tag{9}$$

where D_1 and D_2 are diameters of the first and second pinholes, respectively, and L_1 and L_2 are distances between the two pinholes, and the second pinhole and detector, respectively. D_3 is the diameter of the beam at the detector plane and D_3' is a diameter of the peak intensity spot. The intensity within D_3' is nearly constant, and easily found as

$$n_3' = \frac{n_1 D_1^2}{16(L_1 + L_2)^2},\tag{10}$$

where n_1 is the source intensity at the first pinhole. This intensity is independent of D_2 provided that D_3' is larger than zero or

$$D_2 > \frac{L_2}{L_1 + L_2}D_1.\tag{11}$$

As shown in Fig. 4, the angle θ_c that defines a conical beam envelope after the second pinhole is found from the geometrical relationship as $\theta_c = (D_1 + D_2)/L_1$. It is clear from Fig. 4 that if the deflection angle difference of any two beams of different quantities is less than the angle θ_c, the images of the two beams cannot be separated at the detector plane regardless of its position. Thus, the angle θ_c is referred to as the "collimation resolution angle." It is a serious drawback of the Thomson spectrometer system that the resolution of the system depends only on the collimation, since no focusing principle can be adopted.

There is, in general, a trade off between the beam size and the beam intensity as seen in Eqs. (8) and (10). However, a satisfactory condition, which provides both beam size and intensity, exists. Having a small ratio L_2/L_1, small second pinhole size D_2, and fairly large first pinhole size D_1, the size of the beam D_3 at the detector is nearly proportional to D_2, and n_3' is proportional to the square of D_1 as in Eqs. (8) and (10), respectively. In this regime, the beam size D_3 is adjusted by the second pinhole size D_2, and the intensity n_3' is adjusted by the first pinhole size D_1 almost independently of D_2.

In a typical Thomson spectrometer, the two pinholes are placed upstream of the deflection sector and the detector is placed downstream. This arrangement has been employed in almost every Thomson spectrometer system since Thomson's original system.[22] In such a system, the minimum distance L_2 is limited by the length of the deflection sector. This large L_2 not only makes D_3 large, but also reduces the intensity n_3'. To remedy this, the deflection sector in our spectrometer is placed between the first and second pinholes so that the distance L_2 can be adjusted to any small value. It is worth mentioning that the particle trajectory in this system is somewhat different from that in the conventional system. One can consider the first pinhole located far upstream of the spectrometer to be approximately a point source. Thus, a nearly uniform and parallel beam enters the entire space of the field region. Only the neutrals (or extremely energetic ions) among the on-axis particles, which are not deflected by the fields, can pass through the second pinhole marking the origin of deflection coordinates on the detector. All other on-axis ions are deflected by the fields and checked by the pinhole plate. Those ions that can pass through the pinhole after deflection are off-axis particles whose initial position can offset the deflection. One can show that the angles of these particles as they pass through the pinhole are the combination of two deflection angles given by Eqs. (1) and (2) as in the conventional system. There exists a maximum electric deflection angle due to the finite electrode gap (pole gap), and this acceptance angle is found in deflection geometry (see Fig. 1) to be equal to the aspect ratio of electrode; gap/radius. This angle, which limits the lower bound of ion energy range, would be chosen appropriately for the application of the spectrometer as mentioned in the next section. It should be noted that this limitation is exactly the same as that in the conventional system. Some advantages are found for this system. For the spectrogram analysis, the deflection angle is obtained directly from the distance between the second pin-
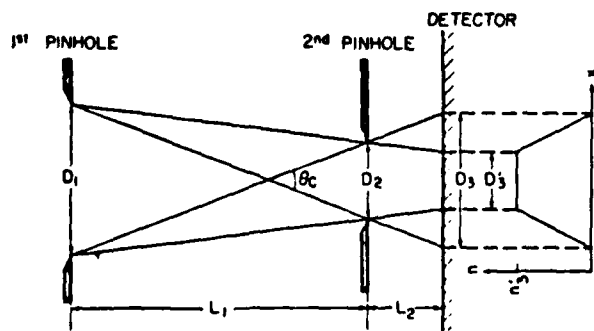

FIG. 4. Geometrical relationships between pinholes, detector, and density profile.

hole and detector and the deflection on the detector, whereas for the other system, the deflection angle is deduced from the deflection and a distance between the detector and the center(s) of field regions, which may not be exactly defined, particularly when the field is nonuniform or asymmetric. Another advantage of this system over the usual arrangement is in the small size of the resultant spectrogram due to the short distance between the pinhole and the detector. This feature permits us to make multiple exposures on a detector plate of reasonable size using an advancing mechanism as described in the next section, or to make several simultaneous spectrograms of beams sampled at different positions. It should be mentioned that the use of small samples (typically 1×1 mm) is of great convenience, since they can be photographed easily using either an optical microscope or an electron microscope.

III. DESIGN CONSIDERATIONS

In an early design reported by us[16] and others,[4,5] a permanent magnet is placed outside the vacuum chamber so that the magnetic field can be easily turned off by removing the magnet away from the system without disturbing the experimental conditions. This arrangement enables us to add the reference axes to the parabola spectrogram by having two reference exposure shots. This technique has been found to be extremely convenient in data analysis as it minimizes possible systematic errors.

After some experience with this spectrometer, we have discovered that it always shows a clear spot corresponding to the origin of the system axis. Examination of the spot by a scanning electron microscope has revealed that it is made of a mixture of different particle tracks which can be found in the various parabolas in the same spectrogram, leading to the conclusion that neutrals are responsible for the spot. The existence of such neutrals not only eliminates the extra reference shot but also permits us to use small magnets built into the system. This feature makes the overall system even more compact and simplifies operation of the system.
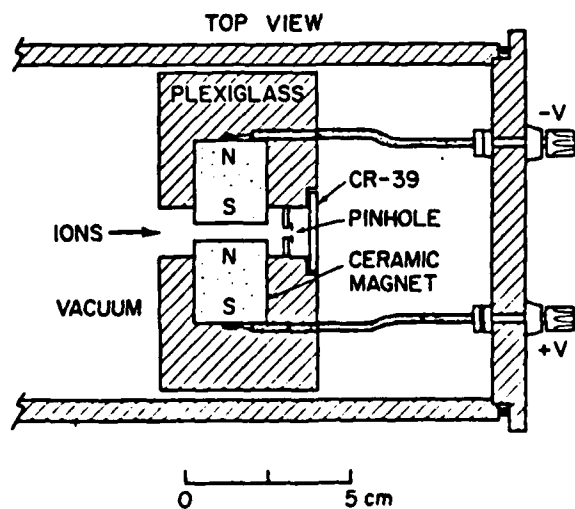

TOP VIEW

FIG. 5. Cross-sectional view of a compact spectrometer.

In this section, a very compact spectrometer, which has been briefly reported,[18] incorporating the above-mentioned features in addition to those in the previous designs[16] is described. Two round bar ceramic magnets of 2.22 cm (7/8 in.) diameter and 2.54 cm (1 in.) long are clamped by two acrylic disks maintaining a certain pole gap as shown in Fig. 5. The magnets are also separately connected to a high-voltage power supply to produce an electric field parallel to the magnetic field in the gap. The smaller the gap, the higher the magnetic and electric fields that can be produced with given magnets and bias voltage. Reducing the gap also reduces the aspect ratio of the pole gap and radius which is equal to the maximum acceptance angle in the direction of the E axis. In this device, the gap is chosen to be 3 mm which gives a maximum acceptance angle of $3/(22.2/2) = 0.27$ rad.

A second pinhole is placed immediately downstream of the pole pieces for reasons described in the preceding section. The pinhole system is so arranged that various sized pinholes can be easily interchanged. The smallest sized pinhole used consists of a 10-μm-diam hole drilled on 10-μm-thick nickel foil. The CR-39 detector is mounted on a slot 5 mm (L_2) downstream of the pinhole. A simple lever with a shaft, which can be cranked from the outside of the vacuum chamber, is used to advance the detector plate without breaking the vacuum. This simple mechanism enables us to make multiple exposures (easily up to ten exposures) on one detector plate. This feature makes the spectrometer system convenient enough to be used as a beam monitor of shot to shot variations.

IV. CALIBRATIONS

The deflection of ions as calculated in Eqs. (1) and (2) is proportional to the fields and their lengths. Accordingly, other quantities obtainable from the spectrogram are subject to the accuracy of the fields and their length as in Eqs. (4)–(7). The ideal field geometries expressed as EL or BL, which were assumed for the simple analysis, are not only unrealizable physically but violate Maxwell's equations. It can be shown that if the deflection angles are small, the terms EL and BL can be replaced by $\int E\, dl$ and $\int B\, dl$, respectively, in the relevant equations if the real field distributions E and B are known.

The magnetic field distribution is measured along the system axis by using a Hall probe system. The accuracy of the system is within 1.5% and the Hall probe active area is of 1.8 mm diameter, which is a measure of the spatial resolution of the probe. The probe is coupled to an X-Y recorder to obtain a continuous distribution. The measured field distribution is numerically integrated and found to be

$$\int B\, dl = (5.97 \pm 0.09) \times 10^{-3} \text{ Tm.}$$

Since the electric field, unlike the magnetic field, is quite difficult to measure, a numerical calculation of the field has been carried out by solving the Laplace equation with appropriate boundary conditions. The axisymmetric cylindrical coordinate system is used in the computation because of the electrode (magnet polepiece) geometry. However, the outer boundary, which can not be well described in such a
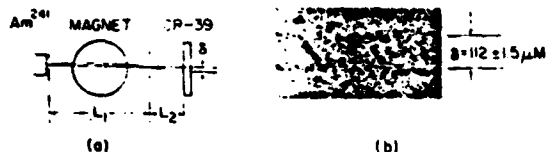
FIG. 6. (a) α-particle calibration system. (b) Optical microscope photograph of etched CR-39 detector showing deflected and undeflected α-particle tracks.

system, is replaced by a simple cylindrical wall of finite radius with either Dirichlet or Neumann boundary conditions. The resulting electric field distribution is integrated along the axis (beam path) and found to be

$$\int E\,dl/E_0 L_0 = 1.26 \pm 0.05 \tag{12}$$

for the given aspect ratio of electrodes $d/(D/2) = 3/11.11$ mm, where the $E_0 L_0$ is the product of the electric field of the ideal parallel plate capacitor V_0/d and its diameter D. The error in Eq. (12) represents the difference between the two results obtained using Dirichlet and Neumann conditions for the outer boundary.

Another calibration method used by Smith[5] is the direct measurement of α-particle deflection in the spectrometer system. The easily available α-source Am^{241} emits α particles of 5.485 and 5.443 MeV. A slit collimation system, as shown in Fig. 6(a), similar to the pinhole system in the spectrometer described in Sec. II, is employed; the first slit of 100 μm that is attached to an α source to form a line source and the second slit of 12 μm placed in front of the CR-39 detector, are placed upstream and downstream of the pole pieces, respectively, thus making the corresponding distances in Eq. (8) of $L_1 = 5$ cm and $L_2 = 1.0$ cm. To produce a sufficient number of tracks, two exposures are made to a CR-39 detector of three days duration with and without the magnet system with a 1-μC source. Then the detector is etched 4 h in an NaOH solution at 70 °C. A portion of the resulting optical microscope photograph is shown in Fig. 6(b). The coordi-
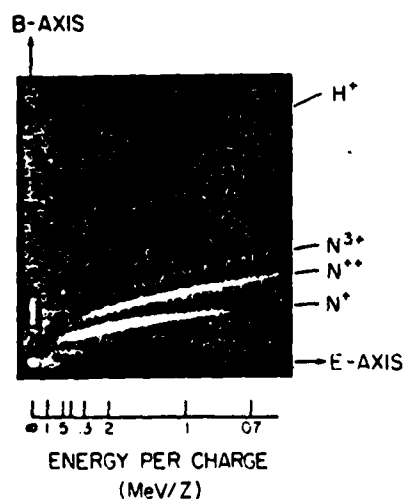
nates of all the tracks are measured and are statistically analyzed. The separation distance between the lines is found to be 112 ± 1.5 μm in which the statistical standard error corresponds to 1.3%. From this, the term BL in the equations is deduced by a geometrical relation as

$$BL = (6.06 \pm 0.08) \times 10^{-3}\,\text{Tm}. \tag{13}$$

This value agrees with the integrated field distribution $\int B\,dl$ within an error of 1.5%.

Similar calibrations can be done for the electric deflection.[5] In this case, however, knowing the charge-to-mass ratio Z/A of a known ion species and the calibrated value of BL in Eq. (13), the term El has been found by use of the deflections θ_e and θ_b which can be measured in a Thomson parabola. The proton parabola is the most convenient for this purpose, since it is easily identifiable because of its larger separation from the other parabolas (as can be seen in Fig. 7) and also has the smallest track size due to the fact that protons have the least energy loss. Taking deflection measurements from several points on the parabola with the value in Eq. (13), we obtain

$$EL/E_0 L_0 = 1.254 \tag{14}$$

in good agreement with the results of the computational analysis and well within an error of 1%. Thus, all the calibrations using different methods are consistent with each other, suggesting that only one calibration (whichever is convenient) is necessary for the purpose of parabola analysis.

V. PARABOLA ANALYSIS AND ENERGY SPECTRUM

In this section, analysis of an ion beam produced by a plasma focus device[18] is described as an example of the application of the spectrometer. The device used here consists of a coaxial plasma gun and a 3-kJ capacitor which are coupled through a coaxial transmission line. Ions, predominantly of the filling gas element, are accelerated in the forward axial direction.

The first pinhole of the spectrometer system, whose aperture size can be varied up to 1.5 mm diameter, is placed 50 cm upstream of the spectrometer ($L_1 = 50$ cm). For the highest resolution, the smallest available pinhole (10 μm diameter) is used for the second pinhole which is placed immediately after the field region and 5 mm upstream of the CR-39 detector ($L_2 = 0.5$ cm). A spectrogram obtained for the nitrogen filling gas is shown in Fig. 7. The B axis, obtained by a reference shot without the electric field, and the neutral spot which together conveniently define the coordinate system are also shown. Proton tracks of very low density exist as an impurity and are sufficient to be used as the reference.

The charge-to-mass ratio of unknown parabolas may be determined by Eq. (7) with the measured coordinates (deflection angles) of points along the parabola and the calibrated values of EL and BL. Another method which is convenient and accurate, is to compare the unknown parabola with that of reference ions such as protons as described in Sec. I. This method does not even require calibration. The accuracy depends only on the measured ratio of deflections. The charge-to-mass ratios of parabolas are found as $Z/A = (\theta_b/\theta_{bp})^2$ by measuring the ratio of magnetic deflection of unknown ions θ_b to that of protons θ_{bp} at the same electric deflection

FIG. 7. Thomson parabolas of N^{14} and H^+ ions, reference axis, and origin spot of neutrals.
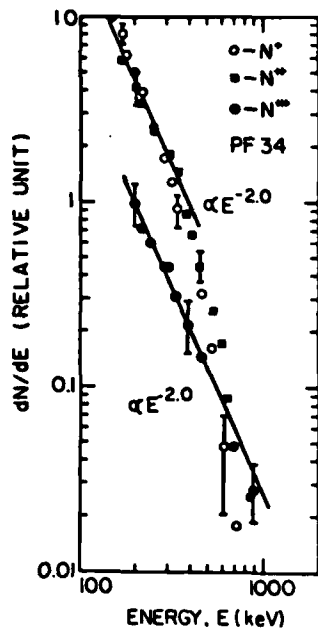
ENERGY PER CHARGE

(MeV/Z)

FIG. 8. Charge state resolved energy spectra of N^{14} ions constructed from the parabolas shown in Fig. 7.

$\theta_e = \theta_{ep} =$ const. The charge-to-mass ratio obtained using the proton parabola as the reference is very close to that of N^+, N^{++}, and N^{3+} within an error of less than 1%.

As an added feature of the spectrometer, the construction of charge state resolved energy spectra is possible due to the smaller size of the spectrogram, the thin linewidth of the parabola, and the adjustability of the track density of the parabola. As described earlier, the first pinhole aperture is reduced to 100 μm diameter to produce a track density of parabolas low enough to be separated for counting by using an optical microscope. To construct time integrated, charge state resolved energy spectra of ions, the parabolas are divided into many small segments $\Delta\theta_i$, of constant electric deflection angle. The number of tracks N_i in the ith segment of each parabola of N^+, N^{++}, and N^{3+} are counted separately. The mean energies E_i and energy increment ΔE_i in kiloelectron volts in the ith segment of each parabola are calculated to find the energy spectra from

$$\frac{dN}{dE} = \frac{\Delta N_i}{\Delta\theta} \frac{\Delta\theta_i}{\Delta E_i}, \tag{15}$$

and each spectrum is plotted in Fig. 8.

[1]G. W. Kuswa, L. P. Bradley, and G. Yonas, IEEE Trans. Nucl. Sci. NS-20, 305 (1973).

[2]R. F. Hoeberling, R. B. Miller, D. C. Straw, and D. N. Payton III, IEEE Trans. Nucl. Sci. NS-24, 1662 (1977).

[3]S. Takeda, M. Tamura, T. Yamamoto, and M. Kowanishi, Jpn. J. Appl. Phys. 18, 641 (1979).

[4]W. W. Destler and J. T. Cremer, J. Appl. Phys. 54, 636 (1983).

[5]J. R. Smith, Ph.D. thesis, North Carolina State University, 1983.

[6]J. N. Olsen, G. W. Kuswa, and E. D. Jones, J. Appl. Phys. 44, 2275 (1973).

[7]D. C. Slater, Rev. Sci. Instrum. 49, 1493 (1978).

[8]G. L. Payne, J. D. Perez, T. E. Sharp, and B. A. Watson, J. Appl. Phys. 49, 4688 (1978).

[9]M. A. Gusinow, J. P. Anthes, M. K. Matzen, and D. Woodall, Appl. Phys. Lett. 33, 800 (1978).

[10]J. P. Anthes, M. A. Gusinow, and M. K. Matzen, Phys. Rev. Lett. 41, 1300 (1978).

[11]M. A. Yates, J. Kephart, R. Robertson, F. Begay, T. H. Tan, A. W. Ehler, A. H. Williams, S. K. Wilson, D. Van Hulsteyn, R. F. Benjamin, S. Pederson, J. Hayden, and C. Barnes, Bull. Am. Phys. Soc. 26, 934 (1981).

[12]T. Ozaki, S. Miyamoto, F. Ogawa, A. Yoshinouchi, K. Imasaki, S. Nakai, and C. Yamanaka, J. Appl. Phys. 54, 632 (1983).

[13]T. D. Stanley and R. W. Stinnet, Proceedings of the Workshop on the Measurement of Electrical Quantities in Pulse Powser Systems, 2–4 March 1981 (U. S. GPO, Washington, D.C., 1981), NBS Special Publication 628, p. 87.

[14]M. J. Rhee, Bull. Am. Phys. Soc. 25, 958 (1980).

[15]H. Herold, A. Mozer, M. Sadowski, and H. Schmidt, Rev. Sci. Instrum. 52, 24 (1981).

[16]M. J. Rhee, IEEE Trans. Nucl. Sci. NS-28, 2663 (1981).

[17]A. Mozer, M. Sadowski, H. Herold, and H. Schmidt, J. Appl. Phys. 53, 2959 (1982).

[18]M. J. Rhee and R. F. Schneider, IEEE Trans. Nucl. Sci. NS-30, 3192 (1983).

[19]R. L. Fleischer, P. B. Price, and R. M. Walker, Nuclear Tracks in Solids (University of California, Berkeley, CA, 1975).

[20]B. G. Cartwright, E. K. Shirk, and P. B. Price, Nucl. Instrum. Methods 153, 457 (1978).

[21]See, e.g., J. Roboz, Introduction to Mass Spectroscopy (Wiley, New York, 1968).

[22]J. J. Thomson, The Corpuscular Theory of Matter (Archibald Constable and Co., London, 1907).

RESOLUTION ANALYSIS OF THE THOMSON SPECTROMETER

R. F. Schneider, C. M. Luo, and M. J. Rhee

Laboratory for Plasma and Fusion Energy Studies
University of Maryland
College Park, Maryland 20742

Abstract

The resolution of Thomson spectrometers is examined. Charge, mass, energy, and momentum resolutions are found as functions of collimation parameters and field strengths. The results are generally applicable to all Thomson spectrometer systems. In conjunction with this analysis, a compact Thomson spectrometer with high resolving power is described.

I. Introduction

Thomson spectrometers have recently been widely used for the analysis of ion beams produced in collective ion acceleration[1-6] and plasma focus[7-11] experiments. They are found extremely useful for the investigation of ion sources in any device that produces a beam of sufficient intensity or duration compatible with the large degree of collimation necessary for this device. Recently we reported[12] the construction of a Thomson spectrometer which utilizes the highly sensitive nuclear track plate known as CR-39 as a detector and a small permanent magnet. The use of this highly sensitive detector allows a high degree of collimation of the beam in order to produce a compact Thomson spectrometer with high resolving power. The methods by which ion species and energy spectra are obtained from the raw data on the detector are discussed in Ref. 12. In this paper, we will analyze the factors which affect the resolution of the Thomson spectrometer and apply them to the newly constructed compact Thomson spectrometer which has much higher resolving power.

II. Detector Image Geometry

The compact Thomson spectrometer geometry which employs the second collimating pinhole downstream of the field region leads to a simplification in the treatment of the Thomson spectrogram. In the following, we employ a small angle approximation by setting $\tan\theta$ equal to θ. This introduces an error on the order of 1.5% for deflection angles of 200 milliradians (mrad) or less. This approximation

introduces much less error than other factors which we shall consider, and is in fact commonly used in Thomson spectrometer analysis. The magnetic and electric deflections on the detector, x_m and x_e, are proportional to the magnetic and electric deflection angles, θ_m and θ_e, by

$$\theta_i = \frac{x_i}{L} \tag{1}$$

where L is the distance from the downstream (second) pinhole to the detector in the compact spectrometer (L_2 in Fig. 1). This analysis may also be applied to conventional Thomson spectrometers which utilize both collimating pinholes upstream of the field region. It is necessary in this case to define L as the distance from the detector to the point where incident and final particle trajectories intersect. Usually, this is taken to be the center of the field region. The magnetic and electric deflection angles, θ_m and θ_e, are given by the simple non-relativistic expressions:

$$\theta_m = \frac{Ze \int Bd\ell}{p} \tag{2}$$

$$\theta_e = \frac{Ze \int Ed\ell}{2T} \tag{3}$$

where Ze is the product of ion charge state and electronic charge, $\int Bd\ell$ and $\int Ed\ell$ are the integrals of the magnetic and electric fields along the ion path length, and T and p are the ion energy and momentum
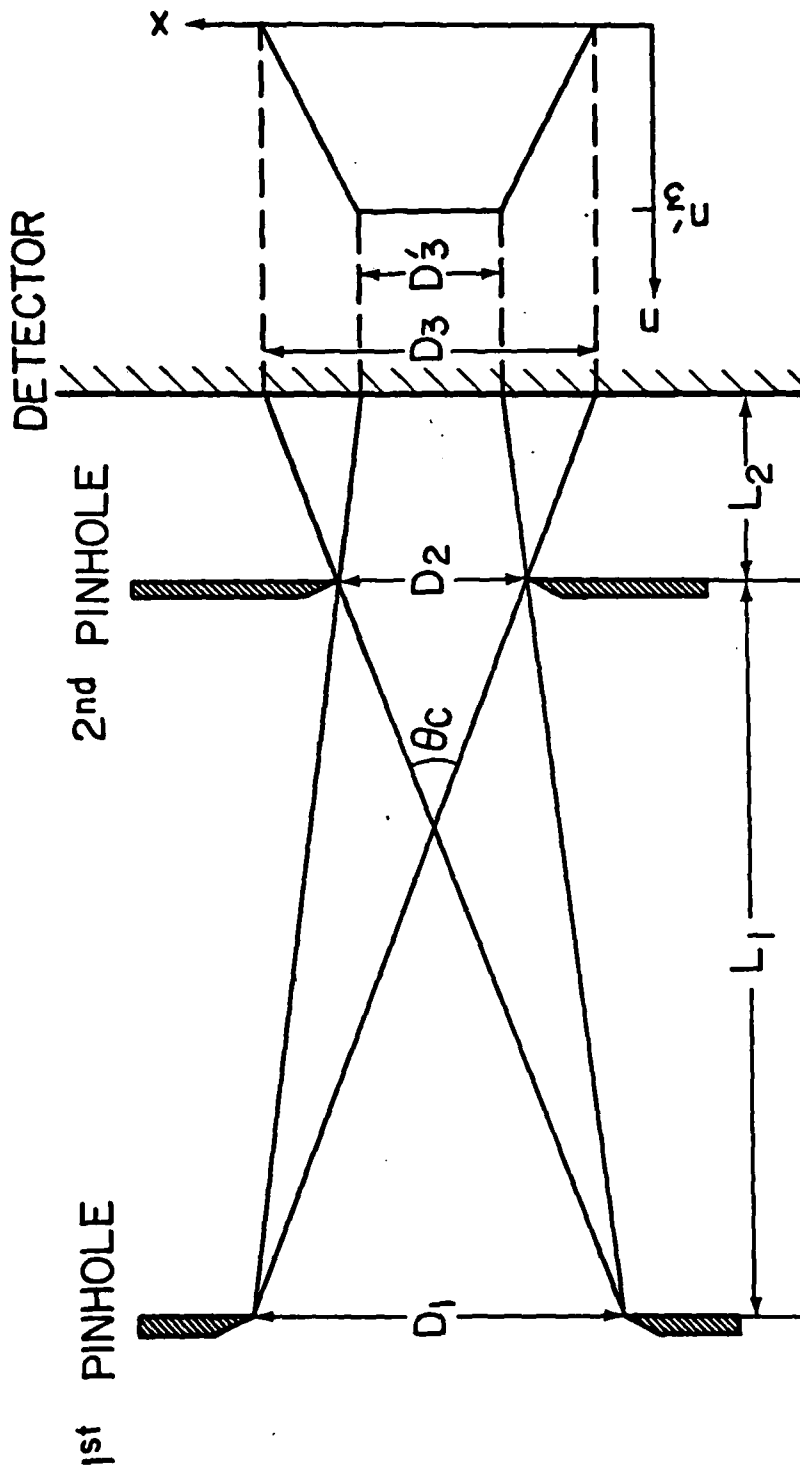
Fig. 1 Detector image geometry showing density profile and spot sizes given by Eqs. (5) and (19).

respectively. MKS units are used throughout. By elimination of p and T, Eqs. (2) and (3) combine to give the well known parabola equation:

$$\theta_m^2 = \frac{Z}{A} \left[\frac{e}{u} \frac{(\int Bd\ell)^2}{(\int Ed\ell)} \right] \theta_e \quad , \tag{4}$$

where A is the atomic mass number of the ion, and u is the unit mass of a nucleon, 1.66×10^{-27} kg.

A major purpose of the Thomson spectrometer is to separate parabolas of different charge to mass ratio in order to differentiate ion species and charge state. This in principle happens naturally if the parabola is an infinitely thin line. Practically, however, this can never be done since the collimation procedure utilizes two pinholes which produce an image with a finite diameter as displayed in Fig. 1. The resulting width of the parabolas, which are swept out by the different energies of a given charge to mass ratio, leads to overlapping, which reduces the resolution of the spectrometer. From the geometry of Fig. 1, the width of the parabola on the detector is given by

$$D_3 = \frac{L_2}{L_1} (D_1 + D_2) + D_2 \quad . \tag{5}$$

This corresponds to a subtended angle of

$$\delta = \frac{D_3}{L} \quad . \tag{6}$$

As in Eq. (1), L here is different for conventional and compact
spectrometers. The overlapping of the parabolas as they near the origin
can be calculated and resolution criterion can be obtained by
determining the points where different charge to mass ratio parabolas
are separated for either constant charge or constant mass. It is
interesting to note that these equations arise solely from the pinhole
geometry and are independent of the location of the field region, hence
this analysis is completely general. The only difference between
compact and conventional spectrometers is the position of the pinholes
relative to the fields. In the compact spectrometer, the field region
is placed between the first and second pinholes allowing much more
control over the diameter of the pinhole collimation image on the
detector. In conventional spectrometers, the pinhole collimation system
is entirely upstream of the fields. This implies that the distance L_2
in Fig. 1 must be large enough to contain the fields. This limits the
minimum obtainable D_3, and hence requires a spectrometer which is an
order of magnitude larger to obtain the same resolution.

III. Charge and Mass Resolution Analysis

To analyze charge resolution, we suppose we have one ion species
with several different charge states. Along what curve can we find the
points at which neighboring parabolas are separated? To answer, we use
the criterion for separation that $\Delta\theta_m$, the separation of the centers of
the parabolas along a vertical line, i.e. θ_m direction, must be greater
than the parabola width along that line,

$$\Delta\theta_m > \delta \left[1 + \frac{\theta_m^2}{4\theta_e^2}\right]^{1/2} \quad \text{and} \quad \Delta\theta_e = 0 \quad . \tag{7}$$

This is illustrated in Fig. 2. Here we have made use of the fact that the slope of the parabola is given by

$$\frac{d\theta_m}{d\theta_e} = \frac{\theta_m}{2\theta_e} \quad , \tag{8}$$

which is derived from the parabola Eq. (4). Assuming small $\Delta\theta_m$, we can substitute the separation condition Eq. (7) into the total differential of the parabola Eq. (4) with Z, A, θ_e, and θ_m as variables yielding:

$$\frac{dZ}{A} - Z\frac{dA}{A^2} = \frac{u}{e} \frac{\int Ed\ell}{(\int Bd\ell)^2} \frac{2\theta_m}{\theta_e} \delta \left[1 + \left(\frac{\theta_m}{2\theta_e}\right)^2\right]^{1/2} \quad . \tag{9}$$

If dA = 0 and dZ = 1, we will arrive at the equation describing the line connecting the points of charge resolution for a certain ion species:

$$\theta_m^4 + \theta_m^2 (4\theta_e^2) - \left(\frac{k}{A\delta}\right)^2 \theta_e^4 = 0 \quad . \tag{10}$$

We have made the definition

$$k = \frac{e}{u} \frac{(\int Bd\ell)^2}{\int Ed\ell} \quad . \tag{11}$$

The physical solution to the quartic equation is:

$$\theta_m = \left\{\left[4 + \left(\frac{k}{A\delta}\right)^2\right]^{1/2} - 2\right\}^{1/2} \theta_e \tag{12}$$
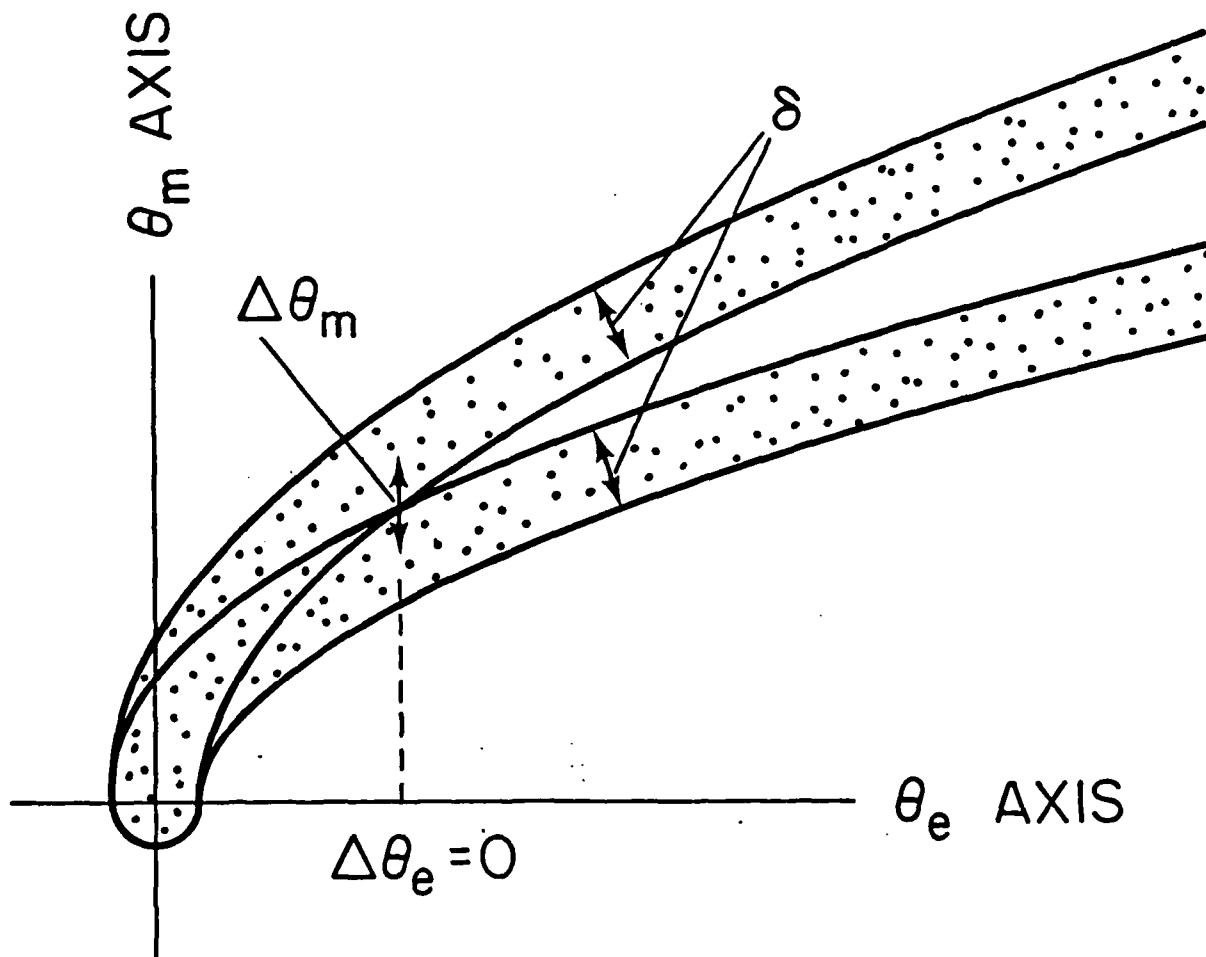
Fig. 2 Simulated Thomson spectrogram showing geometry of parabola separation with finite parabola width. The condition for separation of the parabolas is given by Eq. (7).

which describes a straight line which intersects the origin with slope $\{[4 + (k/A\delta)^2]^{1/2} - 2\}^{1/2}$. This is illustrated in Fig. 3. Below this line, the parabolas of every charge state of ion mass A are separated. An alternate way of viewing this is to note that such lines are constant velocity lines with velocity $v = \{\int Ed\ell / \int Bd\ell\}\{[4 + (k/A\delta)^2]^{1/2} - 2\}^{1/2}$. Any ions with velocity less than this value will be resolved. Thus, large values of k/δ will yield better charge resolution.

For mass resolution, let $dZ = 0$, $dA = 1$:

$$- \frac{Z}{A^2} = \frac{1}{k} \frac{2\theta_m}{\theta_e} \delta \left[1 + \left(\frac{\theta_m}{2\theta_e}\right)^2\right]^{1/2} \quad . \tag{13}$$

Using Eq. (4) to eliminate A, we obtain

$$\theta_m^6 - (Zk\delta\theta_m)^2 - 4(Zk\delta\theta_e)^2 = 0 \quad , \tag{14}$$

which can be solved numerically. An interesting analytical result can be derived when the charge state Z in Eq. (13) is eliminated in favor of mass number A. In this case, we find the line which connects the resolution points (points of separation) of parabolas with atomic numbers A and A + 1 with different charge states:

$$\theta_m = \frac{2A\delta\theta_e}{\left[\theta_e^2 - (A\delta)^2\right]^{1/2}} \quad . \tag{15}$$

This equation describes a hyperbola with asymptotes $\theta_e = A\delta$ and $\theta_m = 2A\delta$ above which isotopes are resolved as in Fig. 4. This can be generalized
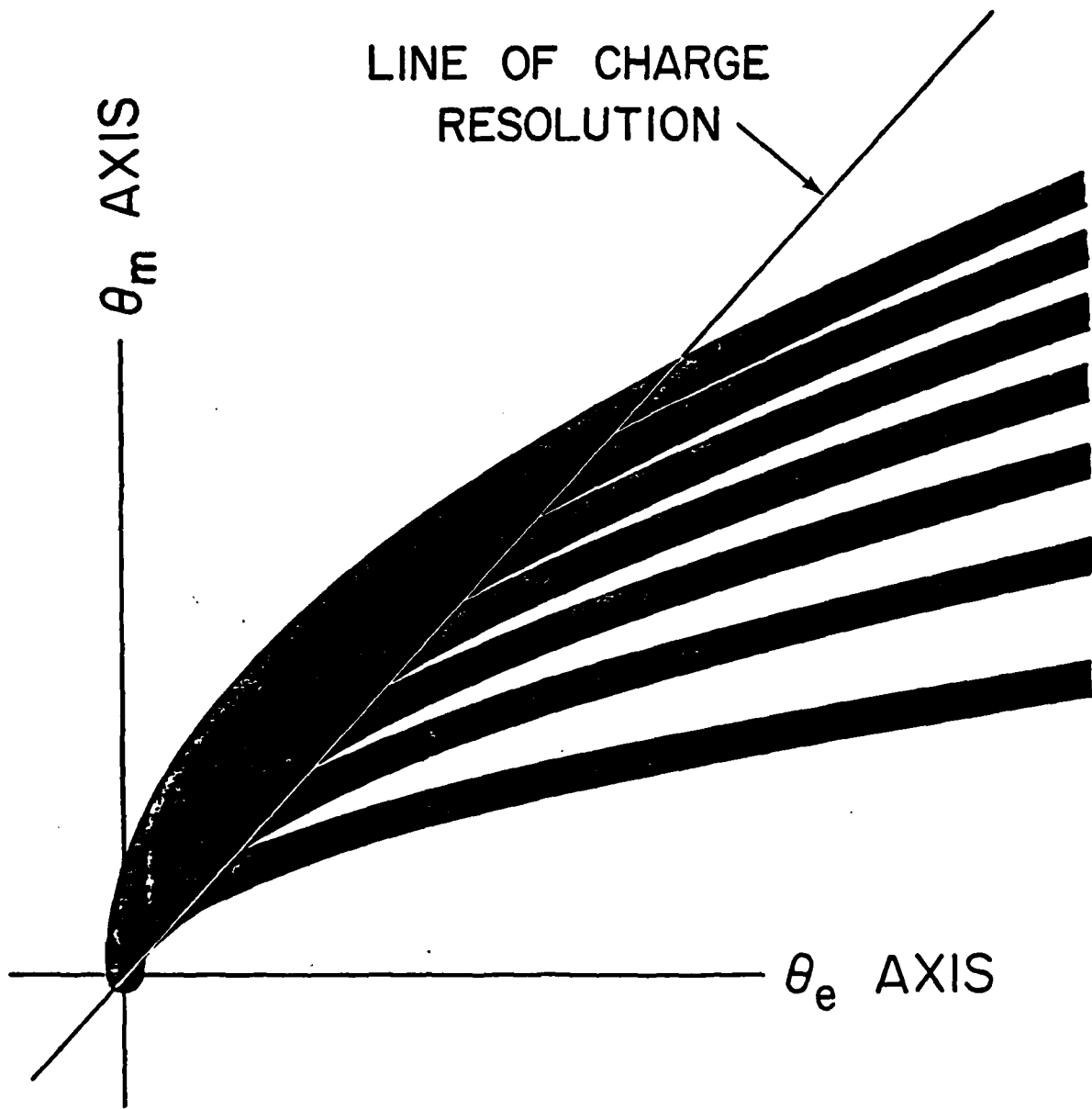
Fig. 3 Charge resolution geometry. Shown is a set of parabolas with

A = 35, k = 1.00 and δ = 11 mrad. The line of charge resolution
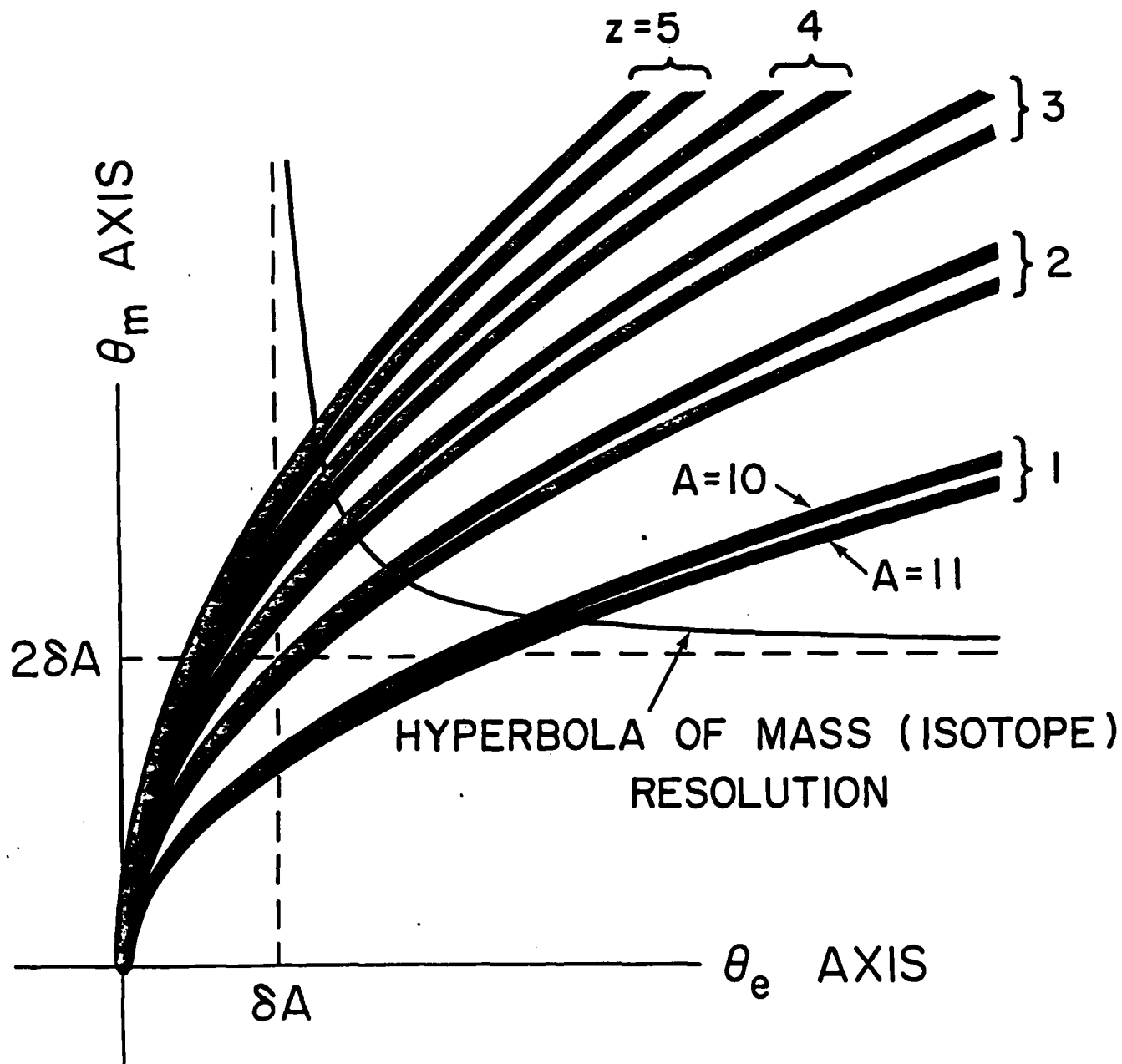
is calculated from Eq. (12).

Fig. 4 Mass (isotope) resolution geometry. Resolution curves that describe points of separation of parabolas corresponding to mass numbers A and A + 1 at different charge states are described by hyperbolas with asymptotes at $\theta_e = A\delta$ and $\theta_m = 2A\delta$. Shown is $\delta = 5.5$ mrad and $A = 10$.

to dA = n provided n/A << 1 in order to obtain a resolution curve for elements which differ in mass number by n. This leads to the simple modification in Eq. (15) that A must be replaced by A/n everywhere it appears.
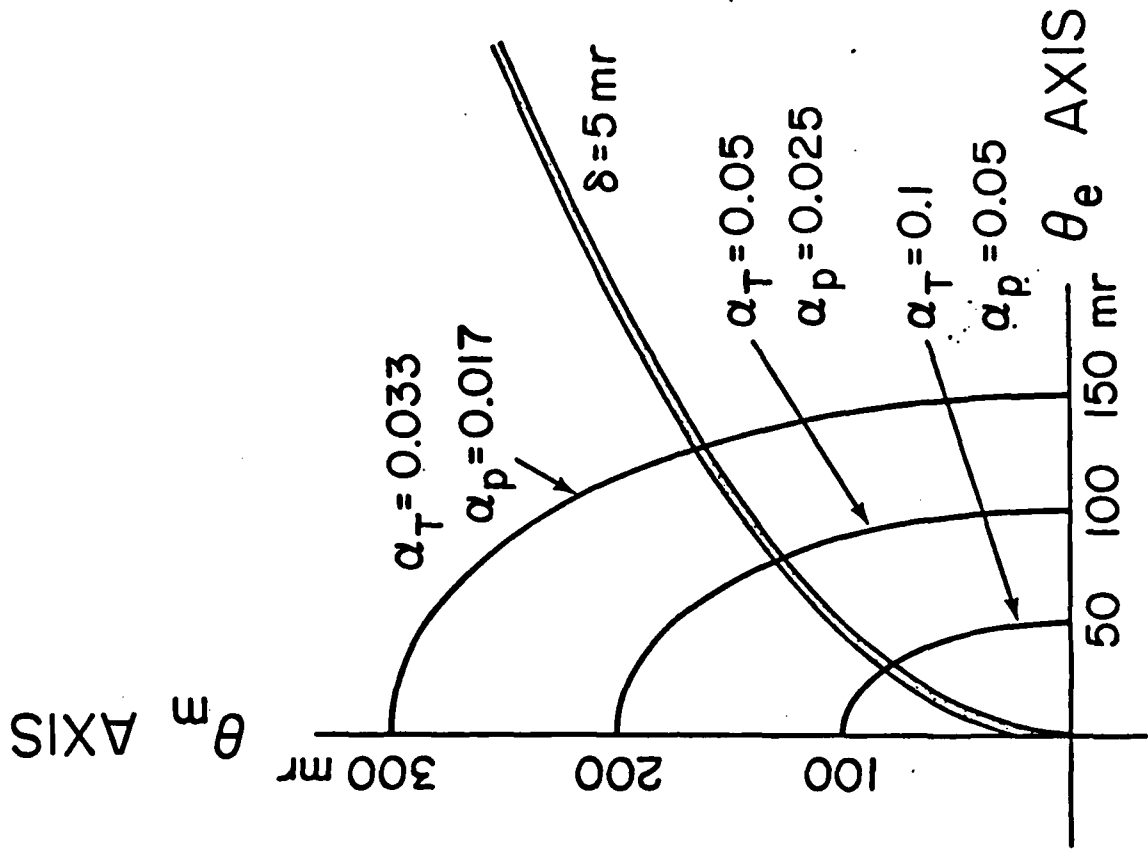
IV. Analysis of Energy and Momentum Resolution

Energy and momentum resolution is also limited by the subtended angle of the pinhole collimation spot, δ. The spectrogram can be thought of as a superposition of many of these spots infinitely close together along the parabola. Energy or momentum, which is found from either the electric or magnetic deflection angle is hence uncertain by an amount corresponding to the projection of the collimation spot length δ along the parabola onto the electric or magnetic axis of the spectrogram [see Fig. 5(a)]. Within our approximation, these quantities are related by the equation:
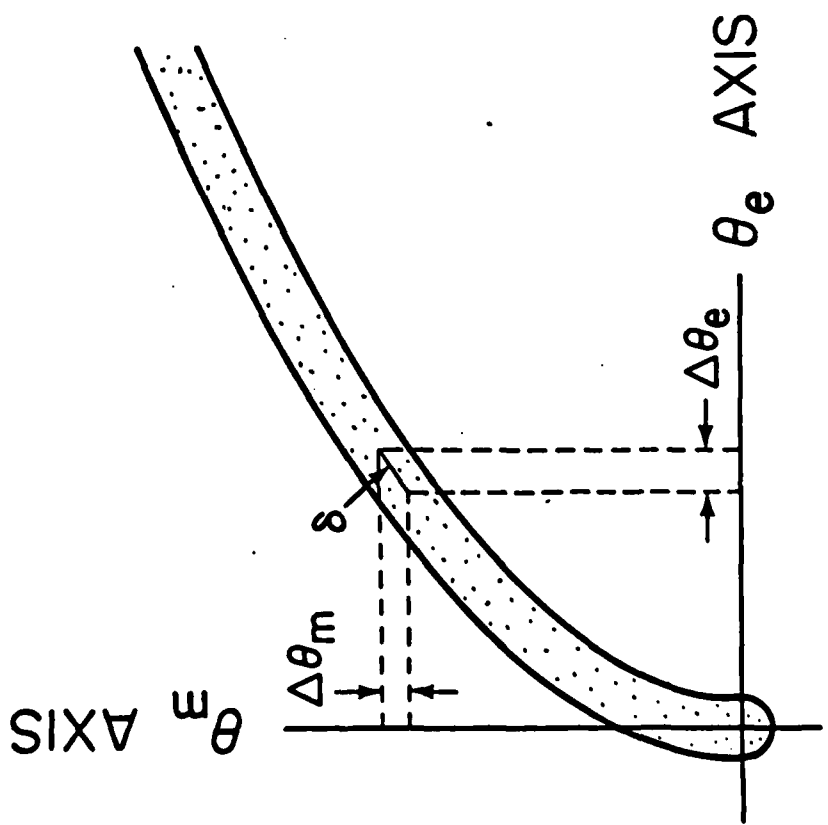
$$\delta^2 = \left[1 + \left(\frac{\theta_m}{2\theta_e}\right)^2\right](\Delta\theta_e)^2 \tag{16}$$

where we have used Eq. (8). Relative energy and momentum uncertainties $\Delta T/T$ and $\Delta p/p$ can be found from the deflection Eqs. (2) and (3) in terms of θ_e as;

$$\alpha_T = \frac{\Delta T}{T} = -\frac{\Delta\theta_e}{\theta_e} \quad ,$$

$$\alpha_p = \frac{\Delta p}{p} = -\frac{\Delta\theta_e}{2\theta_e} \quad . \tag{17}$$

Fig. 5

(a) Energy or momentum, which is derived from projection on the θ_e or θ_m axis, is uncertain due to the spot size δ as it is projected onto the axes.

(b) This uncertainty gives contours of constant relative energy or momentum uncertainty which are ellipses. Shown is a $\delta = 5$ mrad parabola with some associated contours.

A quantity Q_i, representing either T or p can then be expressed along with its uncertainty as $Q_i(1 \pm \alpha_i/2)$. It is of interest to find the curves of constant α_i which will give a contour map of relative uncertainty of energy or momentum. Substitution of Eq. (17) into Eq. (16) yields,

$$\frac{\theta_e^2}{(\frac{\delta}{\alpha_T})^2} + \frac{\theta_m^2}{(\frac{2\delta}{\alpha_T})^2} = 1$$

(18)

$$\frac{\theta_e^2}{(\frac{\delta}{2\alpha_p})^2} + \frac{\theta_m^2}{(\frac{\delta}{\alpha_p})^2} = 1$$

These describe upright ellipses about the origin which are contours of constant relative uncertainty as illustrated in Fig. 5(b). The relative energy or momentum resolution at a certain point on the parabola corresponds to the α_T or α_p value of the ellipse that intersects that point. In terms of spectrometer parameters, by combining Eqs. (2), (3), and (18) with the definition of k, we can find the energy uncertainty of a certain ion species as a function of its energy per charge as

$$\alpha_T = \frac{2(\frac{T}{Z})\delta}{e \int Ed\ell} \left[1 + (\frac{Z}{A}) \frac{(\frac{T}{Z})k}{2e \int Ed\ell}\right]^{-1/2}$$

(19)

or more simply, in terms of electric deflection angle θ_e,

$$\alpha_T = \frac{\delta}{\theta_e} \left[1 + \frac{Z}{A} (\frac{k}{4\theta_e})\right]^{-1/2} \quad .$$

(20)

V. Comparison of Spectrometers

The principles examined in the previous sections are applied to the design of a new compact Thomson spectrometer in order to improve resolution over previously reported spectrometers.[4,6,11,12] Resolution analysis shows us the importance of the parameters k and δ. The lower limit of δ is determined by the ion flux produced by the source for the spectrometer. If one tries to make δ too small, insufficient flux will reach the detector to make the parabolas distinguishable or to provide enough statistical information to produce useful energy spectra. For maximum flux to reach the detector, D_3' in Fig. 1 must be larger than zero (nonnegative). D_3' is given by the equation

$$D_3' = \frac{L_2}{L_1} (D_2 - D_1) + D_2 > 0 \quad . \tag{21}$$

In conjunction with this consideration, we wish to make δ as small as possible. It has been discussed in Ref. 12 that simultaneously satisfying both conditions is best accomplished by placing the second pinhole in the collimation system downstream of the field region. The spectrometer is shown in Fig. 6. A single pinhole (not shown in Fig. 6) is placed approximately 40 cm upstream of the spectrometer. When the beam reaches the spectrometer after passing through the first pinhole, it is relatively diffuse and usually covers the entire spectrometer entrance area. This condition depends upon the nature of the ion source as well as its distance from the first (upstream) pinhole. Usually all plasma type sources are of satisfactory nature. Upon entering the spectrometer, the ion trajectories are parallel to each other and

SOFT IRON
CASE

IONS

RARE
EARTH
COBALT
MAGNETS

S

N

CR-39

PINHOLE
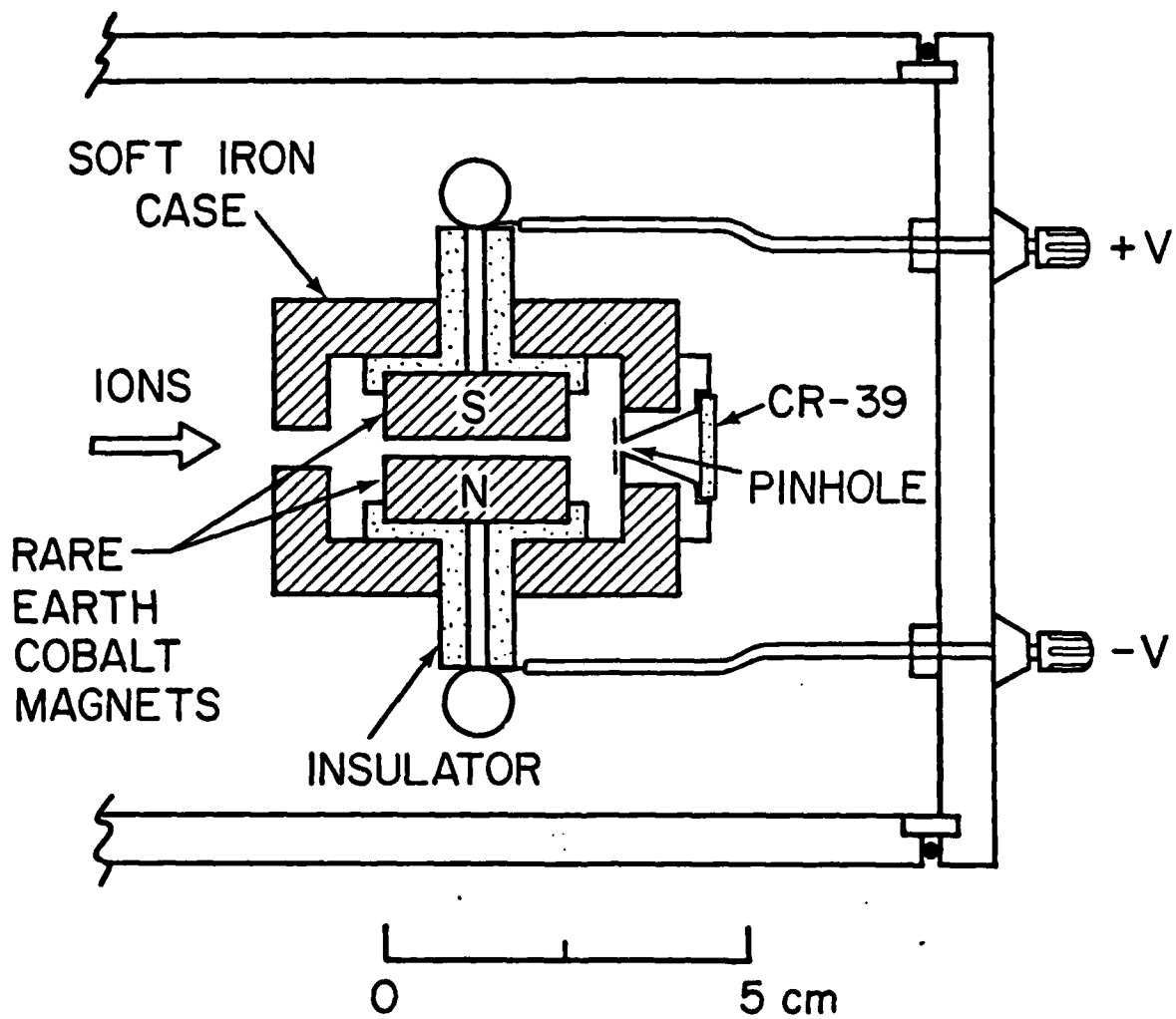
INSULATOR

+V

−V

0   5 cm

Fig. 6 Cross sectional view of a high resolving power compact Thomson
       spectrometer.

perpendicular to the fields. The ions passing through the field region are deflected and subsequently pass through the second (downstream) pinhole. The position they impact on the detector then depends only upon the velocity components they had upon leaving the pinhole. Experience shows that scattering from the pole pieces is not a problem.

The parameter k is proportional to the square of $\int Bd\ell$ and inversely proportional to $\int Ed\ell$. The minimum value of $\int Ed\ell$ is limited by the energy range of the ions to be analyzed as well as the acceptance angle of the magnetic pole gap. $\int Bd\ell$ is in general not limited in this manner and we are free to choose higher values of $\int Bd\ell$ in order to increase resolving power of the spectrometer. In order to obtain a large $\int Bd\ell$, the spectrometer is made from rare earth cobalt 2.54 cm diameter disc magnets which are placed within a soft iron case. The pole gap used is 2.54 mm. The soft iron case provides good containment of the fields. $\int Bd\ell$ is found by Am^{241} α-particle calibration[5,12] to have the value 1.66×10^{-2} T-m. The rare earth cobalt magnets, which are insulated from the case, can be biased to high voltage producing the necessary E parallel to B configuration. $\int Ed\ell$ is found experimentally to have the value $12.8 \times V$, where V is the voltage applied to the electrodes (magnets). Using typical values for this spectrometer, $\delta = 5.2$ mrad, k = 1.48, and $\int Ed\ell = 1.80 \times 10^4$ volts, from Eq. (19) we can obtain a plot of α_T, relative energy uncertainty, vs. T/Z, energy per charge, for various charge to mass ratios (see Fig. 7). As in all Thomson spectrometer systems, the acceptance angle of the pole gap, the ion charge, and the electric field path integral, $\int Ed\ell$, determine the minimum energy of the ions which may pass through the spectrometer
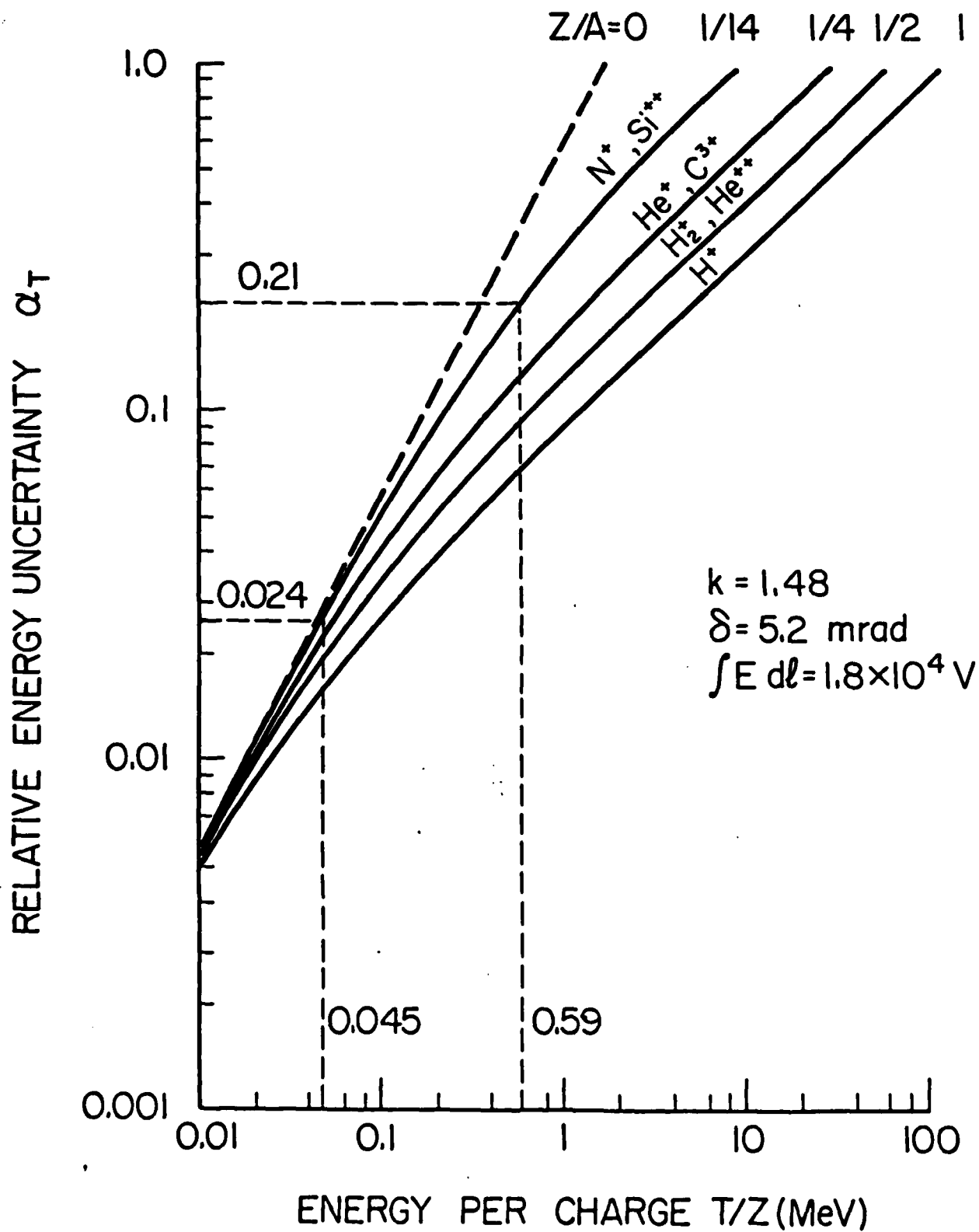
Fig. 7 Plot of relative energy uncertainty α_T vs. energy per charge T/Z
for several different charge to mass ratios and using the
spectrometer parameters discussed in the text.

unobstructed by the pole pieces. For $\int Ed\ell = 1.80 \times 10^4$ volts, the minimum energy per charge which can be measured is 45 keV. For example, if we wish to analyze a N^+ parabola we see in Fig. 7 that the minimum possible relative energy uncertainty is 0.024 ($\pm$ 1.2%) for this spectrometer. A parabola obtained from a plasma focus ion source is shown in Fig. 8(b). The peak N^+ energy in Fig. 8(b) is 0.59 MeV which has a relative energy uncertainty α_T of 0.21 ($\pm$ 10.5%).

Spectrograms from both old and new spectrometers are obtained with a plasma focus device.[11] They are displayed in Fig. 8. Figure 8(a) shows a Thomson spectrogram with the parameters $\delta = 6.0$ mrad and $k = 0.16$. The ions were identified as N^+, N^{2+}, and N^{3+}. From Eq. (12) we calculate the slope of charge resolution to be 0.87. This means that ions with velocity less than 3.2×10^6 m/s, or Nitrogen kinetic energy, T_N, less than 740 keV, will be separated in charge. The two asymptotes for the hyperbola of mass resolution of Carbon (A = 12) and Oxygen (A = 16) from Nitrogen (A = 14) are shown on the spectrogram indicating that the region containing the tracks is not within the mass resolution region. In Fig. 8(b), δ is 5.2 mrad and k is now 1.48. The increased magnetic field brought the tracks into the mass resolution region enabling the identification of C and O impurities. The charge resolution region now contains the major portion of the mass resolution region. The charge resolution slope, 4.3, corresponds to a velocity of 4.7×10^6 m/s or T_N of 1.57 MeV.

We compare this spectrometer to one used for a collective ion acceleration experiment.[4,6] In this conventional spectrometer, both collimating pinholes are located upstream of the fields and are
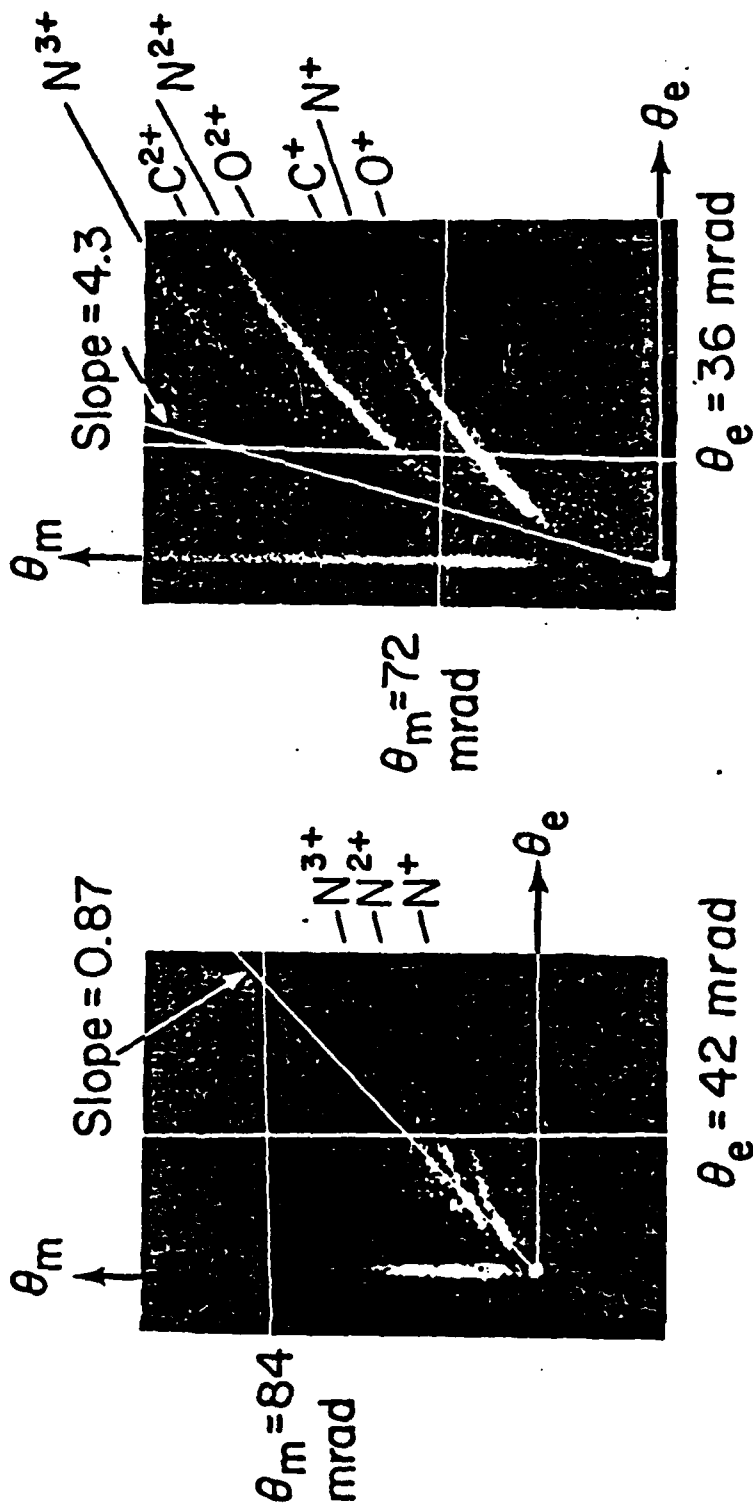
Fig. 8 Comparison of two spectrograms.

(a) A Thomson spectrogram with $\delta = 6.0$ mrad and $k = 0.16$. The three lower parabolas were identified as N^+, N^{++}, and N^{3+}. The slope of charge resolution from Eq. (12) is 0.87. The asymptotes for resolution of C and O from N are $\theta_e = 42$ mrad and $\theta_m = 73$ mrad.

(b) A spectrometer with higher resolving power separated the parabolas enabling the identification of carbon and oxygen impurities. For this spectrogram, $\delta = 5.2$ mrad and $k = 1.48$. The slope of charge resolution is 4.3. The asymptotes for resolution of C and O from N are $\theta_e = 36$ mrad and $\theta_m = 73$ mrad.

unobstructed by the pole pieces. For $\int Ed\ell = 1.80 \times 10^4$ volts, the minimum energy per charge which can be measured is 45 keV. For example, if we wish to analyze a N^+ parabola we see in Fig. 7 that the minimum possible relative energy uncertainty is 0.024 ($\pm$ 1.2%) for this spectrometer. A parabola obtained from a plasma focus ion source is shown in Fig. 8(b). The peak N^+ energy in Fig. 8(b) is 0.59 MeV which has a relative energy uncertainty α_T of 0.21 ($\pm$ 10.5%).

Spectrograms from both old and new spectrometers are obtained with a plasma focus device.[11] They are displayed in Fig. 8. Figure 8(a) shows a Thomson spectrogram with the parameters δ = 6.0 mrad and k = 0.16. The ions were identified as N^+, N^{2+}, and N^{3+}. From Eq. (12) we calculate the slope of charge resolution to be 0.87. This means that ions with velocity less than 3.2×10^6 m/s, or Nitrogen kinetic energy, T_N, less than 740 keV, will be separated in charge. The two asymptotes for the hyperbola of mass resolution of Carbon (A = 12) and Oxygen (A = 16) from Nitrogen (A = 14) are shown on the spectrogram indicating that the region containing the tracks is not within the mass resolution region. In Fig. 8(b), δ is 5.2 mrad and k is now 1.48. The increased magnetic field brought the tracks into the mass resolution region enabling the identification of C and O impurities. The charge resolution region now contains the major portion of the mass resolution region. The charge resolution slope, 4.3, corresponds to a velocity of 4.7×10^6 m/s or T_N of 1.57 MeV.

We compare this spectrometer to one used for a collective ion acceleration experiment.[4,6] In this conventional spectrometer, both collimating pinholes are located upstream of the fields and are

separated by 23 cm (L_1). The distance from the second (downstream)
pinhole to the detector is 18.7 cm (L_2), and each pinhole is 0.2 mm in
diameter. This yields a D_3 of 0.53 mm by Eq. (5). The distance from
the center of the field region to the detector is 8.7 cm (L), hence by
Eq. (6), δ = 6.0 mrad. From the magnetic and electric field integrals
of 9.48×10^{-3} T-m and 3.42×10^4 volts respectively, we find k =
0.25. The slope of charge resolution for N is found from Eq. (12) to be
1.26, corresponding to a velocity of 4.55×10^6 m/s or T_N = 1.50 MeV.
The asymptotes for mass resolution of C and O from N are θ_e = 42 mrad
and θ_m = 84 mrad. This spectrometer has similar resolution to the one
reported in this paper; however, its field region is an order of
magnitude larger. This leads to larger spectrograms which are much more
difficult to analyze quantitatively than small plates which can be
viewed under a microscope.[12]

VI. Conclusions

The resolution of the Thomson spectrometer was examined, and simple
analytic expressions for resolution curves were obtained. The
importance of two parameters in particular was displayed, k and δ. In
general, the ratio k/δ should be made as large as possible consistently
with the ion energy range and the ion flux reaching the spectrometer.
The analysis shows the advantages of the compact spectrometer design
proposed by Rhee which places the second pinhole downstream of the field
region. This design allows the reduction of δ without the associated
sacrifice of ion track density on the detector. The energy range and
acceptance angle of the pole gaps determines the optimum $\int Ed\ell$. The new

high resolving power Thomson spectrometer utilizes a permanent magnet with a much larger magnetic field increasing $\int Bd\ell$ and hence k. The resulting spectrometer has applications in many fields of research.

Acknowledgements

References

1. G. W. Kuswa, L. P. Bradley, and G. Yonas, IEEE Trans. Nucl. Sci. NS-20, 305 (1973).

2. R. F. Hoeberling, R. B. Miller, D. C. Straw, and D. N. Payton III, IEEE Trans. Nucl. Sci. NS-24 (3), 1662 (1977).

3. S. Takeda, M. Tamura, T. Yamamoto, and M. Kowanishi, Jpn. J. Appl. Phys. 18 (3), 641 (1979).

4. W. W. Destler and J. T. Cremer, J. Appl. Phys. 54 (2), 636 (1983).

5. J. R. Smith, Ph.D. Thesis, North Carolina State Univesity (1983).

6. J. T. Cremer, Ph.D. Thesis, University of Maryland (1984).

7. M. J. Rhee, Bull. Am. Phys. Soc. 25 (8) 958 (1980).

8. H. Herold, A. Mozer, M. Sadowski, and H. Schmidt, Rev. Sci. Instrum. 52 (1), 24 (1981).

9. M. J. Rhee, IEEE Trans. Nucl. Sci. NS-28, 2663 (1981).

10. A. Mozer, M. Sadowski, H. Herold, and H. Schmidt, J. Appl. Phys. 53 (4), 2959 (1982).

11. M. J. Rhee and R. F. Schneider, IEEE Trans. Nucl. Sci. NS-30, 3192 (1983).

12. M. J. Rhee, Rev. Sci. Instrum. 55, (page) (1984).

END

FILMED

11-85

DTIC